Organic crystals and improved electrolyte for aqueous sodium-ion batteries

Fundamental insights in new organic anode materials for aqueous sodium-ion batteries using DFT calculations and experimental insights in increased electrolyte stability

Kajan Nando Kort

Technische Universiteit Delft

TU Delft

Organic crystals and improved electrolyte for aqueous sodium-ion batteries

Fundamental insights in new organic anode materials for aqueous sodium-ion batteries using DFT calculations and experimental insights in increased electrolyte stability

by

Kajan Nando Kort

in partial fulfillment of the requirements for the degree of

Master of Science
in Sustainable Energy Technology

at the Delft University of Technology,
to be defended publicly on Thursday 21 December, 2017 at 10:00 AM.

Student number:	4291697	
Project duration:	March 29, 2017 – December 21, 2017	
Thesis committee:	Prof. dr. ir. F. M. Mulder,	TU Delft, external assessor
	Dr. E.M. Kelder,	TU Delft, assessor
	Dr. ir. M. Wagemaker,	TU Delft, supervisor
	Ir. A. Vasileiadis,	TU Delft, daily supervisor

An electronic version of this thesis is available at `http://repository.tudelft.nl/`.

TU Delft

Abstract

Density Functional Theory (DFT) calculations were performed to explore the electrochemical properties of two organic molecules that show promise to serve as affordable and safe anode materials in aqueous sodium-ion batteries. Upon sodium insertion, N,N' –bis(methyl)- 1,4,5,8-naphthalene diimide (NDMe) appears to share sodium atoms with three surrounding molecules in the crystal lattice in so called Triple Binding Spots (TBS). Until a sodiation fraction of 0.5, it shows a voltage plateau at 1.78 V versus Na/Na^+. For increasing sodiation fractions a voltage plateau of roughly 0.4 V versus Na/Na^+ is predicted. The second organic molecule N,N' –bis(p-tolyl)- 1,4,5,8-naphthalene diimide (NDTo) appears to share sodium atoms between in two or four molecules, forming Dual Binding Spots (DBS) or Quartet Binding Spots (QBS). After Van der Waals corrections, the voltage profile of NDTo shows a sloping voltage between 2.05 V and 1.2 V till a sodiation fraction of 0.5, followed by a rather low voltage plateau at 0.24V versus Na/Na^+ until full sodiation.

It is found to be of crucial importance to include a Van der Waals correction in the DFT calculations for NDMe and NDTo. Without Van der Waals corrections, the outcomes of the DFT calculations without exceptions show large deviations from experimental data in all cell parameters. For NDTo, the Van der Waals corrections show more significance for an increasing fraction of sodiation.

Both organic crystals show extreme lattice distortions upon sodiation. NDMe shows a volumetric change of 14,73% upon full sodiation with changes in vector lengths up to 50,13%. NDTo shows a volumetric change of 8,24% upon full sodiation with changes in vector lengths up to 10,41%. These large lattice distortions demand for the crystal structure to have an exceptionally high flexibility in order to prevent material degradation when applied as anode material in a sodium-ion battery. For this reason a revaluation of NDMe and NDTo as robust anode materials is suggested, based on computational findings as presented here.

Solutions with different concentrations of sodium perchlorate ($NaClO_4$) have been tested in a three-electrode open test-cell to find evidence for an enlarged electrochemical stability window compared to that of distilled water. At a concentration of 10M, close to the saturation limit, the solution shows a stability window between -1.29 V and 1,762 V versus Ag/AgCl, effectively offering a stability window of 3.05 V. In order to test its applicability with an organic anode material, NDMe has been obtained and tested in 10M $NaClO_4$ versus a titanium counter electrode. To proof the open test-cell design to be suitable for yielding reliable results, two easy to synthesize inorganic electrodes that are elaborately described in previous studies have been selected and tested as reference electrode materials.

NDMe shows redox potentials that are well within the improved stability window, suggesting safe use as anode material in aqueous batteries. However, capacity fading was observed upon the first cycles, which could not be quantified. Due to the open test-cell, dissolved oxygen can easily react, and is replenished by atmospheric oxygen. A new type of test-cell that is air tight is strongly recommended. Future research may now look beyond the limitations of the traditional narrow aqueous stability window, by identifying and testing aqueous battery chemistries that approach 3.0 V full cell potentials.

Contents

Nomenclature

The next list describes several abbreviations and symbols that will be later used within the body of the thesis. A more elaborate explanation of the listed nomenclature is provided at first use in the thesis.

$NDMe$	N,N' –bis(methyl)- 1,4,5,8-naphthalene diimide
$NDTo$	N,N' –bis(p-tolyl)- 1,4,5,8-naphthalene diimide
ALB spots	Assumed Logical Binding spots
DBS	Dual Binding Spots
DFT	Density Functional Theory
$Na_{0.44}MnO_2$	Sodium Manganese Oxide
$NaClO_4$	Sodium Perchlorate
$NaTi_2(PO_4)_3$	Sodium Titanium Phosphate (NTP)
O1-O4	Oxygen atom 1-4
QBS	Quartet Binding Spots
TBS	Triple Binding Spots
True host	The oxygen atom which is nearest to the sodium atom
VASP	Vienna Ab-initio Simulation Package
Å	Ångstrom=10^{-10} meter

1 Introduction

1.1. The need for energy storage

Energy transition

The global energy mix consists out of primary energy sources which are currently predominantly fossil fuels. Global human population is expected to increase, which is paralleled by the expected increase in energy demand per person. Concerns about climate change caused by anthropogenic greenhouse gas emissions make fossil fuels a dangerous and unethical source of energy. There are different greenhouse gasses of which carbon-dioxide is most often addressed in the world's political and scientific debates. Carbon-free energy sources are needed thus supply the world population of clean and sustainable energy. The transition from a fossil-fuel based energy system to a renewable energy based system is called the energy transition, and is believed to be one of the most urgent worldwide challenges.

Electricity can be made using sustainable energy sources. Most processes that currently use fossil fuels can be electrified and can thus become independent of fossil fuels. There are several sustainable carbon-free energy sources such as solar, wind, geothermal, hydro and tidal energy. In figure 1.1 the total estimate potential of all renewable energy sources are given in Terra Watt (TW) and the potential of finite sources in TW-years.[41] It is obvious that solar energy is by far the biggest renewable energy source, followed by wind, hydro and geothermal energy. Also, the enormous potential of renewable energy sources versus finite sources provides sufficient evidence to belief the energy transition is far from unrealistic.

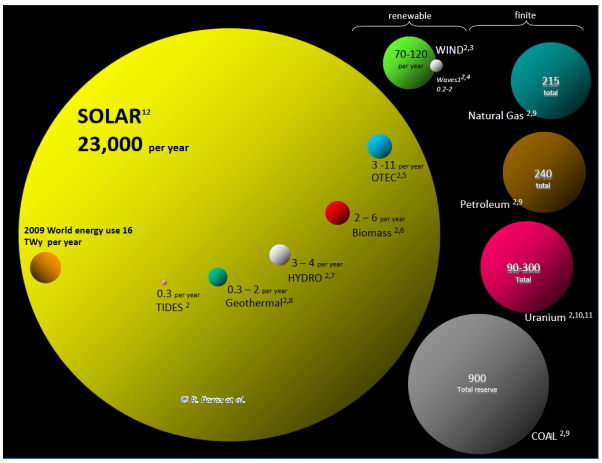

Figure 1.1: Estimate of planetary energy reserves. Renewable energy sources in [TW] and finite sources in [TW-yr].[41]

Energy storage solutions

Most renewable energy sources have an intermittent character. Both daily and seasonal fluctuations lead to a mismatch with the energy demand, which also fluctuates but in a different rhythm. To counteract this mismatch between energy supply and demand, large scale energy storage solutions are required. Among them are pumped-hydro, compressed air, chemical and electrochemical energy storage. The feasibility and application of the energy storage types are size-dependent, can be place-dependent and are always price-dependent. Also, other characteristics such as safety, toxicity, energy density, specific energy and scarcity of

materials are important parameters to take into account when evaluating different energy storage options. Different applications call for different trade-offs between the energy storage characteristics. For example, for mobile applications such as electrical cars, mobile phones and laptops, the energy density, specific energy and battery lifetime are of vital importance. In contrast, for large-scale and stationary application such as the stabilization of a national electricity grid, power density, total capacity size and price per kilowatt-hour are more decisive.

The advancement of the energy transition is dependent on the availability and affordability of large-scale stationary energy storage solutions. Affordable energy storage will accelerate the uptake and implementation of renewable energy sources. Therefore, it is of great relevance to explore new possibilities for large-scale and affordable energy storage. Electrochemical energy storage is assumed to be one of the most viable options for both small scale and large scale short-term energy storage in a wide range of applications.

1.2. Battery storage

Different chemistries

There are numerous different battery technologies offering energy storage for a wide range of applications. The size range for batteries is extremely large, from micro-scale batteries used in medical applications such as pacemakers to Giga-scale battery systems used for stabilization of the electricity grid. The lithium-ion battery is now one of the most popular battery chemistries because of the high energy density, high cell voltage and considerable long life-time.[19] This makes the lithium-ion battery extremely suitable for mobile applications where energy density is one of the most important parameters. The energy density of lithium-ion batteries has since its commercialization structurally increased by about 8 Wh/kg, currently reaching about 250 Wh/kg. The costs have come down from 1000 €/kWh in the mid 1990s to below 200 €/kWh today. As further cost reduction is expected in the nearby future and electric vehicles are about to be mass produced, this could offset a sharply increase in demand. [37]

There are a number of drawbacks in the use of lithium in batteries. Firstly, lithium is not abundantly available and not evenly distributed over the earth's crust. When lithium demands increase, this could lead to scarcity driven price rise and political tensions in the lithium rich regions. As of today, three out of the four main lithium rich regions in the world are classified as political unstable regions, posing a serious risk to an undisturbed lithium production for world-wide large-scale energy storage. Secondly, the dominant lithium-ion battery chemistry consists out of toxic, flammable and expensive materials. It is understandable that these parameters are possibly less important than the energy density and specific energy in mobile applications that require small and light energy dense batteries. But for stationary applications, safety and environmental impact become important. Thirdly and possibly most important, the price of most lithium-ion batteries are considerably high, caused by the expensive production process that often requires oxygen and water free environment and high material purity.

These reasons justify the belief that other battery chemistries could be a better candidates for large-scale stationary energy storage. These alternatives should offer more prospect on the material availability, safety, toxicity and affordability in order to make the trade off with a lower energy density and specific energy feasible. Following this line of thought, the aqueous sodium-ion battery chemistry is one of the most promising candidates for large-scale stationary energy storage.

Aqueous sodium-ion battery

Like in many academic disciplines, battery research has been directed into commercially viable directions. For decades, more research has been done in the lithium-ion battery chemistry than any other battery chemistry. More recently, sodium-ion battery with organic electrolytes were researched and yielded commercially viable results. However, new insights and concerns regarding the toxicity, safety, material scarcity and affordability now seem to redirect the battery research to other areas, among them aqueous sodium-ion batteries.

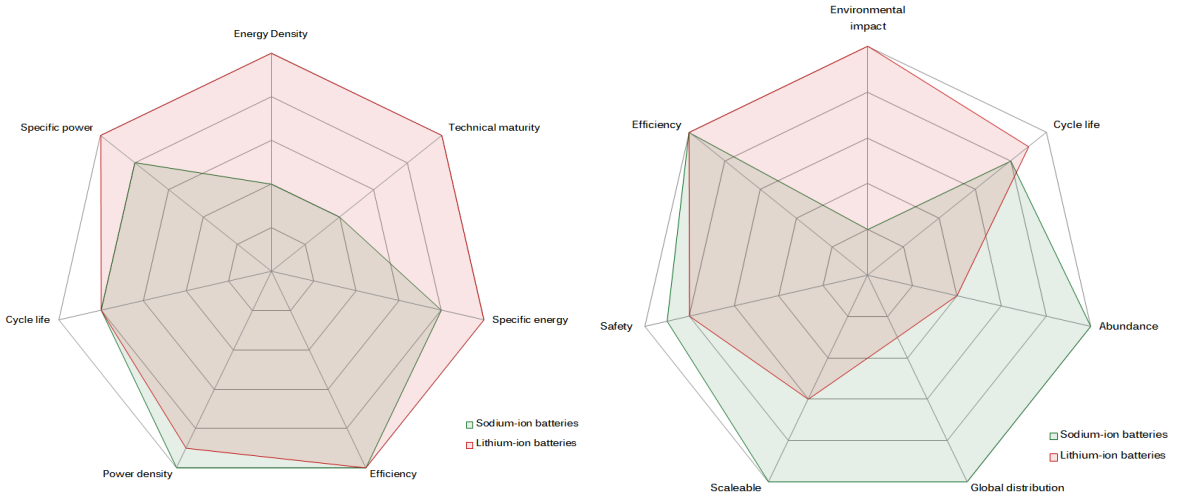

(a) for mobile applications

(b) for stationary applications

Figure 1.2: Comparison between Lithium-ion and Sodium-ion batteries based on important battery parameters for different applications.[59]

Similar to lithium, sodium is also an alkali metal and has similar properties. Alkali metals have a tendency to donate an electron spontaneously, which means that the reducing potentials of alkali metals are very low. This makes alkali metal ions interesting charge carriers in high potential batteries. The atomic radius of an sodium atom is approximately 25% larger than the atomic radius of a lithium atom, namely 102 nm instead of 0.076 nm. Sodium is one of the most abundant elements on earth, and unlike lithium, the occurrence of sodium is distributed evenly inside the earth's crust. Besides that, sodium containing compounds like sodium-chloride, commonly known as table salt, is dissolved in the oceans covering two third of the planet's surface.

In order to provide insight in the comparison between sodium-ion and lithium-ion batteries, a number of important battery parameters are combined in the radar charts in figure 1.2. Figure 1.2a shows the important battery factors for mobile applications such as electric vehicles, while figure 1.2b shows the important factors for stationary, large scale and affordable energy storage. From this comparison it is clear that sodium-ion batteries are significantly more promising for affordable large scale stationary energy storage than lithium-ion batteries.

Water has been used as electrolyte in battery chemistries for over a century, since Thomas Edison developed the renowned Nickel-Iron battery in 1901 using water as electrolyte. Even today aqueous electrolytes are used on a large scale, the well known lead-acid battery used in most internal combustion engine (ICE) cars also has an aqueous electrolyte. However, due to the rather low electrochemical stability window of water, it does not allow to be used in high potential battery. At cell potentials higher than 1.229V, it becomes thermodynamically possible for water to split into oxygen and hydrogen gas. The splitting of water in an active battery results in explosion risks and accelerated degradation of the battery components, resulting in a poor lifetime.

The electrochemical stability window of water has another implication. Besides the width of the window between the hydrogen and oxygen evolution lines, the distance of the window versus standard hydrogen (SHE) potential is of essential importance. Understandably, the pH value of the water influences the ease of forming hydrogen gas, thus the distance to the SHE potential. This correlation is showed in the Pourbaix diagram, which will be discussed in more detail in chapter 6 in section 6.1. By considering a range of applicable pH values, a range of anode and cathode materials can selected based on their redox potential. The main requirement is that the redox potential must not be significantly outside of the electrochemical stability window of water.

1.3. Promising research directions

Organic anodes

A promising research direction is to find new anode material that match with the stability window of (normal) water. As the search for suitable cathode materials has yielded satisfying candidates, the search for suitable anode materials seems to fall behind.[32, 35, 43, 66] Exploring new anode materials that satisfy the requirements for large-scale affordable aqueous sodium-ion batteries is thus a relevant effort. Previously examined suitable anode materials for aqueous sodium-ion batteries are transition-metal oxides, poyl-anionic compounds, metal ferricyanides and organic compounds.[30] Considering the relatively high prices and purity demands for materials consisting out of scarce metals, research focus has been directed toward identifying affordable organic crystals or polymers. [24, 39, 62, 70]

Organic molecules are composed of elements that naturally occur in organisms, like carbon, oxygen, nitrogen and hydrogen. These elements are among the most abundant on earth. The most well known carbon-based electrode material is graphite, which consists out of many 2 dimensional layers of hexagonal connected carbon atoms. Other than in lithium-ion batteries, graphite does not intercalate sodium atoms reversibly. Other carbonaceous materials such as petroleum cokes, carbon black, pitch-based carbon-fibers, polymers and hard-carbons have been demonstrated to insert sodium. The small particle size, low surface area/volume ratio and morphology that minimizes side-reactions at low voltages are properties of some carbon structures that make them favorable as electrode materials.[50] Unfortunately, most carbon-based anode materials show a sodiation voltage far outside of the stability window of water. However, a number of organic molecules are reported to be compatible for aqueous batteries.

Several studies have researched organic molecular structures with the ability to bind and release sodium atoms reversibly at potentials suitable for aqueous electrolytes. Among these organic structures are crystals and polyimides from pyrolenes, napthalenes and quinones. Most of these compounds are currently produced in bulk by the chemical industry with low costs a high efficiency. One study focused on the effect of different variations of naphthalene diimides (NDs) crystals on the redox potentials, by substitution of a number of chemical side groups to the backbone molecule. Changes in the electronic characteristics resulted in discharge potentials in the range of 2.3-2.9 V vs Li/Li+.[47] Two of the variants of NDs are considered to be of great interest for further research in aqueous sodium-ion batteries.

Promising Naphtalene Diimides

The attention of our research group has been directed towards variations of the naphthalene diimides, as suggested by Krishna et al.[26] The sodiation process of N,N' –bis(methyl)- 1,4,5,8-naphthalene diimide (NDMe) and N,N' –bis(p-tolyl)- 1,4,5,8-naphthalene diimide (NDTo) is currently not known, but many have suggested a two step enolisation mechanism involving two sodium atoms per step.

Previous results of experimental research performed by Buise (2017) give insight in the practical results of the sodiation and desodiation of NDMe. As his research includes recommendations to gain more insight in the fundamental enolisation mechanism for Naphthalene Diimides (NDs), it is interesting and useful to compare the computational results from our research with the experimental outcomes of the NDMe variant as reported by Buise.

As computational calculations for large organic molecules are not common, it is important to inform about possible adjustments in the computational methods used generally for metal oxides or other crystalline ceramics that typically have small unit cells. Insights from organic chemistry predict the Van der Waals force to be more significant in larger molecules. It is thus important to evaluate the impact of Van der Waals forces on the computational outcomes for the organic molecules.

Widening the stability window

Another promising research directions is to look for ways to increase the stability window of the aqueous electrolyte. If the potentials at which water decomposes could be widened, more different electrode materials will become applicable. Besides that, the working potentials of the battery will be increased, leading to battery battery performance.

The electrolyte salt concentration influences the electrochemical properties of electrode materials. [13, 30, 36, 53, 71] High concentrations can improve the Coulombic efficiency, cycling stability and bring down the activity of electrolyte solvents.Very recent reports on high concentrations of sodium salts in aqueous electrolytes show similar feasibility to lithium salts. For example, Kühnel et al tested ultrahigh concentrations (up to 37m) of Sodium bis(fluorosulfonyl)imide (NaFSI), reporting a stability window of 2.6 V.[27] Suo et al tested 9.26m sodium trifluoromethane sulfonate (NaOTF) showing an overall electrochemcial stability window of 2.5 V.[55] At these concentrations, the water molecules are outnumbered against the salt molecules, leading to the term 'water-in-salt (WIS)' instead of 'salt-in-water' electrolytes. However, fluoride and sulfur containing salts impose high costs and safety concerns, making them unsuitable for low cost and safe batteries.

Fluoride free sodium salts have also been reported for the application in electrolyte, amongst them Na_2SO_4, $NaNO_3$ and $NaClO_4$.[30, 35, 36, 40, 43, 45] Because Na_2SO_4 has a saturation concentration of roughly 2M and $NaNO_3$ is known to have significant corrosive side reactions[35], the choice to experiment with $NaClO_4$ can be justified.

Li et al [30] point out that high concentration $NaClO_4$ electrolytes is an effective strategy to improve electrochemical performance of ferricyanide cathode for aqueous sodium-ion batteries. High concentrations of $NaClO_4$ are proven to raise the working potential and improve the Coulombic efficiency. Having tested a range of concentrations between 1M and 9M, the 6M $NaClO_4$ aqueous electrolyte was considered to be optimal, as the Coulombic efficiency almost keeps invariable with further increase of concentration. [30]. Another study experimented up to 4 M $NaClO_4$ and found the highest concentration to be feasible. [35]

1.4. Research aim and objectives

The aim of this research is to gain fundamental insights in promising organic anode materials for aqueous sodium-ion batteries. Within this aim, it is of vital importance to assess the significance of the Van der Waals corrections. Besides the exploration of new anode materials, this research also aims to find evidence for the possibility and the feasibility of extending the electrochemical stability window of an aqueous electrolyte in sodium-ion batteries using organic anodes. These aims are in line with the ongoing research in critically assessing proper chemistries for aqueous sodium-ion batteries in order to establish robust, affordable and safe large-scale energy storage. These aims can be translate in a number of research objectives.

Part I: Computational work

1. Gain fundamental understanding in the electrochemical behavior of the organic crystals of NDMe and NDTo upon sodium insertion.
   (a) Observe the thermodynamic most stable binding spots for sodium to unravel the sodiation pathways.
   (b) Research the voltage profiles upon sodium insertion.
   (c) Gain insight in the crystalline lattice distortion upon sodium insertion.
2. Assess the significance of the Van der Waals corrections for the computational calculations of NDMe and NDTo upon sodium insertion.
   (a) Find an appropriate correction model based on the comparison with experimental data.
   (b) Compare the uncorrected computational outcomes with the corrected outcomes and search for evident trends.

Part II: Experimental work

1. Assess the feasibility of $NaClO_4$ to be used in improving the aqueous electrolyte for affordable aqueous sodium-ion.
   (a) Research the effect of increasing molarity of $NaClO_4$ on the electrochemical stability window of water.
   (b) Research the applicability of concentrated solutions of $NaClO_4$ with the NDMe anode material.
   (c) Determine the impact of highly concentrated $NaClO_4$ solutions on the safety, environmental and cost of an aqueous sodium-ion battery.

1.5. Document Structure

This thesis is structured in a way to provide most structure for the reader. As the research objectives can be roughly divided into a computational part and an experimental part, the thesis is structured by assigning parts. In the first part, the background theory for computational research methods provided in chapter 2. This is logically followed by the used research methods and settings as described in chapter 3. The computational results are presented in chapter 4, followed by the discussion and interpretation of the results in chapter 5. Additional results and illustrative references are presented in the appendices at the end of the thesis.

The second part knows a similar structure, but for the experimental part of the research. Background theory is provided in chapter 6, followed by a description of the research methods and measurements in chapter 7. Experimental results are presented in chapter 8. The findings are critically discussed and put in a wider scientific context in chapter 9.

Finally, the computational and experimental research parts come together in the last chapter and the thesis is finished by the research conclusions and recommendations.

I

First Part: Computational work

2

Background theory on electrochemistry and computational analysis

2.1. Electrochemical energy storage

Electrochemistry is the study of the relationships between electricity and chemical reactions, which includes both spontaneous and non-spontaneous reactions. A battery is a device that can store chemical energy that can be converted into electrical energy by means of a redox reaction. Thus, theory from electrochemistry is needed to explain the working principle of a battery. This section is written using insights from both the academic chemical reference book written by Brown and others [3] and insights from the book on advanced batteries by R.A. Huggins. [18]

2.1.1. Battery chemistry

A battery is an electrochemical power source that consists of one or more voltaic cells. A battery consists of three main components: the anode, the cathode and the electrolyte. The anode and the cathode are separated by the electrolyte, which does not conduct electrons but is permeable to ions. The electrons are transported through an external circuit. Other important components of the battery are the separator, which prevents the electrodes from short-circuiting and the current collectors which are placed behind the electrode material to enhance the electronic conductivity. There are two types of batteries; primary cells are not rechargeable and are often used for small electronic devices. Secondary cells can be recharged and are used for a wide range of application. Stationary large-scale energy storage requires secondary batteries with a high lifetime and efficiency, therefore only secondary cells are of interest here.

An ideal electrode materials is able to store and release energy without capacity losses. There are generally three ways for the electrode materials to store energy. The first two are reconstitution and decomposition involve alloying of the charge carriers with the active electrode material upon release or uptake. This often causes unavoidable swelling and shrinking, as the ratio of ion exchange and the active material is generally high. When the volume change becomes too large, material failures such as cracking, splitting or deformations can occur. The third ion-exchange reaction is called intercalation, which translates to the storage of ions in available 'parking spots'. Although volume changes and deformations are possible in intercalation reactions, it is generally insignificant compared to the reconstitution and decomposition reactions. A great advantage of the intercalation mechanism is that materials can be used that do not consist out of dangerously reactive sodium metal.

2.1.2. Red-ox reaction and cell potential

The key working principle of a battery is the reduction-oxidation (red-ox) reaction. A chemical reaction is called a redox reaction when the oxidation numbers of the elements involved in the reaction change during the reaction. The oxidation number represents the charge for mono-atomic atoms, and for neutral molecules and poly-atomic ions it represents the hypothetical charge. The hypothetical charge is assigned by artificially dividing up the available electrons among the atoms in the molecule or ion.

A complete redox reaction is built up from two half-reactions, that each describe only the oxidation or the reduction reaction. The complete redox reaction can only occur when both half-reactions take place simultaneously. It is very useful to work with half-reactions in order to predict the electrochemical favorability of a reaction. The half-cell reaction of a substance takes place at a certain voltage. As the half-cell reactions are reversible, the potential for the reversed half-reaction changes sign (+ becomes - and vice verse).

If an elements is reduced it gains an electron, and if it is oxidized it loses an electron. Every elements, substance or chemical has a certain 'tendency' to retain electrons. If two compounds with a different tendency for electrons come in contact, they will strive towards an equilibrium. The resulting redox reaction will only stop when this equilibrium has been reached. In a battery this equilibrium is the moment people consider a battery 'empty'. The 'tendency' to retain electrons is a physical property and can be translated into 'reduction potential'. The reduction potential is generally expressed relatively versus the Standard Hydrogen Electrode (SHE) reduction potential.

The voltaic cell consists out of at least two different substances with different reduction potentials. A redox reaction can spontaneously occur when the potential of the reduction half-reaction is higher than the oxidation half-reaction. The battery needs to be charged in order to reverse the process until all electron donating atoms are filled with electrons and electron withdrawing electrons are deprived of electrons. In a voltaic cell, the transfer of electrons takes place through an external pathway rather than directly between the substances. In this way, the redox reaction only occurs when energy is added to or subtracted from the battery. The cell potential of a battery is the absolute difference in half-cell potentials. As different battery chemistries contain different substances, the half-cell reactions dictate the cell potential of a battery.

The working principle of the battery can also be described mathematically, to easily predict if a certain redox reaction is spontaneous. Under standard conditions, the cell potential is the potential of the reduction process minus the potential of the oxidation process. Positive values of E indicate a spontaneous process and vice verse.

$$E°_{cell} = E°_{red} - E°_{ox} \tag{2.1}$$

2.1.3. Gibbs free energy and Nernst equation

There is also another measure to determine if a process is spontaneous, namely the Gibbs free energy, Δ G. At constant temperature and pressure, the relationship between the cell potential in equation 2.1 and the Gibbs free energy is as follows:

$$\Delta G = -nFE = \Delta G° + RT\,ln Q \tag{2.2}$$

In this equation, n represents the number of moles of electrons transferred in the reaction and F stands for the Faraday constant, which is 96485 C/mol, the electrical charge of 1 mol of electrons. The Gibbs free energy is a useful thermodynamic quantity that describes the maximum useful work that can be done by a system on its surroundings. Counter-intuitive, a negative value indicates a spontaneous process. The magnitude of the value indicates the amount of work. Vice verse, a positive value indicates the minimum amount of work that must be done to cause the process to occur. Practically, due to inefficiencies a non-spontaneous process needs more work than this theoretical value.

Because the Gibbs free energy can also be related to the quantity for equilibrium constant K, equations 2.1 and 2.2 can be combined and rewritten.

$$E° = \frac{\Delta G°}{-nF} = \frac{-RT\,lnK}{-nF} = \frac{RT}{nF}\,lnK \tag{2.3}$$

In this equation, R stands for the gas constant (8.314J/K mol), T stands for the temperature in Kelvin and K for the equilibrium constant K. equation 2.3 is the prelude to the Nernst equation, which described the process of decreasing voltages of a voltaic cell as the cell discharges. Previously, the conditions were assumed to be constant, including the concentrations of the participating re-dox chemicals. But as the concentration logically changes as the reaction takes place, the standard conditions can not be assumed for a working battery. Therefore, the equilibrium constant K is replaced for the quantity Q which is the reaction quotient regarding the concentrations at a given moment. The Nernst equation can be obtained by combining and solving equation 2.2 and 2.3. Under room temperature (T=298K), this leads to equation 2.4.

$$E = E° - \frac{RT}{nF}\,lnQ = E° - \frac{0.0592V}{n}\,logQ \tag{2.4}$$

This equation forms the theoretical basis for the stability window of water, which is a very important topic in aqueous sodium-ion batteries. Looking at the Nernst equation, it is logical to see why the pH value of water influences the position of the stability window. At high concentrations of protons (hydrogen cations), it is easier to form hydrogen gas (a reduction reaction) than at low concentrations. Therefore, the Pourbaix diagram for water contains a downwards slope for increasing pH values.

2.1.4. Capacity and energy density

The capacity and the energy density are two important parameters for batteries. The amount of charge that can be stored per weight or per volume is called specific energy (or capacity) and capacity density, respectively. The capacity is determined by the number of charge carriers that can be intercalated or bound to the anode or cathode material. Anode and cathode material often have different capacities, which is an important factor to take into account when designing a battery. Generally, the energy density of a full battery is lower than the energy density of the active electrode materials. This is caused by the addition of the weight of the non-active components of the battery, that do not contribute to the capacity. The specific energy is often expressed in milliampere-hour, which is a convenient unit for further calculations. The commonly used expression is given in equation 2.5

$$C = \frac{x_{max}F}{M_{host}3.6} \tag{2.5}$$

2.2. Carbon-based anodes

There are a number of advantages of carbon based organic electrodes, including the non-conventional fabrication, high flexibility and ability to undergo large volume changes. But most appealing, organic electrodes can be prepared using biologically derived materials making them promising candidates in sustainable energy storage. [21, 23, 48, 60]

The most well known carbon-based electrode material is graphite, which consists out of many 2 dimensional layers of hexagonal connected carbon atoms. Other than in lithium-ion batteries, graphite does not intercalate sodium atoms reversibly. Other carbonaceous materials such as petroleum cokes, carbon black, pitch-based carbon-fibers, polymers and hard-carbons have been demonstrated to insert sodium.[50]

Research for variants of polyimides made from N,N'-diamino-1,4,5,8,-naphthalenetetracarboxylic bisimide (ND) emerged decennia ago, when ND's showed high glass transition temperatrue, imporoved precessability and long-term thermal stability.[10] Also their application in organic semi-conductors have been researched, because of their strong electron-withdrawing ability.[14] It took roughly 20 years until the applicabiltiy of

ND's as battery electrode material was researched by numerous scholars.[6, 9, 22, 33, 43, 47, 52, 61] The research covered both the application of ND variations in polyimides, which are long chains of interconnected molecules, and the application of ND in crystal form as electrode material. As in many cases, the lithium related battery research precedes the sodium related battery research.

N,N' –bis(methyl)- 1,4,5,8-naphthalene diimide

The NDMe crystal structure was obtained from the experimental data provided by Krishna et al (2016). The crystal structure of NDMe consists of two different lines of twisted molecules in Y direction. In other words, identically oriented molecules are stacked in parallel in straight lines. The two lines are built up similarly, but the molecules in the first line show a twist compared to the molecules in the second line. In this way, the crystal structure could be seen as a 'zipper' of twisted interlocked molecules. This zipper like configuration shows different possible spots for sodium atoms to reside, assuming solely oxygen atoms to attract sodium atoms, and looking at the places where oxygen atoms come close in this crystal. The molecular configuration and crystal structure of NDMe are presented in appendix A. In table 2.1 the lattice parameters from experimental data is presented.

Table 2.1: Lattice parameters of NDMe as derived from experimental data by Krishna et al. [26]

Lattice Parameters			
Length scale	Distance in Å	Angle	Degrees
a	4,6215	α	90,00°
b	8,019	β	93,99°
c	17,024	γ	90,00°

N,N' –bis(p-tolyl)- 1,4,5,8-naphthalene diimide

Like the NDMe, the crystal structure of NDTo was obtained from existing experimental data. Again a flat 'core' of the molecule is present, surrounded by two flat side groups that are both twisted regarding the core of the molecule, but located in the same plane. The twists from the core molecule have angles of roughly 172°to the outward plane and 68,5°to the side-ward plane. The crystal structure of NDTo shows many similarities with the crystal structure of NDMe. The NDTo also shows two different lines that consist of symmetrically positioned molecules in the Y direction. However, the molecules from the two different lines are twisted with respect to each other. It is in the way of how these lines of molecules are twisted where the crystal structure of NDTo differs significantly from that of NDMe. The side groups of NDTo are all roughly pointing in the same direction, where the side groups of NDMe clearly did not. The molecular configuration and crystal structure of NDMe are presented in appendix B. In a similar fashion, the different lines are labelled 'Alpha', 'Beta right' and 'Beta left'. The side groups of the molecules are positioned in a way that resembles the 'zipper' configuration again, as earlier described. However, for NDTo this zipper-configuration is more clear, since the side groups are significantly taller than those of NDMe. The side group zipper is visible in figure B.3 in Appendix B

Table 2.2: Lattice parameters of NDTo as derived from experimental data by Krishna et al. [26]

Lattice Parameters			
Length scale	Distance in Å	Angle	Degrees
a	8,040	α	90,00°
b	4,324	β	92,36°
c	29,008	γ	90,00°

2.3. Density Functional Theory Calculations

Density Functional Theory (DFT) is a calculation method used in physics, chemistry and materials science that is based on quantum-mechanical principles. It is presently the most successful and also most promising approach to compute the electronic structure of matter.[7] The development of materials science in the past decades has led to the growing need to understand the fundamental principles and phenomena determining the properties of materials.[15] The laws of quantum-mechanics govern the interactions between atoms and electrons, thus any computational method solving many-atom, many-electron systems must incorporate the basic quantum-mechanical equations. DFT achieves this, providing insights in the electronic structure of molecules, crystals, surfaces and other body systems consisting out of atoms.

The original formulation is based on the electron density and provides the ground state properties of the molecular system. The generalized formulation is modified to make DFT more suitable to deal with a wide range of systems. The mathematical theorems of Kohn and Honenberg and equations defined by Kohn and Sham are the basic principles of DFT. Insights in the nucleus and electron positions in atoms are necessary when studying the atomic behaviour. As the mass of an electron is much smaller than the mass of a proton or neutron (roughly 1837 times), Born and Oppenheimer stated that the electron cloud would react much faster to the changes of the surroundings than nuclei would. From this, they stated that the problem of defining the electron and nucleus positions could be separated into two mathematical problems. This assumption is called the Born-Oppenheimer (BO) approximation, and allows the wave-function of a molecule to be separated into an electronic and a nuclear component, as shown in equation 2.6.

$$\Psi_{total} = \psi_{electronic} \times \psi_{nuclear} \tag{2.6}$$

Following the assumption that electrons react much faster to the surroundings than nuclei leads the justification to consider the positions of the nuclei of the treated cluster as fixed. The stationary electronic state can now be described by a wave-function, aligning with the time-independent Schrödinger equation.

$$H\Psi(r_1, r_2, ..., r_N) = E\Psi(r_1, r_2, ..., r_N) = \Big[T + V + U\Big]\Psi = \left[\sum_i^N \Big(-\frac{\hbar^2}{2m_i}\nabla_i^2\Big) + \sum_i^N V(r_i) + \sum_{i<j}^N U(r_i, r_j)\right]\Psi \tag{2.7}$$

In this equation, the system contains N electrons, E stands for the total energy and is built up by the kinetic energy T, the potential energy from an external field due to positively charged nuclei V and the electron-electron interaction U. V is system dependent, but the operators T and U are universal for all N-electron systems.

The first theorem by Kohn and Honenberg states that the external potential and hence the total energy is a unique functional of the energy density. Together with the second theorem, that states that the density that minimizes the total energy is the exact ground-state density, simplifications in the Schrödinger equation can be made. The electron density can be varied until the energy of the functional becomes minimal, if the true functional is known. Now, the functional can be split into two terms. The known term includes the kinetic energy of the electron, the Coulombic interactions between the electrons and the nuclei, the interaction between electrons and the interactions between nuclei.

Kohn and Sham were able to express a set of equations that each involve a single electron. By doing this, the problem turned into single electron wave functions that only depend on three spatial variables. The Schrodinger equation can now be rewritten into the so called Kohn and Sham equation:

$$\left[\frac{\hbar^2}{2m}\nabla_i^2 + V(r) + V_H(r) + V_{XC}(r)\right]\Psi_i(r) = E_i\Psi(r) \tag{2.8}$$

In this equation the contribution of V(r) defines the interaction between an electron and the atomic nuclei. The term V_H(r) is called the Hartree potential and defines the Coulombic repulsion between the electron and other electrons. V_{XC}(r) defines the exchange-correlation energy, which entails the difference between the real

and non-interacting kinetic energy plus the non-classical electron interaction. This term can also be seen as a collection of all the unknowns.

The Kohn Sham equations can be solved in an iterative way, firstly defining an initial trial electron density n(r). From this point, the single-particle wave function can be calculated, leading to a new electron density. At the point the calculated electron density is equal to the the input density, the ground-state electron density is found. From this, the total energy can be calculated. If the ground-state is not reached, the trial electron density needs to be altered.

2.4. VASP

The Vienna Ab initio Simulation Package (VASP) is a computer program for atomic scale materials modelling. It is a pre-packaged code that solves the Schrödinger equation using approximations for the energy and forces. It is widely used for ab initio electronic structure calculations and quantum-mechanical molecular dynamics.

The successful application of DFT as a tool to gain insights in the fundamental properties of materials involves three steps. First, the engineering problem needs to be translated into a computable atomistic model. Then, the computation of the required physicochemical properties can take place. Lastly, the simulation results have to be valdiated by the comparison of experimental data. [15] Thus, in order to make calculations with VASP the system of interest needs to be specified. Information about the atomic structure, the crystal structure, electronic structure and the convergence parameters are essential for VASP and can be specified in input files. There are 4 input files, namely 'POSCAR', 'POTCAR', 'INCAR' and 'KPOINTS'. These will be briefly explained below.

The crystal structure is defined in the POSCAR file, based on the coordinates of the atoms in a crystal lattice. Based on experimental data from literature, the crystal structures of many compounds are available. A crystal structure can also be made and modified by 3D molecular software like Materials Studio. The specification of the different types of atoms present in the crystal structure is done in the POTCAR file. The POTCAR file should hold the pseudopotentials for all the present elements, which is a modified expression for the potential that enables sovling the Schrödinger equation. It is not needed to specify the pseudopotentials for elements that do not occur in the crystal. Introducing new elements into the lattice, which will be done in the process of sodium insertion, thus requires the psuedopotentials of sodium to be added to the POTCAR file.

The electronic constraints for the calculations are specified in the INCAR file. Also the settings for the accuracy, starting point, cut-off energy and manximun number of ionic steps et cetera, are specified in in the INCAR file. The KPOINT file describes the division of the calculation over the reciprocal space. Higher K-point settings will generally result in more accurate calculations, which will require more calculation power and time. To find the balance between accuracy and CPU time, it is useful to perform a convergence test. From a certain point, higher K-points setting will not lead to more accurate calculation outcomes, but will exponentially increase the CPU time.

2.5. Van der Waals correction

There is ground to believe DFT calculations for large organic crystals should be corrected by the so called Van der Waals correction.[4] The Van der Waals correction is named after the Van der Waals forces, which are weak intermolecular forces. In order to understand the fundamental principle behind the Van der Waals corrections in the DFT calculations, insights on the intermolecular forces as described by Brown e.a. in the reference book *Chemistry, The central science* are used.[3]

There are a number of forces holding particles together which can be categorized in intramolecular forces, or chemical bonds, and intermolecular forces. Intramolecular forces consist out of ionic bonds, metallic bonds and covalent bonds, and are generally much stronger than the intermolecular forces. This translates in the fact that it requires roughly 25 more energy to break up one mole of HCl than to vaporize it. The intermolec-

ular forces consist out of the dispersion force, dipole-dipole force and the hydrogen-bonding force. There are many properties of a substance including boiling points that reflect the strength of intermolecular forces. The larger the intermolecular forces, the higher the boiling point, as it will require more energy to separate the molecules. The dispersion force and the dipole-dipole fore are the weakest intermolecular forces and are collectively called 'van der Waals forces' after Johannes van der Waals, who researched the deviation of gases from ideal behaviour and arrived at the significance of the intermolecular forces. All the intermolecular interactions are electrostatic and get stronger as the magnitude of the charges increases, but weaker as the distance between charges increases. This is the main reason why intermolecular forces are generally much weaker than intramolecular forces, as the distance between molecules (inter) is often way larger than the distance between atoms within the same molecule (intra).

2.5.1. Dispersion forces

The first type of van der Waals force is called the (London) dispersion force, first proposed by German-American physicist Fritz London. It can be described as the attractive force of the instantaneous dipole induced by the motion of electrons in neighbouring atoms. This means that even in neutral or nonpolar atoms or molecules, the instantaneous distribution of electrons can be different than the average distribution. The strength of the dispersion force depends on the polarizability, which is the ease with which the charge distribution is distorted. In general, polarizability increases with increasing molecular weight, which means that the dispersion forces play a bigger role in heavier molecules. Next to the weight, also the molecular shape influences the magnitude of dispersion forces. When a larger surface of the molecule is available to come in contact with surrounding molecules, the intermolecular attraction will be greater.

2.5.2. Dipole-dipole forces

The second type of van der Waals force is caused by the presence of a permanent dipole moment in polar molecules, and is called the dipole-dipole force. This force is the result of the electrostatic attraction between the partially charged ends of two neighbouring molecules. Whenever a partially positive end of one molecule comes closer to a partially negative end of another molecule, this force will be attracting, where it will be repulsive if the ends are similarly charged. The presence of a dipole-dipole force in a molecule can lead to higher boiling points compared to comparable (weight, atomic structure, size) molecules, because the attractive dipole-dipole force prevents the molecules to move apart.

3

Research Methods

This chapter contains the actions to be taken to investigate the research problem as stated in the research objections in section 1.4. The main aim of this chapter is to describe the way in which the results are gathered and the way in which the data is analyzed The application of specific procedures, techniques and theory is described in two sections about the simulation protocol and the sodiation process.

3.1. Proposed nomenclature

In order to ease the process of interpretation of the sodiation pathway, a number of rules for naming were proposed. First of all, it is very important to maintain an uniform three-dimensional perspective in Material Studio in order to work consistently. The most insight into the configuration of the crystals was obtained with the unit cell positioned in such a way, that the X-axis was pointing upwards, the Y-axis was pointing outwards of the plane, and the Z-axis was pointing to the right. This perspective is kept constant throughout this report unless explicitly mentioned otherwise.

Secondly, the crystal structure of NDMe and NDTo consists of two different lines of twisted molecules in Y direction. Thus, identically oriented molecules are stacked in parallel in straight lines. The two lines are built up similarly, but the molecules in the first line show a twist compared to the molecules in the second line. In this way, the crystal structures of the two compounds could be seen as a 'zipper' of twisted interlocked molecules. For NDTo this zipper-like configuration is more clear than that of NDMe, since the side groups in NDTo are significantly taller than those of NDMe.This zipper-like configuration shows different possible spots for sodium atoms to reside, assuming solely oxygen atoms to attract sodium atoms. The central line of NDMe molecules is to be named the *'Alpha'* string. In the interpretation of the simulation results, the molecule from this line will be the reference point. The two twisted line to the sides are called *'Bravo left'* string and *'Bravo right'* string, for the strings on the left and right, respectively.

Thirdly, the oxygen atoms must be numbered in order to distinguish between them. As there are four oxygen atoms per molecule of NDMe or NDTo, the oxygen atoms are numbered as follows: O1, O2, O3 and O4. Assuming the sodium atoms to reside near one of those four oxygen atoms, the area round the numbered oxygen atoms are called 'assumed logical binding' (ALB) spots. In figure 3.1 the sodium binding spots are indicated in red. The oxygen atom closest to a sodium atom is called the 'true host', which will be useful to indicate clearly how the sodiation process takes place.

3.2. VASP settings

As explained briefly in section 2.4, VASP requires four different files that describe the necessary information about the DFT calculations to be performed. Shortly, the settings for these files will be described below.

POSCAR file The positions of the atoms in the crystal lattice are defined in the POSCAR file. By using the 3D molecular software of Materials Studio, the configuration to be calculated for each calculation is exported and converted into a new POSCAR file. After the DFT calculation is finished, the positions of the atoms in the relaxed structure is imported again in Materials Studio in order to interpret it and repeat the cycle.

POTCAR file The POTCAR file is simply made by adding the psuedopotentials for the individual atoms from the database into one file. It is of crucial importance to put the elements in the same sequence as the POSCAR file is difined. In this ways the positions of e.g. the carbon atoms are coupled to the pseudopotentials of carbon.

INCAR file All other input parameters for the calculation is defined by the INCAR file. According to best practice and experience with DFT calculations within our own research group, the INCAR settings were defined. The INCAR settings were not changed throughout the course of this research and will thus not be elaborately discussed here. The only INCAR setting of importance in this research is the definition of the Van der Waals correction model, which will be discussed in section 3.4. An complete overview of the used INCAR file settings can be found in appendix C.

3.2.1. K-POINTS file

The K-POINTS file (K-points settings) contains instructions of the grid over which the density functional calculations are performed. Generally speaking, the settings define the resolution of the calculations. The outcomes of the calculations are thus affected by the choice of the K-point settings. A suitable grid setting is necessary for calculations to be made. There is a number of different types of grids, of which the Monkhorst-Pack type is often used and provides much freedom to change the settings. In the Monkhorst-Pack type K-point settings, the grid is equally spaced in reciprocal space. The grid should be symmetric with the 1st Brillouin zone of the crystal to obtain the best results. This is done by relating the parameters of the grid with the parameters of the crystal lattice. This means that the lattice parameters should be proportionally inversed to obtain matching grid parameters in the K-point settings.

In cubical unit cells this would not be a difficult task, as the lattice parameters are equal. However, many organic crystals know more complex crystal lattice configurations, like the tetragonal, orthorhombic, trilinic and rhombohedral configuration. In the case of both NDMe and NDTo the initial lattice structure as derived from experimental research [26] is monoclinic, with typically different vector lengths (a,b,c) and angles: α=γ=90°, $\beta \neq 90°$. The experimentally determined crystal parameters of NDMe and NDTo is given in table 2.1 and 2.2.

The method to find an appropriate K-point setting was derived from insight out of our own research group [25, 58]. A number of K-point settings with invisibly proportional dimensions with respect to the crystal lattice parameters is tried for the empty host structure of NDMe and NDto. The sequence is logically from small settings toward larger settings. When a consecutive outcome in relaxation energy of a modified K-point settings of 1meV is observed, the energy can be regarded as converged. From that point onward, higher K-point settings would not significantly yield better results, but would usually require more CPU time. The value of 1 meV is based on the insight that the thermal energy kT at room temperature is roughly 25 meV. An uncertainty of less than 5% is therefore assumed reasonable. A second consideration is the uniformity of K-point settings between the different organic crystals NDMe and NDTo. It is preferred to obtain similar K-point settings for NDMe and NDTo, as this would make comparisons more scientifically valuable.

3.3. Sodium insertion protocol

In order to visualize the sodiation process of NDMe and NDTo, a number of simplifications have to be made regarding the visualization of the molecular structure. Because the NDMe and NDTo molecules in the crystal lattice are rotated in three dimensions with respect to the surrounding molecules, it is a difficult but important task to come up with a numbering protocol using a two dimensional figure. The first simplification is regarding the 'skeleton' of the molecule, i.e. the benzene rings with Methyl or Tolyl side groups on both ends. This skeleton will be considered as a flat oval plate, indicated by the grey colour in figure 3.1.

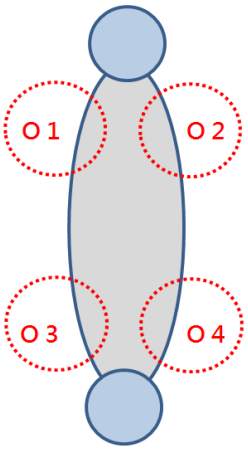

Figure 3.1: Visual simplification of NDMe. Sodium binding spots are indicated in red.

The side groups are assumed to be spherical balls, indicated by the blue colour in figure 3.1. The sodiation simulation protocol works the same for both NDMe and NDTo. The crystal lattice derived from literature existed of two molecules per unit cell. This means that per unit cell, in total eight sodium binding spots are available, assuming a maximum sodium occupancy of 1 sodium atom per oxygen atom. The protocol consists of 4 steps. Because the crystal unit cell in Materials Studio exists of in total two molecules of NDTo, the amount of sodium atoms per sodiation step that is expected to bind to one molecule of NDTo is 1. This means that per step 2 sodium atoms are placed at ALB-spots, which are determined based on the notion that most documented TiO_2 compounds show distances between the oxygen and sodium atoms of in between 2,1-2,4 Å, after relations.[58] An alternative would be to perform Molecular Dynamics (MD) simulations, but taking the large molecular size into account and realizing the exceptionally long calculation times required for MD on large molecules, this method is not found feasible.

Dependent on the positioning of the molecules in the crystal lattice, the oxygen atoms from different molecules can create so called Dual Binding Spots (DBS), Triple Binding Spots (TBS) and Quartet Binding Spots (QBS). The common characteristic of these spots is that one sodium atom is 'shared' between two, three or four oxygen atoms. A sodium atom is shared when the distances between the surrounding oxygen atoms are approximately equal. Unless mentioned otherwise, the closest oxygen will be considered to be the true 'host' of the sodium atom.

With the identification of ALB-spots, the sodiation protocol for the DFT calculations can be set up. Basically the sodiation protocol is a repetitive and iterative process that contains a number of steps. Firstly, in Material Studio, the empty molecule is constructed based on the proposed molecular structure in literature. Secondly, two sodium atoms are added manually in different ALB-spots. As many configurations are constructed in this way as is deemed sufficient, with the requirement of showing a significant difference with other configurations.

Then, the set of configurations is transferred into PuTTY using FileZilla, and are all runned in VASP simultaneously to find their relaxation energy and molecular structure. After all the simulations have been completed, the results are interpreted in Excel and in Materials Studio and the the configuration that yielded the lowest relaxation energy is taken as the base structure in the new simulation round. This protocol repeats until the crystal is completely sodiated. The sequence of configurations that consequently yielded the lowest energy per simulation step, forms the thermodynamically most favourable sodiation pathway. Insight in this pathway is very valuable in order to analyze further results.

3.3.1. Enthalpy of formation

The (standard) enthalpy of formation is a very useful parameter to gain insight in the thermodynamic feasibility of a transition process. It is defined as the change of enthalpy during the formation of 1 mole of substance compared to the enthalpy of formation of the elements it consists of, under standard conditions. The enthalpy of formation for the different phases can provide insight in the stability of the sodium insertion phases. The formation enthalpy can be calculated using the following formula:

$$E_{form} = E[Na_xNDz] - xE[Na_4NDz] - (1-x)E[NDz] \tag{3.1}$$

In this formula, x stands for the fraction of sodiation, E_{form} is the formation enthalpy of the specific phase, E[Na_xNDz] is the relaxation energy of the specific phase, E[Na_4NDz] is the relaxation energy of the completely full compound (NDMe or NDTo) and E[NDz] is the relaxation energy of the empty compound. From this formula it can be concluded that for fractions of sodiation 0 and 1 the enthalpy of formation will be zero. Furthermore, a negative value for any of the phases in between means a more stable state. When comparing the values of the enthalpy of formation for different configurations within one sodium insertion step, the most negative will thus represent the most stable state.

As the enthalpy of formation is calculated for all sodium insertion steps, the most stable states per step can be connected. A resulting curve is called the convex hull diagram and will be of vital importance to predict the voltage curve, also called the potential profile. When the most stable state of a specific sodium insertion phase lies above the line between the most stable states of the steps before and after, the specific sodium insertion phase is likely to be 'passed by' in the actual sodiation process. This process is called 'tunneling' and has an implication on the voltage profile. In order to take this possibility into account, formula 3.3 needs a modification:

$$V_{avg}(x_{n+1} - x_n) = -\frac{\Delta G°}{ze} = -\frac{E[Na_{x_{n+1}}NDz] - (x_{n+1} - x_n)E[Na] - E[Na_{x_n}NDz]}{(x_{n+1} - x_n)e} \tag{3.2}$$

V_{avg} now stands for the average voltage between two phases which can be arbitrarily chosen based on the insights of the formation of enthalpy and the convex hull diagram. $\Delta G°$ stands for the total change in Gibbs free energy ze represents the number of electrons involved in the reaction. The difference in sodiation fraction between the phases is represented by (x_n + 1-x_n). Formula 3.2 will be used in the determination of the potential profile.

3.3.2. Potential profile

From the enthalpy of formation values the voltage profile can be calculated. The voltage profile can predict the electrostatic force by which the organic crystals attract sodium atoms towards their binding spots. The voltage is calculated by using formula 3.3:

$$V(x) = \frac{E(Na_xNDz) - xE(Na) - E(NDz)}{xe} \tag{3.3}$$

In this formula, $V(x)$ is the voltage related to the sodiation, $E(Na_x)NDz$ represents the relaxation energy of the partially sodiated molecule, $xE(Na)$ stands for the enhalpy of formation of x number of sodium atoms, $E(NMz)$ represents the relaxation energy of the empty host structure and finally xe are the number of electrons added to the structure.

3.4. Van der Waals correction models

Van der Waals force apparently is increasingly significant in large and heavy molecules and molecules that have a permanent dipole. The organic molecules NDMe and NDTo do not have permanent dipoles, so dipole-dipole force can be neglected. However, due to their flat 'planar' shape, the surface area is dis-proportionally large. This means that the London dispersion force has to be considered to influence the intermolecular interaction significantly. Earlier research has shown a relation with molecule size and calculation errors for DFT settings not corrected for Van der Waals forces. [1]

Numerous correction models have been suggested previously to correct for these Van der Waals forces in DFT calculations. [4, 11, 12, 57] As stated on the website of VASP[**?**], most popular density functionals are unable to describe de Van der Waals interactions correctly. A pragmatic methods is to add a correction to the conventional Kohn-Sham DFT energy. There are several methods to compute the size of the correction, with different theoretical substantiation. To enable a Van der Waals correction method, the code tag (IVDW= x) should be added to the INCAR file, with a value of (0|1|10|11|12|2|20|21|202|4) on the place of the x. A short description is given per setting for IVDW.

- IVDW=0 adds no correction
- IVDW=1|10 enables the DFT-D2 method of Grimme. [11]
- IVDW=11 enables the zero damping DFT-D3 method of Grimme [12]
- IVDW=12 enables the DFT-D3 method with Becke-Jonson damping
- IVDW=2|20 enables the Tkatchenko-Scheffler method [57]
- IVDW=21 enables the Tkatchenko-Scheffler method with iterative Hirshfeld partitioning
- IVDW=202 enables the many-body dispersion energy method (MBD@rSC)
- IVDW=4 enables the dDsC dispersion correction method

All of the listed Van der Waals correction methods will be tested on the empty host structure to see which method leads to the best approximation of the experimental data of the lattice parameters. From that point on, the most appropriate method will be used in all further DFT calculations for the organic structures upon sodium insertion. The series of uncorrected calculations can then be compared to the series of corrected calculations to gain insight in the significance and importance of the Van der Waals corrections in the computational calculations.

4

Computational Results

The computational results are presented in four different sections. First, the K-point convergence for NDMe and NDTo are described, which determined the appropriate settings of the consecutive computations. Then, an elaborate overview and description of the sodiation pathway for NDMe and NDTo is given in two separate sections. In the last section the significance of the Van der Waals corrections in the outcomes is showed.

4.1. K-point convergence

The main criterion for selecting an appropriate set of K-point is the convergence of relaxation energy. As explained in section 3.2.1, if the outcomes in relaxation energy of different K-point settings of 1meV is observed, the energy can be regarded as converged. From that point onward, higher K-point settings would not significantly yield better results, but would usually require more CPU time.

A range of K-point settings has been tried out for NDMe and NDTo in a trail and error fashion. A number of K-point settings resulted in a mismatch and yielded no calculation outcomes. The other settings were sufficiently appropriate to finish the DFT calculations. The results of the K-point convergence for NDMe and NDTo are summarized in 4.1. The calculated energies are plotted against the computational time. In the graphs, the green curves represent the relaxation energies, and the red curves the CPU time. On the x-axis a range of K-point settings are sorted by size with increasing size to the right. There is a clear resemblance

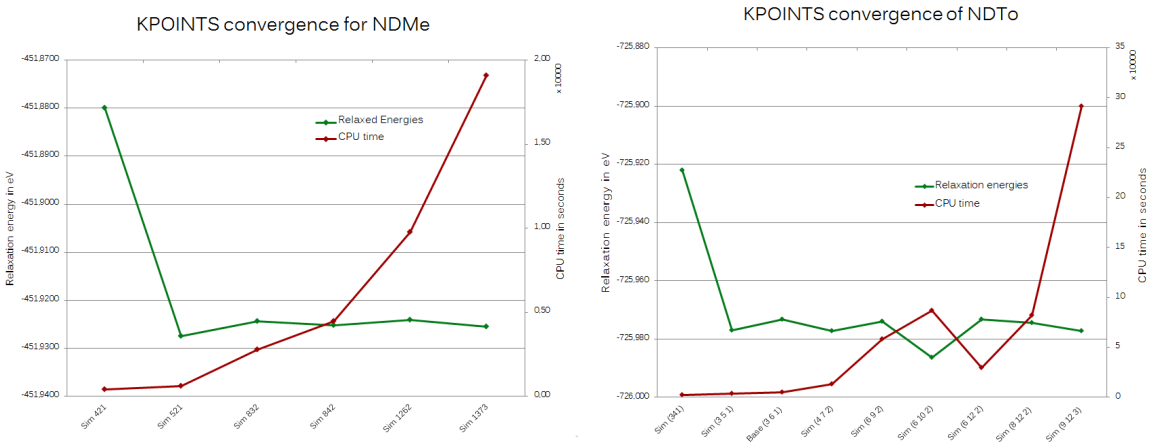

(a) for NDMe

(b) For NDTo

Figure 4.1: Convergence of the relaxation energy at increasing K-point settings.

between the two plots of NDMe and NDTo. The larger the K-point settings, the larger the CPU Time, and the smaller the deviation in the relaxation energy.

The selection of a suitable K-point setting for the NDTo calculation requires elaboration. In plot 4.1b two exceptions to this pattern can be noted. For the K-point setting 6-10-2 the calculated relaxation energy shows an unexpected deviation to the relaxation energies of closely related K-point settings. At K-point setting 6-12-2 the CPU time required is also remarkably low. When leaving out the relaxation energies of the calculations with K-point settings 3-4-1 and 6-10-2, all outcomes are in a range of 4 meV. Because the calculations with the K-point setting 6-12-2 has a remarkably low CPU time and relatively high grid parameters leading to a more detailed calculation, it is chosen as default setting for further NDTo DFT calculations.

The convergence of relaxation energy for NDMe is clearly visible, as the fluctuation of the green line quickly diminishes. Practically, all K-point settings from 8-3-2 to 13-7-3 resulted in relaxation energies that vary no more than 1,4 meV. Logically, the lowest K-point setting would have to be selected according to the previously determined method. But, as uniformity with the K-point settings of NDTo is scientifically relevant, 12-6-2 as chosen as K-point settings for further NDMe DFT calculations

4.2. NDMe sodiation pathway

The crystal lattice of NDMe without sodium inside is built up in a rather complex way. The O1 oxygen atom is positioned relatively close to the O4 oxygen atoms of the two molecules in row Beta line left (4,122Å and 3,591Å). This is also true for the distance between the O1 oxygen atom and the Alpha O2 oxygen atom of the molecule behind it (3,677Å) and the Beta O2 oxygen atom right (4,332Å).The distance to the O1 oxygen atom of the next molecule in the Alpha line is significantly larger (4,880Å). This is visualized in figure 4.2, where the atomic distances (in Å) between the O1, O2 and O4 oxygen atoms are shown. Only the distances between oxygen atoms smaller than 5 Å are considered. For the oxygen atoms at the O2, O3 and O4 locations, similar atomic distances are found. The most important insight derived from this empty host configuration is that the Alpha, Beta Right and Beta Left strings show a real 'interlocked' behaviour, like a zipper.

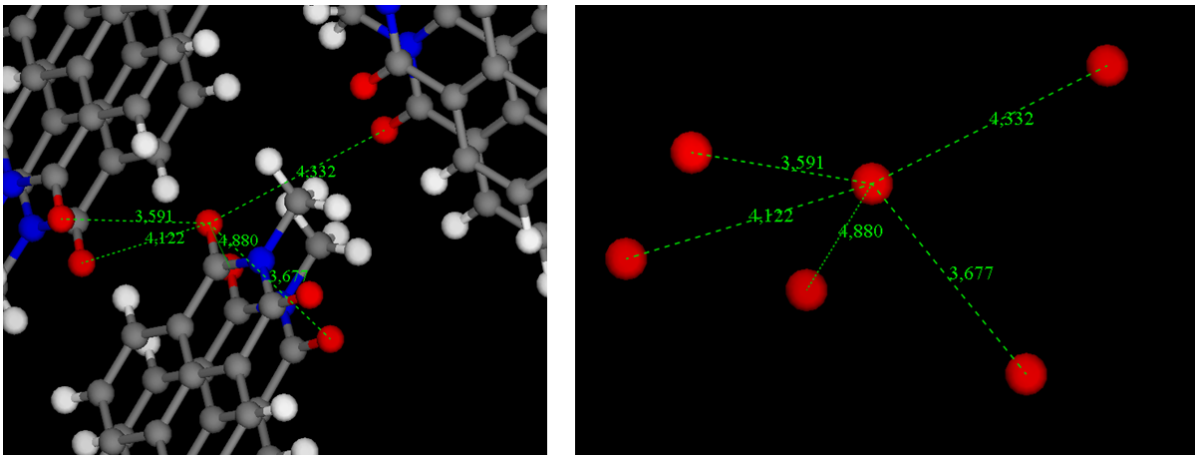

Figure 4.2: Empty host crystal structure of NDMe. Left: O1 oxygen atom with distances to surrounding oxygen atoms. Right: Overview of merely closely positioned oxygen atoms.

4.2.1. Step-wise sodiation

Using the predetermined sodiation protocol explained above, the sodiation pathway of NDMe is found. The first two sodium ions have a clear tendency toward the available Triple Binding Spots (TBS) near O2 and O3. This can be seen in figure 4.3. Upon insertion of the first two sodium atoms, the crystal structure of NDMe shows a total volume change of 11.37%, resulting in an increased distance between the oxygen atoms of different molecules, with only one exception: the distance between the Alpha O1 oxygen atom and the Alpha O2 oxygen atom behind it decreases. This leads to a change in the (b)axis of -0,87%, where the other

Table 4.1: Lattice parameter and volume change of NDMe upon sodiation.

	a (Å)	Δ a%	b (Å)	Δ b%	c (Å)	Δ c%	Δ V
Empty	4,88		8,018		17,656		
Step 1	5,373	10,10%	7,948	-0,87%	18,056	2,27%	11,37%
Step 2	6,341	18,02%	7,513	-5,47%	15,808	-12,45%	-2,19%
Step 3	6,727	6,09%	7,281	-3,09%	16,495	4,35%	5,88%
Step 4	7,205	7,11%	6,758	-7,18%	16,143	-2,13%	-3,64%
Total		47,64%		-15,71%		-8,57%	11,14%

two axes increase significantly, as shown in table 4.1.

The sodium atoms inserted in the second sodiation step resided in a similar fashion as in the first sodiation step, namely at TBSs. The O1 and O4 oxygen atoms are now centre of attention. Because after the second sodiation step, 4 TBSs are formed, this means that some oxygen atoms will have two sodium atoms in their vicinity. The happens in such a way, that two sodium atoms are 'sandwiched' in between the Alpha molecules, while the other two sodium atoms reside in the TBSs between the Alpha and Beta lines.

After the third sodium insertion, all oxygen atoms in the unit cell have two sodium atoms in their vicinity which are all situated in TBSs. The sodium atoms are still located in TBSs, although the true triangular positioning has changed in two cases. Because of the crystal symmetry, these two sodium ions are in fact repetitions of the same position. This can be seen in figure 4.4 at the TBS of O1 (front) and O4 (back). These sodium ions now show a significant preference to one of the oxygen in the TBS. Since double accounting must be avoided, this atom will be regarded as being hosted by the O1 oxygen atom.

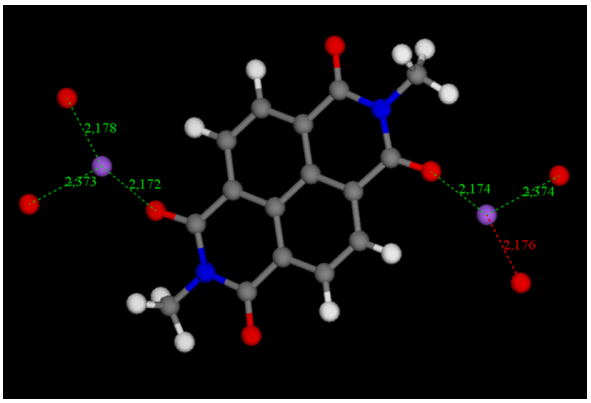

Figure 4.3: The positioning of the sodium atoms in the NDMe crystal after the first sodium insertion step with distances between surrounding oxygen atoms in Å

After the last sodiation insertion step, a number of remarkable observations can be made. To enhance the visibility of the distances between the relevant oxygen and sodium atoms, separate close-ups of each binding spot are included in figure 4.6

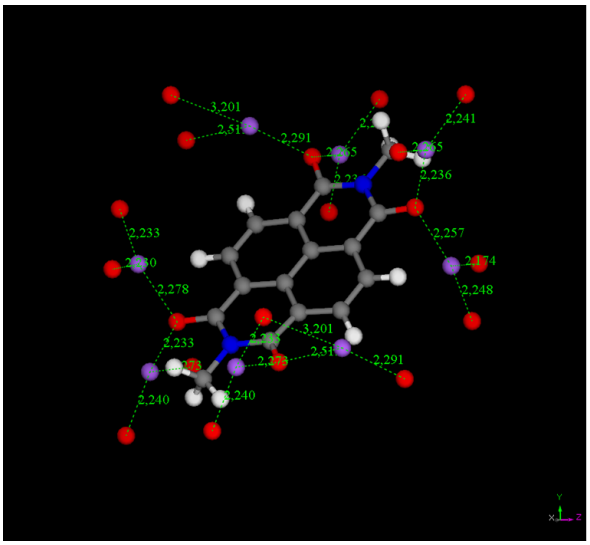

Figure 4.4: The positioning of the sodium atoms in the NDMe crystal after the third sodium insertion step with distances between surrounding oxygen atoms in Å

First of all, the sodium atoms are not symmetrically distributed around the NDMe molecule, what has been the case in previous sodiation steps. The oxygen atoms at O1 and O4 both share 2 sodium ions, one in a TBS and one in a DBS configuration with surrounding oxygen atoms. The oxygen atoms at O2 and O3 both share 3 sodium ions, of which 2 in a TBS and one in a DBS with surrounding oxygen atoms. This means that if all distances between oxygen-sodium are taken as equal, the O1 and O4 oxygen atoms 'possess' 5/6 sodium ion, where the O2 and O3 oxygen atoms possess 7/6 sodium ion.

Another remarkable observation is the structural change of the NDMe molecule. Both methyl side groups have made a 'kink' relative to the flat plane of the skeleton of the molecule. The side-group on top between O1 and O2, has made a kink forward, while the side group between O3 and O4 has made

a kink backwards. These kinks have an angle of approximately 160° and 130° respectively, and can be seen in figure 4.5. The kinks of side groups of the Alpha molecules is significantly different to the kinks in the side groups of the NDMe molecules in Bravo line. In none of the previous sodiation steps there has been significant kinks in the NDMe molecules.

Apparently the last sodiation step initiates a structural change to the host material. This is generally speaking unwanted since it demands high flexibility and strength from the host material for material degradation to be prevented. The volume changes and lattice parameters per sodium insertion step are presented in table 4.1. As can be seen in this table the total volume increases significantly twice, namely during the first and the third sodiation step. A slight decrease is observed in the second and fourth sodiation step. Looking at the change in the b-direction of the crystal lattice, presented in the third column in table 4.1, it is remarkable to see that upon sodiation the crystal lattice is decreasing after every step. This is in contrast with the lattice parameter in the a-direction, which is ever increasing upon sodiation.

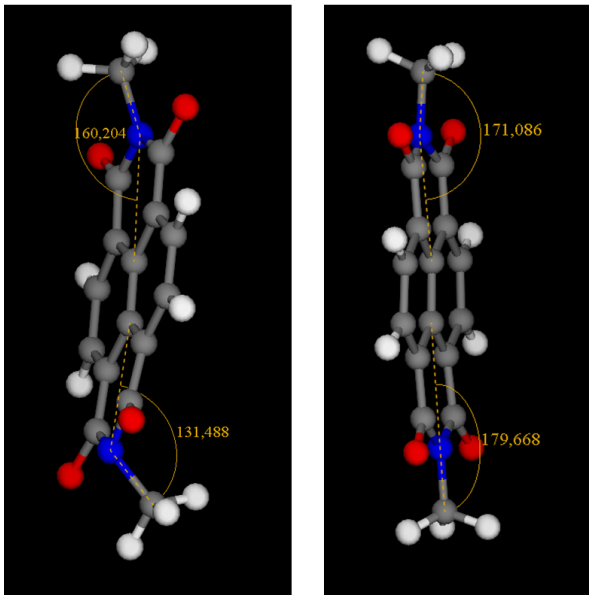

Figure 4.5: Kinks of the methyl side groups after the fourth sodiation insertion. Left: an Alpha molecule. Right: a Bravo molecule.

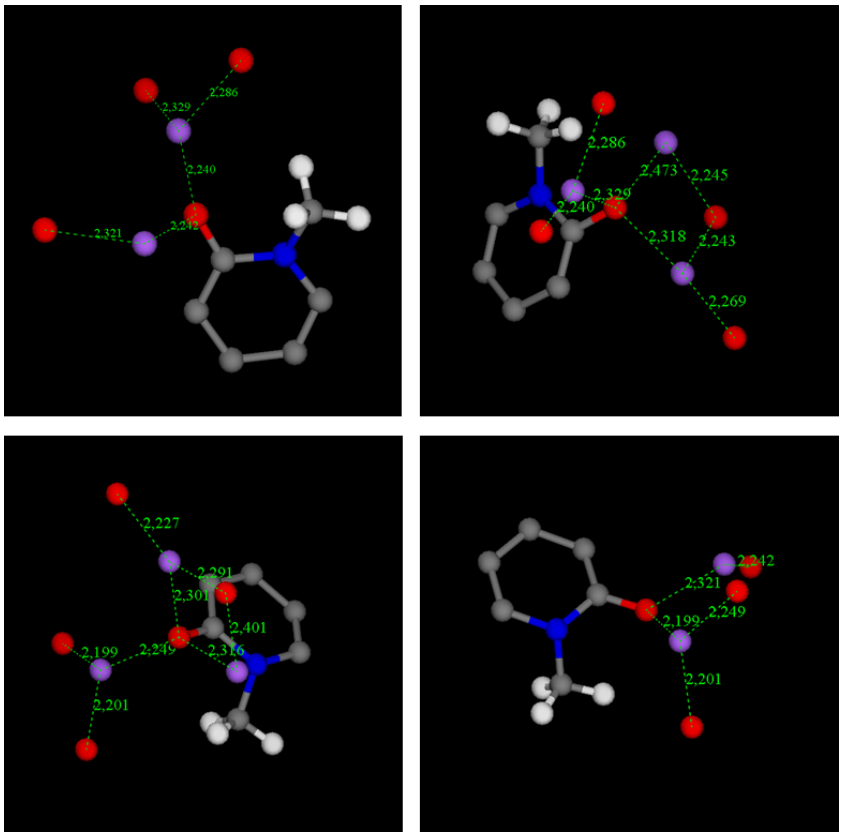

Figure 4.6: Close-up of the O1-O4 oxygen atoms with surrounding sodium and oxygen atoms and the inter-atomic distances in Å

4.2.2. Van der Waals corrections

In order to gain insight in the significance of the Van der Waals corrections, a completely new series of calculations were executed, based on the insights of the uncorrected NDMe sodiation pathway. To begin this, a set of calculations for the empty host structure with different Van der Waals correction models were performed.

As the enthalpy of formation of the experimental data as derived from Krishna et al. [26] did not include the enthalpy of formation, this could not be used as a criterion in the selection of the best Van der Waals correction model. The total volume change was thus taken as main criterion. Looking at the total volume of the unit cell, it is clear that the IVDW=11 correction model yields the best approximation of the experimental data. The total volume change is -0.42% with the lattice vector lengths (a), (b) and (c) changing 0.18%, -1.12% and 0.63%, respectively. Compared with the uncorrected calculations, this is remakably close to the experimental data, as the uncorrected calculations resulted in a unit cell volume mismatch of 9,73% with the experimental data [26]. The second best approximation is yielded with the correction model IVDW=12, that shows a higher volume change (-1,35%) but a lower enthalpy of formation than the correction model IVDW=11. The Van der Waals correction model of IVDW=11 was thus selected for further calculations. The overview of the calculation outcomes for different correction models is given in table D.1 in appendix D

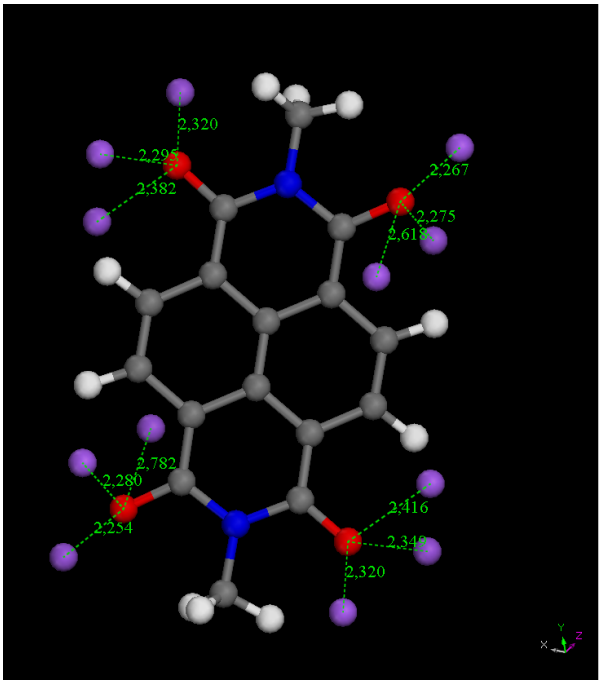

Figure 4.7: The configuration ant inter-atomic distances in Å of sodium atoms around the fully sodiated NDMe after relaxation with Van der Waals corrections.

Based on the insights of the uncorrected NDMe sodiation pathway as described before in section 4.2.1, the same configurations per sodiation step were tested with the added correction model. The sodiation pathway of the corrected calculations remains the same as the uncorrected calculations during the first, second and thirds sodiation step, but the lattice parameters differ significant structurally. The corrected calculations result in significantly smaller absolute values for the lattice dimensions and smaller volume changes per sodiation step. A complete overview of the results is provided in table E.1 in appendix E.

In the last sodiation step of the corrected calculations a remarkable deviation is observed in the relaxed configuration. Instead of the unequal distribution of the sodium atoms in the fully sodiated structure of NDMe as described earlier and showed in figure 4.6, the sodium atoms are now virtually perfectly distributed. All sodium atoms have resided in TBS, with comparable distances between the oxygen and sodium atoms. As all oxygen atoms of the NDMe molecule are surrounded by three sodium atoms, and all sodium atoms are surrounded by three oxygen atoms of surrounding molecules, every oxygen of the NDMe molecule is assumed to be sodiated 100%. The distribution of the sodium atoms in the fully sodiated NDMe as a result of the addition of Van der Waals correction model is showed in figure 4.7. Surprisingly, no significant kinks (as previously shown in figure 4.5) in the methyl side groups were observed this time in the last step. The significance of the Van der Waals corrections will be further described in the following sections on the enthalpy of formation and the voltage profile.

4.2.3. Enthalpy of formation

From the enthalpy of formation of the NDMe molecule in different sodiation steps, a convex hull diagram is produced which is showed in figure 4.8. A number of observations can be made from this diagram. Firstly, the convex hull diagrams for the uncorrected and the corrected calculations looks significantly different. The convex hull diagram of the uncorrected calculations is positioned structurally lower, with a maximum devia-

tion of roughly 0.6 eV at a fraction of sodiation of 0.5. A second observation is that the first sodiation step is obviously not thermodynamically feasible, as all relaxation energies are positioned above convex hull curve. This outcome predicts that the sodiation pathway of NDMe would 'skip' the first sodiation step where it only hosts two sodium atoms.

The third sodiation step is (with little margins) not thermodynamically feasible in the uncorrected calculation outcomes, but is just thermodynamically feasible with the corrected calculations. Another observation is regarding the deviation of relaxation energies of different configurations per step. There is a significant difference between the configurations per sodiation step, but there is no obvious difference in deviation between the uncorrected and corrected calculations. In other words, the scattering or spread of the data points is similar. This is true for all sodiation steps, except the last one. At full sodiation, the spread of data points of the corrected calculations is roughly twice as big as that of the uncorrected calculations.

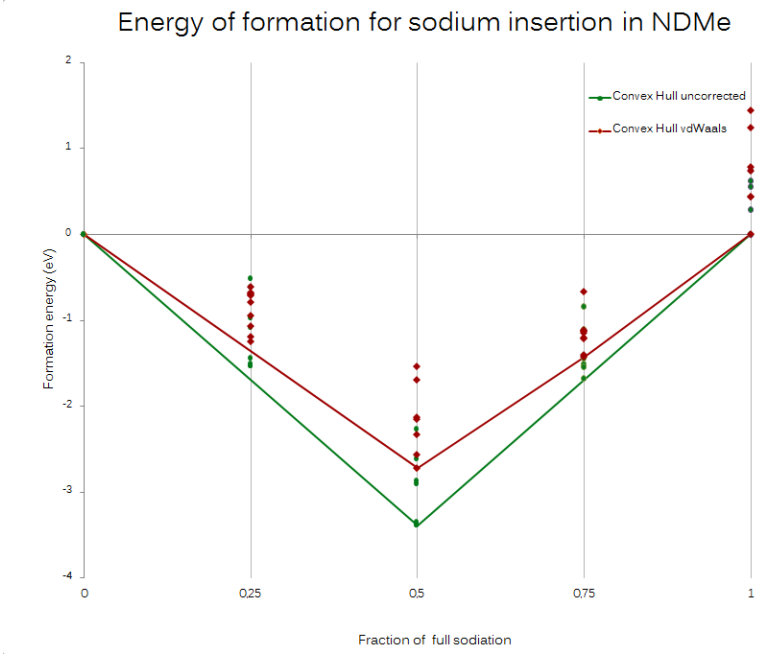

Figure 4.8: Convex Hull diagram of both the basic and the van der Waals corrected sodiation pathways of NDMe

4.2.4. Voltage profile

Related to the convex hull diagram and of comparable significance is the voltage profile of NDMe upon sodiation. Because the convex hull diagram provides the insight in the stable intermediate steps, the voltage profile has to be adjusted for that, using formula 3.2 as described in 3.3.2. The dotted lines in figure 4.9 reflect the situation without taking tunneling into account, and the continuous lines reflect the voltage profiles with tunneling taken into account. A voltage plateau just under 1.8V versus is observed for both the uncorrected and corrected calculation results between a sodiation fraction range of 0-0.5. From that point onward, the Van der Waals corrected calculations reveal two voltage plateaus at 0.45 V and 0.39 V versus Na/Na^+, and the uncorrected model reveals one plateau at 0.08 V versus Na/Na^+.

4.2.5. Change in lattice dimension

The change in volume of the unit cell is determined by the change in the vectors lengths (a), (b) and (c). For both the corrected and uncorrected calculations, the relative change in these lengths are visible in figure 4.10. The relative change in vector lengths is versus the empty host structure. As the first and third step are not found to be thermodynamically feasible in the uncorrected sodiation pathway, they are omitted from the volume change overview. Step one is omitted from the overview of the corrected sodiation pathway. There is much resemblance between the two triangular diagrams. Both diagrams show a significant increase in vector

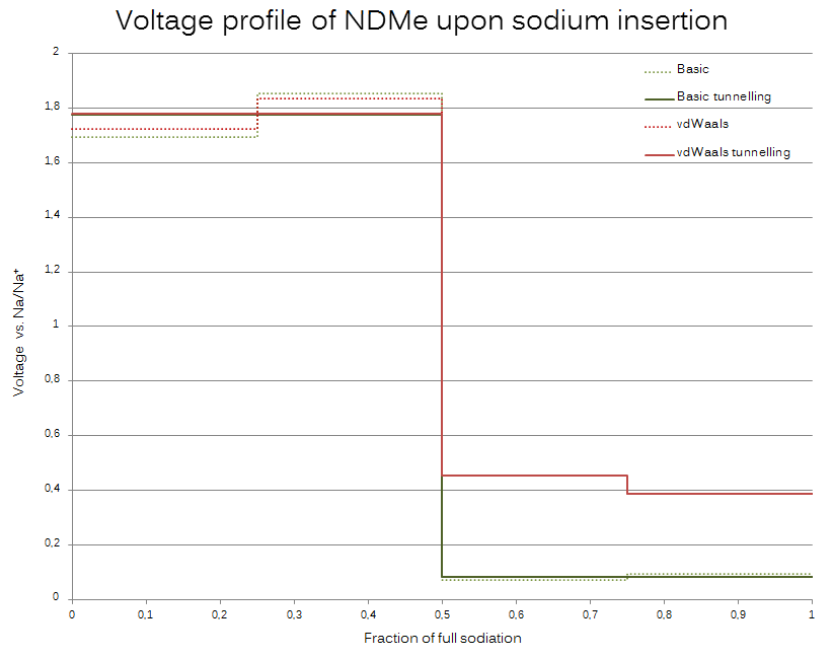

Figure 4.9: Voltage profiles of both the basic and the van der Waals corrected sodiation pathways of NDMe, in Volts vs. Na/Na^+

length (a) and less in length (c) and (b). The relative increase per sodiation step in the two different diagrams is also similar. Step two shows the biggest relative increase in vector length.

It is useful to compare the two changing unit cells, to see if a trend is observable. This could give more insight in the significance of the Van der Waals corrections as the fraction of sodiation increases. Looking at the differences in the absolute values of the difference of the change in relaxation energies, unit cell volume and lattice vector lengths between the corrected and uncorrected calculations as depicted in figure F.1 in appendix F, it is hard to see trends. It is obvious that the relaxation energy deviates more as the sodiation fraction increases, indicating a larger difference between the empty host structure and the fully sodiated structure in the calculations with Van der Waals corrections, than that of the uncorrected calculations. This is another way to explain the higher voltage observed in figure 4.9. The difference in the change of the total unit cell volume fluctuates in such a manner that a trend is not found. Looking at the vector lengths in figure F.1b in appendix F, the fluctuating pattern of the total unit cell seems to be primarily caused by the vector length c, which shows the biggest values. All three vectors are fluctuating without an apparent trend.

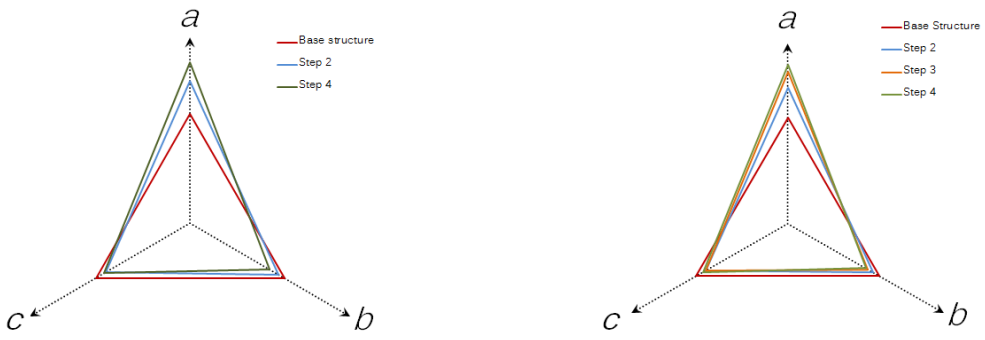

(a) without correction model

(b) with correction model

Figure 4.10: Relative volume change of the NDMe unit cell upon sodiation represented in the change in lattice parameters (a), (b) and (c).

4.3. NDTo Sodiation pathway

The first outcomes are concerning the relaxation configuration of the empty host structure of NDTo. The crystal structure of NDTo is built up in a rather complex order. Different to the structure of NDMe, there are not two but three oxygen atoms from neighbouring molecules from different strings (Beta right and Alpha), closer to the O1 oxygen atom from the Alpha string than the O1 oxygen atom of the molecule behind from the same Alpha string (4,651 Å). These three atoms are the O4 oxygen atoms from the molecules in the Beta left string (3,315 Å), the O2 oxygen atom from the Alpha molecule behind it (4,301 Å) and the O2 oxygen atom from the same molecule (4,588 Å). This means that the distance between O1 and O2 oxygen atoms from the same molecule is smaller than the distance between O1 and O1 of two neighbour molecules from the same string.

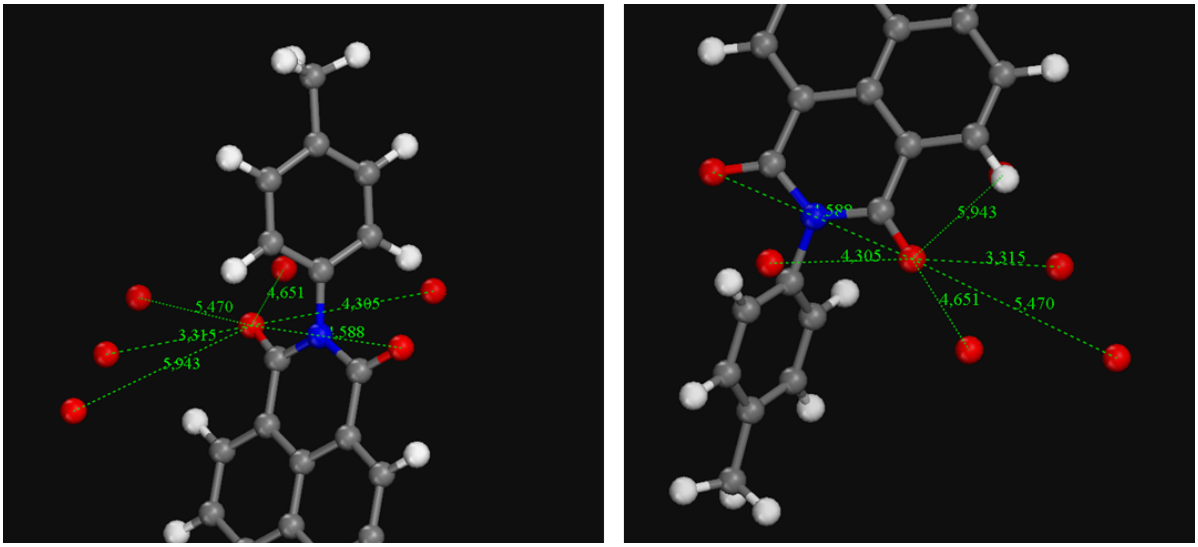

Figure 4.11: Left: O1 oxygen atom with distances to surrounding oxygen atoms. Right: O4 oxygen atom with distances to surrounding oxygen atoms.

The oxygen atom at binding spot O4 is an exact mirrored copy of the oxygen atom at O1 in the sense that the distances from O4 to the surrounding atoms are identical to the distances between O1 and surrounding atoms. In figure 4.11 this is visualized, showing the distances in Å indicated in the green colour. In figure B.1 in appendix B the oxygen atoms and surrounding atoms of O2 and O3 are presented. Similar to O1 and O4, these two binding spots are mirrored. The fact that these binding spots are mirrored indicates that the crystal structure of the empty NDTo is very symmetrical. It might be noted that spot O1 and O4 have a remarkable configuration compared to the previously discusses TBS and DBS. The Alpha O1 forms an almost straight rectangle with the Alpha O1 behind, and the two Beta left O4 atoms. This gives reason to belief that a sodium atom might reside in between these four atoms. This binding spot will be called Quartet Binding Spot (QBS).

4.3.1. Step-wise sodiation

Using the predetermined sodiation protocol explained in section 3.3, the sodiation pathway of NDTo is determined. The first two sodium atoms both reside at Quartet Binding Spots (QBS). The first one is situated between the O1 and O4 atoms of Alpha and Beta left, respectively. The second sodium atom is located in between the Alpha O4 and Beta right O1 atoms. In figure 4.12, the QBS are clearly visible on the left side of O1 and on the right side of O4. The distances between the oxygen atoms (red) and the sodium atom (purple) are in roughly the same range (2,283-3,008 Å). Looking at the distances between the sodium atom and the nearby oxygen atoms, it is clear that the O4 Binding spots in both Alpha and Beta are the true hosts with a distance of 2,283 Å.

In the second sodiation step, sodium atom number 3 and 4 were inserted in several different AL(b)spots, based on the lowest energy configuration of the first sodiation step. The sodium atoms reside on the O3 Dual Binding Spots (DBS). This means that the location of the sodium atom is in between two oxygen atoms, which are both Alpha O3 oxygen atoms. Also in the Beta lines the O3 binding spot are occupied with sodium atoms

after the second step. In figure 4.13 the location of the sodium atoms after the second sodiation step in NDTo is given.

When a sodium atom resides on a QBS, it in fact sodiates the surrounding oxygen atoms for just a quarter. But all the involved oxygen atoms in a QBS configuration have not 1, but 2 sodium atoms in their vicinity. This means that in the first sodiation step of NDTo, the O1 and O4 oxygen atoms were surrounded by in total 4 sodium atoms that all contributed for ¼ to the sodiation of the molecule. This adds up to a total sodiation number of one. In the second sodiation step, the sodium atom resides at a DBS, effectively sodiating the O3 oxygen atom half. But in a DBS configuration, the oxygen atoms are surrounded by 2 sodium atoms. Here the sodium atoms also contribute together for a total sodiation number of one.

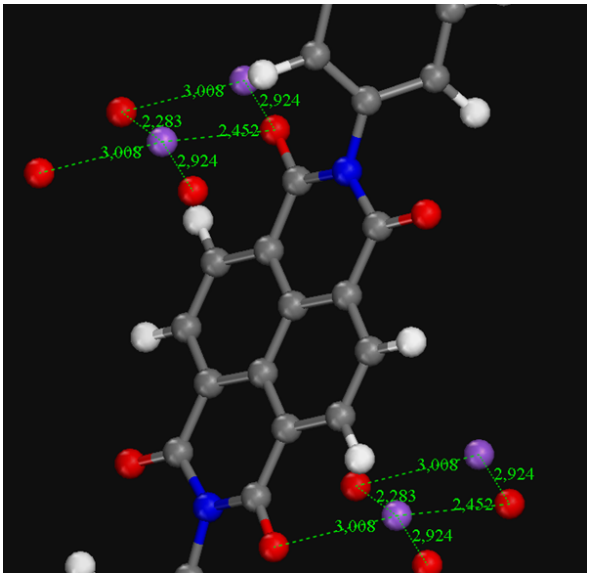

Figure 4.12: The positioning of the first two sodium atoms in the NDTo crystal with distances between surrounding oxygen atoms in Å

In the third sodiation step something remarkable happens. For the first time the molecules in the Alpha string show a different behavior to the molecules in the Beta string. This is because the molecules in the Alpha string fully sodiate at once, while the molecules in the Beta string do not receive extra sodium atoms. In Appendix C1 two figures are included that visually show the differences. This behavior is unexpected, since one of the AL(b)spots in the Alpha string seemed to be occupied one sodium atom in the centre of the QBS. This sodium atom had to be shifted significantly in order to create enough space for the second sodium ion. In Figure 14, the NDTo binding spots O1, O2, O3 and O4 are shown, including the distances between the oxygen atoms and surrounding oxygen and sodium atoms.

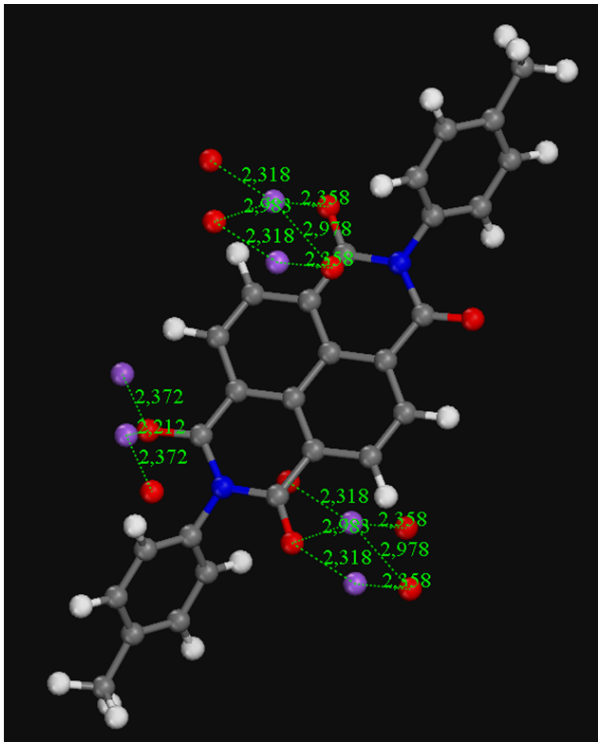

Figure 4.13: The positioning of the sodium atoms after the second sodiation step in the NDTo crystal with distances between surrounding oxygen atoms in Å.

The configuration after sodiation step 3 reveals a number of things. First of all, it might be clear that all the binding spots have 2 or 3 sodium atoms in its vicinity. Secondly, the binding spot O1 and O4 are exact mirrored copies, all distances with surrounding oxygen atoms being equal. The binding spots O2 and O3 are almost mirrored copies, but do show minuscule differences in the distances (2,339Å in O3 vs. 2.330Å in O2) between the oxygen and one of the sodium atoms. The configuration of the sodium atoms in O2 and O3 is set up like a classical DBS: each sodium atom has resided near perfectly in the middle of two O2 or two O3 oxygen atoms. Therefore each sodium atom is considered to contribute for ½ to the sodiation of the binding spot. Because every oxygen atom is surrounded by two sodium atoms , the oxygen atom is considered to be fully sodiated.

For the oxygen atoms at the binding spots O1 and O4 the inter-atomic distances reveal a more complex relation. Previously every sodium atom was surrounded by four oxygen atoms all situated in the same plane, a

new and more complex configuration has now emerged. Every atom is now part of two types of rectangles, of which one is a near perfect square. In figure 4.14, an enlargement of the atomic configuration of binding spot O1 is presented (left up). Seen from the NDTo molecule, the sodium atoms toward the back and toward the right make a near-perfect square plane with the two involved oxygen atoms. A rectangular shaped plane is visible on the left side. The distance between the central oxygen atom and the sodium atom to the left is significantly larger than the distance between the oxygen and the sodium atom to the right, namely 3,131Å instead of 2,283Å.

The atoms in the near-square position are relatively close to each other, and are therefore considered to be connected in a similar way as a double DBS, which leads to the statement that both oxygen atoms involved must be fully sodiated. The same reasoning holds true for the oxygen atom at binding spot O4, since it is shown to be an exact mirrored copy of the O1 binding spot.

In the last sodiation step the new sodium atoms reside at the two remaining available binding spots in the unit cell. Since two binding spots from the Alpha string have been filled in the third sodiation step, the remaining available spots in step four are both situated on the Beta molecules. In figure 4.15 an overview of the fully sodiated crystal structure of NDTo is given. Although the molecules in the Alpha and Beta strings are hosting the sodium atoms in similar ways, some differences can be seen in the angles and inter-atomic distances.

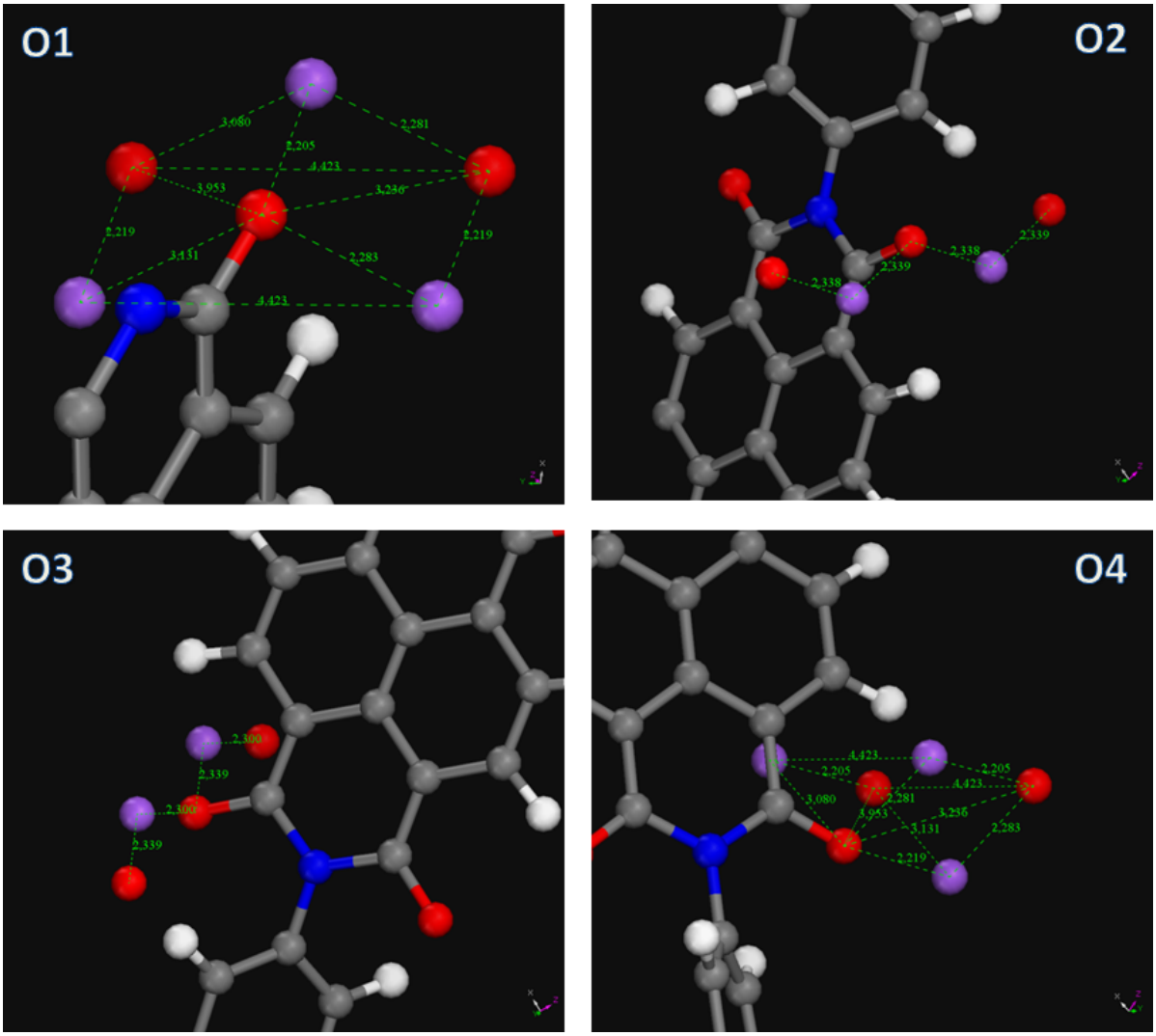

Figure 4.14: The positioning of the sodium atoms after the third sodiation step in the NDTo crystal with distances between surrounding oxygen atoms in Å

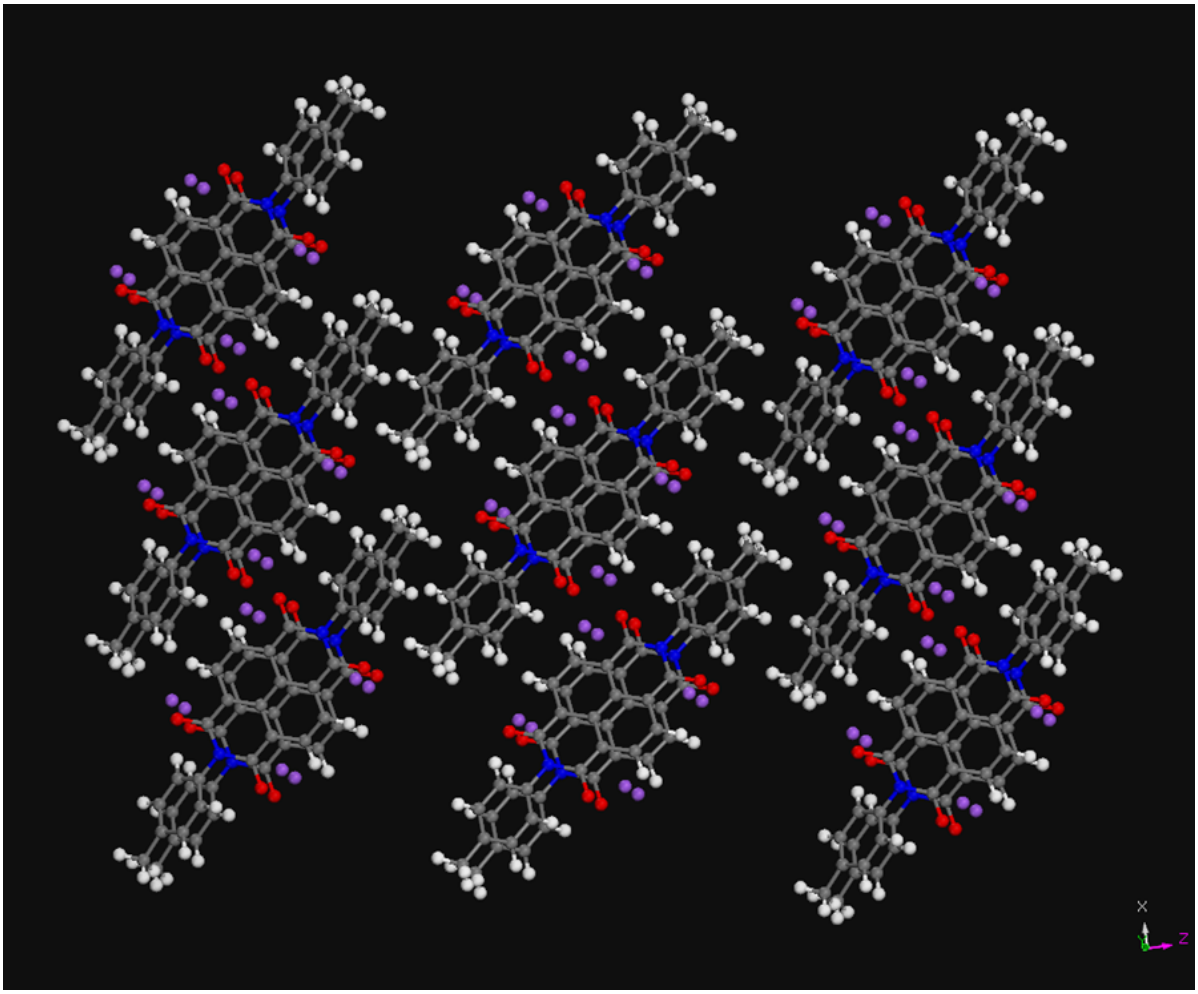

Figure 4.15: The overview of the fully sodiated crystal structure of NDTo.

The double layer reveals the three dimensional positioning of the sodium atoms. It can be concluded that all sodium atoms reside at the sheltered 'armpit' spots of the binding spots. This means that they have a tendency to reside at the centre-side of oxygen atom of the hosting NDTo molecule.

Another observation addresses the virtually unchanged crystal structure. It seems the molecules have hardly changed their shape or orientation upon sodiation. In order to verify this, the change in volume and lattice parameters upon sodiation is compared and presented in 4.2.

During the first two sodiation steps, the volume of the unit cell has slightly decreased. The attracting force of the sodium atoms in between the NDTo molecules could be an explanation for this. During the thirds sodiation step, however, the unit cell significantly expands, with a total volume change of 9,81%. This is the result of the expansion of both the alpha and beta axes 4,84% and 4,49%, respectively. The significant

Table 4.2: Lattice parameter and volume change of NDTo upon sodiation.

	a (Å)	Δa%	b (Å)	Δb%	c (Å)	Δc%	ΔV
Empty	8,179		4,651		29,798		
Step 1	8,514	4,10%	4,295	-7,65%	30,191	1,32%	-2,60%
Step 2	8,674	1,88%	4,233	-1,44%	30,01	-0,60%	-0,19%
Step 3	9,094	4,84%	4,423	4,49%	30,081	0,24%	9,81%
Step 4	9,386	3,21%	4,487	1,45%	29,767	-1,04%	3,61%
Total		14,76%		-3,53%		-0,10%	10,60%

expansion of the volume of the unit cell in the third sodiation step is the predominant reason why the total volume expansion of the sodiation process is rather high, namely 10,60%. To be used in a battery, a material with a high volume expansion has practical disadvantages, e.g. it can lead to degradation of the material upon cycling. Having said this, it should be noted that none of the axis show a larger change than 5% per sodiation step, neglecting the (b)-axis in the first sodiation step. Thus, although the crystal structure of NDTo shows significant volume increase upon sodiation, the expansion happens rather smoothly and slowly.

4.3.2. Van der Waals corrections

Similar to the corrected calculations for NDMe, a completely new series of calculations with different correction models were executed on the empty host structure of NDTo. A complete overview of the results is provided in table D.2 in appendix D. A number of observations can be made from the result of the calculations with different correction models. First of all, the calculations with correction models IVDW=12, IVDW=202 and IVDW=4 do not result in insignificant differences between the calculations without any correction model. As can be seen in the overview, the total unit cell volume change with respect to the experimental data for these models is 12,15%, 12,14% and 12,13%, respectively. These models are thus discarded as candidates for accurate correction models for NDTo. The models IVDW=1 and IVDW=10 result in exactly equal outcomes with the total unit cell volume change being -3,74%. Like for NDMe, IVDW-11 proves to be the best correction model with a volume change of 1,75% and is therefore selected as best approximation and used in the new sequence of calculations of the sodiation pathway of NDTo. The incorrect calculation results in a volume mismatch with the experimentally obtained results of 12,15%. The difference between the mismatch of the corrected calculations and the uncorrected calculations show that the importance Van der Waals corrections for NDTo is very significant.

The sodiation pathway based on the corrected calculations is identical to the uncorrected sodiation pathway, and is thus explained by the DBSs and QBSs as described in section 4.3.1. Nonetheless, the lattice vector lengths and total unit cell volumes are without exception significantly smaller in the outcomes of the corrected calculations. Besides that, the relative unit cell volume change in sodium insertion steps 3 and 4 are different in the uncorrected and corrected calculation outcomes. This translates to a different pattern of the change in the vector lengths a, (b)an c. A complete overview of research outcomes is provided in table E.2 in appendix E. The implication of the discrepancies in the formation energy, voltage profile and volume change is shown in the next sections.

4.3.3. Formation energy

The Convex Hull diagram for both the corrected and uncorrected sodiation steps is showed in 4.16. There are several observations to be made. First of all, the two curves show a significant offset which has a maximum at a fraction of sodiation of 0.5. However, the shape of both curves are (proportionally) identical. This means that for both curves, it is clear that step 3 is not a stable state and will be 'passed by'. Secondly, the spread of relaxation energies of different configurations within the same sodiation step is significantly different between the corrected and uncorrected pathway. The Van der Waals corrected pathway shows a spread numerous times larger in the first, second and fourth step. In step 3 the spreads of both pathways are comparable.

But the most important observation is the fact that the Van der Waals corrected calculations result in a enthalpy of formation convex hull diagram which is positioned lower than that of the uncorrected calculations. This is in complete contrast with the observation made in the enthalpy of formation convex hull of NDMe. This result implies a difference in significance of the Van der Waals correction between the NDMe and NDTo molecules.

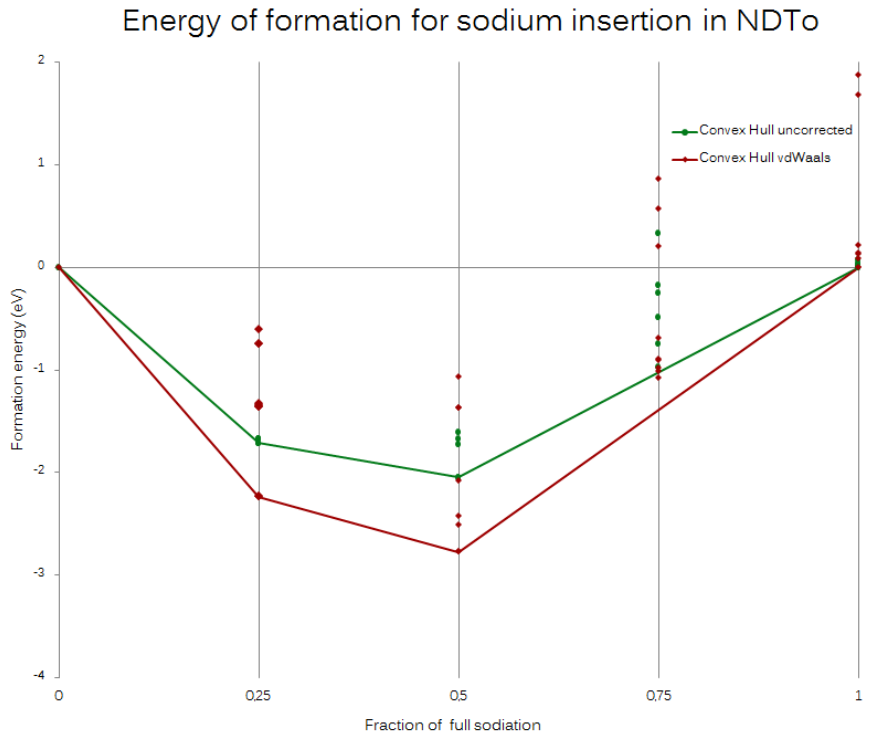

Figure 4.16: Convex Hull diagram of both the basic and the van der Waals corrected sodiation pathways of NDTo

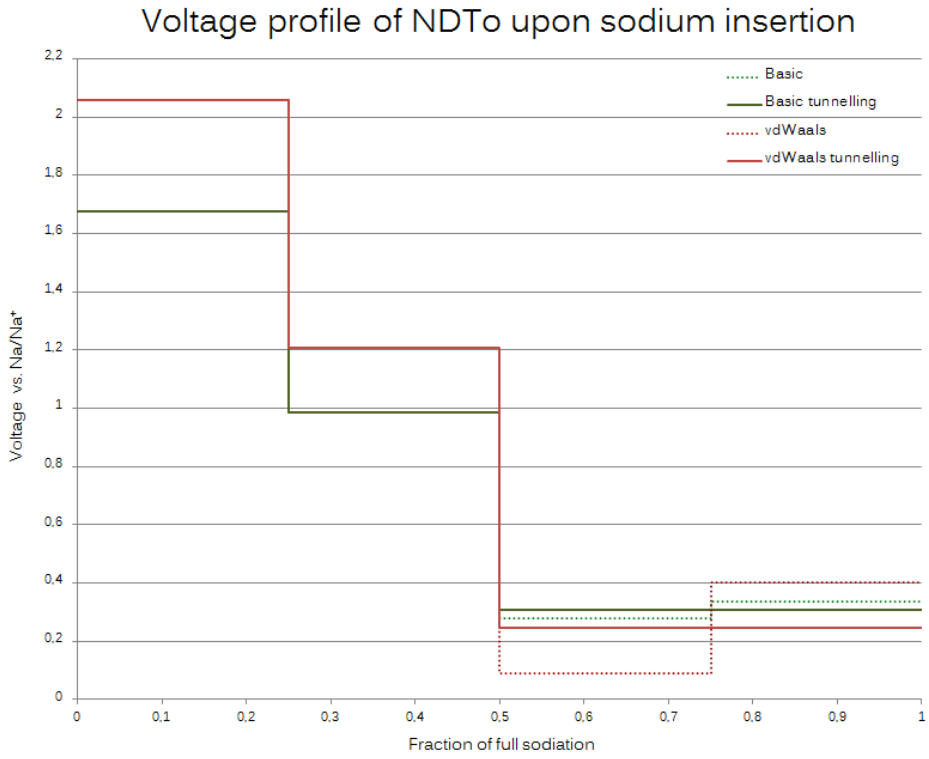

Figure 4.17: Voltage profiles of both the basic and the van der Waals corrected sodiation pathways of NDTo, in Volts vs. Na/Na^+

4.3.4. Voltage profile

Knowing the stable states in the sodiation pathways, as presented in the convex hull diagram, the voltage profile for NDTo is calculated and showed in figure 4.17 in section 3.3.2. The voltage profiles for the corrected and uncorrected have a similar shape, as could be predicted from convex hull diagram where step 3 is 'passed by' by the tunneling effect. Three voltage levels indicate a sloping voltage profile for an increasing fraction of sodiation.

There are two main differences between the uncorrected and corrected pathways. The first is the significant difference in the voltage between a sodiation fraction of 0-0.5. Between a sodiation fraction of 0-0.25, the Van der Waals corrected pathway shows a voltage of 2,06V versus Na/Na^+, while the uncorrected shows a voltage of 1,68V. For the sodiation fraction between 0,25-0.5, the Van der Waals corrected pathway shows a voltage of 1.21V versus Na/Na^+, and the uncorrected pathway 0.99V. The second difference is visible in the sodiation fraction range of 0.5-1. The Van der Waals corrected pathway shows a slightly lower voltage than the uncorrected pathway. This is in contrast with the tendency in the first part of the sodiation fraction range. Tunneling from the second to the fourth sodiation step makes a significant contribution in the Van der Waals corrected pathway. The dotted lines reflect the situation without tunneling, and the continuous lines reflect the voltage profiles with tunneling taken into account.

4.3.5. Volume change

The relative change in unit cell vector lengths (a), (b) and (c) are depicted in the figure 4.18. As can be noted, the volume change of step 3 is omitted, as tunneling will occur between the second and the last sodiation step. On first sight, there is no substantial difference between the uncorrected and corrected pathway lattice change. However, still a few observations can be made looking at the triangular shapes and the overview of the data in table E.2 in appendix E.

The lattice vector length (c) does hardly change, with a relative volume change of all steps in the range of -0.81% and 1,32% for the uncorrected pathway and -0.97% and -0.64% for the corrected pathway. The lattice vector lengths (a) and (b) change more significantly. For the uncorrected pathway, the (a) vector length changes in the range of 1,88-8,21% per step, where the (b)vector length changes in the range between -7,65% and 6.00%. There is a tendency for the Van der Waals corrected pathway to show a smaller range in the vector length change per step. This can be described as a 'damping' effect. Noticeably, for the corrected pathway the vector (a) lengths change in a range of 2,48-4,80% and the (b) vector lengths change in a range between -5,67% and 6,28% per sodiation step. The differences in the change of vector lengths between the two calculation methods are plotted in figure F.2b in appendix F. The largest difference in the vector change between the uncorrected and corrected pathway is the change in vector length (a) after the fourth sodiation step. The uncorrected pathway shows an increase of 8.21% and the corrected pathway an increase of 4,80%.

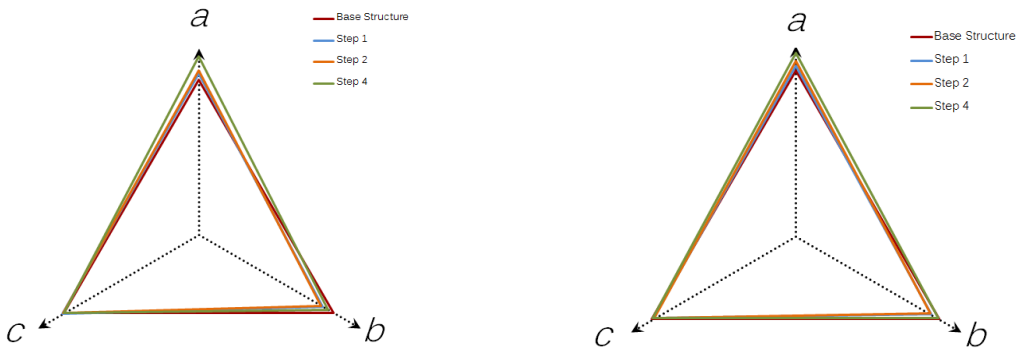

(a) without correction model

(b) with correction model

Figure 4.18: Relative volume change of the NDTo unit cell upon sodiation before Van der Waals correction, represented in the change in lattice parameters (a), (b) and (c).

5

Interpretation and discussion

In this chapter the interpretation of the results will be combined with a discussion based on insights of other studies in literature. Also, a critical reflection on the data as obtained will be made in order to evaluate the research outcomes and place it in a wider scientific context.

5.1. Interpretation of results

5.1.1. K-point settings

The search for appropriate K-point settings did not go as smoothly as previous studies make belief [25, 58]. An important difference with other studies is the lattice structure of the materials. Many metal oxides (like TiO_2) have lattice configurations which is easy to translate into appropriate K-point settings. A cubical lattice for example, would have K-point settings of (1-1-1) or a multitude of it. For both the NDMe and NDTo, finding appropriate K-point settings for the empty host structure was not the hardest part. Choosing a range of K-points that were approximately inversely proportional to the lattice vector lengths (a), (b) and (c) resulted in outcomes for 6 out of 11 settings for NDMe and 9 out of 14 settings for NDTo. The other settings resulted in significant k-point mismatch, which means that VASP was unable to perform DFT calculations.

Initially, the lowest acceptable K-point settings were selected with the relaxation energy convergence versus the CPU time as main criteria. In the calculations for the sodiation pathway of NDTo, the suitable K-point settings were found to be (4-7-2) for the empty host cell. However, in the second sodiation step, these K-point settings were not valid anymore. A new trial and error set resulted in the new start with the K-points of (6-11-2). These K-points became invalid in the fourth sodiation step. Finally, all calculations had to be redone with K-points settings of (6-12-2). The main reason for the K-point settings to become invalid in a later stage of the sodiation process is most probably the significant lattice distortion. The results presented in the tables E.1 and E.2 in appendix **??** show lattice distortion in all vector lengths. As the K-points are inversely proportional to the vector lengths of the crystal lattice, it is understandable that at some point the K-point settings are not valid anymore.

As the calculations of the sodium pathway of NDMe were performed later than the calculations for NDTo, similar K-point settings (12 6 2) were used directly in order to prevent recurring K-point settings invalidity. Smaller K-points (8-3-2) would have been chosen if the predetermined requirement as defined in section 3.2.1 would have been the only determining factor. Choosing a higher K-point setting appeared feasible, as all sodiation steps with K-points (12-6-2) yielded results. An additional advantage of choosing similar K-point settings for NDMe and NDTo is the ability to compare results with a higher reliability.

As lattice distortion has been recorded in all sodiation steps in both the Van der Waals corrected as the uncorrected calculations, it is open for discussion whether a fixed K-point settings remain as valid throughout

the full sodiation process as in the beginning. Valid and appropriate K-point settings are necessary to arrive at trustworthy results. Changing lattice parameters with the same K-point settings is most likely to result in a larger error in research outcomes. To prove the expected growing deviation, experimental data about the lattice dimensions for step-wise sodiation process for NDMe and NDTo is needed. At the moment, no such data is available as far as the author is concerned.

On the other hand, it could be argued that any valid K-point setting that has been been selected based on the convergence energy requirement will result in reliable data. In other words, the chosen K-point settings were already larger than needed, leading to more detailed results and higher CPU times. Lattice distortion would sooner lead to invalidity of K-points -meaning no results at all- than an increasing deviation from (non-existing) experimental data. In addition, as the (relative) relation between the results is more important than the absolute values, a structural offset can be argued to be of minor worry than expected.

5.2. Importance of Van der Waals correction

The Van der Waals force tends to increase for larger molecules with high surface areas. The importance for the Van der Waals correction was thus anticipated to be bigger for the NDTo than for the NDMe molecule. The NDTo molecule is significantly longer and shows a bigger surface area than the NDMe, as the tolyl side-group is both wider and longer than the methyl side-group.

There are several ways to analyze the significance of the Van der Waals corrections. Generally, the most important parameter has been the value of the relaxation energy of the crystal structure upon sodiation. Other important parameters are the lattice dimensions such as the unit cell volume, the vector lengths and the unit cell angles. Because experimental data of lattice dimensions for NDMe and NDTo were obtained by Krishna et al. [26], these has been the main criteria in the determination and selection of the best Van der Waals correction model. Without exception, all vector lengths and total unit cell volume are smaller in the calculation that are corrected by the zero damping DFT-D3 method of Grimme [12], which turned out to be most accurate compared to the experimental data. Apparently, the Van der Waals forces have a net attracting effect, causing the molecules to be closer to each other in all directions. This leads without exception to lower relaxation energies. To understand the trends in the lattice distortion, the outcomes of the change in lattice parameters will be discussed for the NDMe and NDTo separately in the following sections.

5.2.1. Sodium insertion in NDMe

The volume mismatch between experimentally measured data and calculated results without Van der Waals corrections is 9,73%, where that of results with the zero damping DFT-D3 method of Grimme [12] for the Van der Waals interactions is -0,42%, as presented in section 4.2.2. It is therefore safe to conclude the Van der Waals corrections to be of very significant importance to arrive at accurate calculation results for the empty host structure of NDMe. However, to draw conclusions for the significance of the corrections in the calculations for NDMe upon sodium insertion, we need to compare the outcomes of the uncorrected and corrected calculations carefully.

In the case of NDMe, the correction model resulted in an structural decrease of relaxation energy in all sodium insertion steps. The difference between the uncorrected and corrected calculations increases at higher fraction of sodiation, so an obvious conclusion would be that the Van der Waals correction becomes more relevant in systems with an increasing number of atoms. Implicitly this would mean that the uncorrected calculations have an increasing deviation from the true values as the number of atoms increase.

There is one logical argument that proves this conclusion to be a deductive fallacy, namely that the correction model itself could become increasingly inaccurate at an increased number of atoms in the system. This means that the observed relative decrease between the relaxation energies of the uncorrected versus corrected calculation could imply three underlying scenarios: (1) only the uncorrected, (2) only corrected or (3) both calculation models deviate more from the actual (true) values at higher fraction of sodiation. The experimental data for the partial sodiated crystal structures of NDMe could provide crucial insights in matter, but

these are not available at the moment[1]. This implies that no conclusions can be made about the change of significance of Van der Waals corrections upon sodium insertion from the difference in relaxation energies.

Another uncertainty in conclusion about increasing significance is brought forward by the change in absolute lattice parameters between the uncorrected and corrected calculations for NDMe. The difference in total volume change and upon closer examination all three vector lengths show no apparent evidence to support the claim of an increasing importance of the Van der Waals correction upon sodium insertion. Put differently, the difference in the change of vector lengths (a), (b) and (c) are not structurally decreasing or increasing, but show a rather fluctuating behaviour upon sodium insertion. Note that the above statement is about the difference of the change in absolute values of the vector lengths, not about the absolute values themselves. When more gravity is put in the importance of lattice distortion, there is no apparent evidence to conclude the significance of the Van der Waals force to increase upon sodium insertion.

5.2.2. Sodium insertion in NDTo

Following the same line of argumentation as in the previous section on the significance of the the Van der Waals corrections in the sodiation pathway for NDMe, the results for NDTo are analyzed to find trends. As anticipated, it is thus no surprise to see the difference in absolute values of relaxation energies obtained in the uncorrected and corrected calculations to be larger (-6.00 to -6.95 eV) than those of NDMe (-3.78 to 5.15 eV), because NDTo has a higher surface area and is thus more prone to Van der Waals forces. Similar to NDMe, the difference in absolute relaxation energies increases and becomes more negative for NDTo at an increased fraction of sodiation.

In addition, a slight trend in the differences of total unit cell volume between the uncorrected and corrected calculations upon sodiation is observed and tends to become more negative upon sodium insertion. This is caused by the vector length (a), which is increasing less rapidly in the corrected calculations than in the uncorrected calculations. This principle can be seen as a certain 'damping' effect of Van der Waals corrections. This is in line with the understanding of the inter-atomic and inter-molecular dispersion force as described in section 2.5.1. However, the damping effect of the Van der Waals correction is hardly evident in the vector lengths (b) and (c), as the difference between the change in vector lengths between the uncorrected and the corrected calculations first increase and than decrease upon sodiation. Therefore, an overall damping effect on the lattice stability by the Van der Waals correction can not be sufficiently supported by the results. But the damping effect in lattice vector (a) and the observed slight increase in total unit volume difference are found to be sufficient enough to claim the significance of Van der Waals force corrections to increase upon sodiation.

Concluding, the significance of the Van der Waals force is initially very large and is found to become more significant upon sodiation of NDTo. This means that the uncorrected calculations in general have a structural off-set in all lattice parameters which tends to increase.

5.3. Formation enthalpy and voltage profile

The enthalpy of formation convex hull diagrams for NDMe and NDTo show a number of interesting differences. Firstly, for NDMe the enthalpy of formation convex hull diagram of the Van der Waals corrected sodiation pathway is structurally and significantly higher than the diagram of the uncorrected sodiation pathway. This implies that the uncorrected calculations overestimates the thermodynamic favorability of the partially sodiated phases of NDMe. This is in contrast to the outcomes for NDTo, where the convex hull diagram for the Van der Waals corrected sodiation pathway is positioned below the convex hull diagram of the uncorrected sodiation pathway. This implies that for NDTo, the uncorrected calculation outcomes underestimate the thermodynamic favorability.

Secondly, the spread of the enthalpy of formation outcomes for the different configurations per sodiation step is of comparable size in NDMe, in both uncorrected as corrected calculation outcomes. For NDTo the

[1] As far as the author is concerned

spread of the uncorrected calculations for different configuration per sodiation step is clearly smaller for step 1, step 2 and step 4. Step 3 shows a spreads of similar sizes between the enthalpy of formation of different configurations. It is debatable whether the outcomes of step 3 play a significant role, as this phase is most probably 'skipped' due to tunneling. The spread of the different configurations in the enthalpy of formation convex hull diagram is a measure for the thermodynamic favorability of binding sodium at 'any' assumed logical binding spot. The bigger the spread, the more specific the molecular structure binds the sodium atom a specific binding spot. In a way, it can be described as the 'selectivity' of a specific binding spot. In this light, the calculations performed with a Van der Waals correction show a higher selectivity in the sodiation pathway of NDTo than the uncorrected calculations do. This conclusion can not be made for NDMe, where the spread is of similar size.

Another observation is made by analyzing the data behind the enthalpy of formation convex hull diagram. As stated earlier, the difference in relaxation energy outcomes between the corrected and uncorrected calculations tends to become bigger at higher fraction of sodiation. It is therefore no surprise that the difference between the relaxation energy of the full structure and the empty host structure is bigger when the Van der Waals correction is used. This means that for the two enthalpy of formation convex hull curves to overlap exactly, the relaxation energies outcomes of the corrected calculations have to be structurally lower by the the total difference of the full cell and the empty cell divided by the number of steps. In other words, the convex hull diagram will only stay the same if the relaxation energies of the intermediate phases change with exactly the same proportionate amount as the size of the difference in the spread of relaxation energies. For NDMe, this is not the case for the first intermediate phases in step 1 and step 2, as the change in relaxation energies is not sufficiently large. This results in a convex hull diagram for the corrected calculations to lie above that of the uncorrected calculations. For NDTo this is also not the case, as the change in relaxation energies for step 1 and step 2 is in fact larger than the proportionate amount. This results in the convex hull diagram of the corrected calculations to lie lower than that of the uncorrected calculations. Concluding, the emphasis of the influence of the Van der Waals corrections on the favorability of the the sodiation pathway for NDMe lies in the last steps, and for NDTo lies in the first steps.

The effect of this underlying difference between the influence of the Van der Waals correction on the NDMe and NDTo sodiation pathway is also visible in the voltage profiles. The voltage profiles of the corrected and uncorrected calculations of NDMe are almost similar up to a sodiation fraction of 0.5. After that, the voltage profile of the Van der Waals corrected calculations show a significantly higher 'tail' between a sodiation fraction of 0.5 and 1. In the voltage profiles of NDTo, exactly the opposite observation is made. The voltages of the corrected calculations in the sodiation fraction range 0-0.5 show a significant increase compared to the uncorrected calculations. In the higher range, the voltages are comparable, and even slightly lower for the corrected calculations.

Zooming out, for the two organic crystals NDMe and NDTo to serve as anode material in aqueous sodium-ion batteries, the voltage of sodium insertion has to lie in the proximity of the stability window of water, as indicated by the Pourbaix diagram shown in section 6.1. At neutral pH, the boundary of the stability window on the anodic side, also called the hydrogen evolution line, is at roughly 2,3 V versus Na/Na_+. The voltage curves of NDMe do not show good prospect in reaching anywhere near this value, as both corrected and uncorrected calculations reach just under 1.8V versus Na/Na_+. NDTo, in contrast, shows a promising voltage with Van der Waals corrected calculations, in the sodiation fraction range of 0-0.25. However, the voltage profile provides enough suggestion of a steeply descending voltage slope, stabilizing at roughly 0.3 V versus Na/Na_+ until fully sodiated. When applied in an aqueous battery, the material can thus not be allowed to be utilized up to its full capacity, which is unfortunate and has adverse implications for the specific energy and energy density.

5.4. Wider scientific scope

The newly gathered insights can be placed in a wider scientific context to estimate its significance and to compare it with other insights. Firstly, a comparison with experimental data is made, focusing on the same or similar compounds as researched here. Secondly, the suitability of DFT for organic crystals is evaluated in order to gain more understanding of the accuracy and the applicability of DFT calculations for complex molecular structures.

5.4.1. Comparison with experimental data

Within our research group, former Master's student Bas Buise has performed experimental research on crystalline NDMe as promising anode material in aqueous sodium ion batteries and presented the data in his master's thesis.[5] The most interesting results are represented in the graph on page 9 of the report. In this graph, reproduced in figure G.1 in appendix G, the voltage profile during the first 75 charge/discharge cycles are shown. The dark blue line in represents the first charge/discharge cycle. This line shows a clear voltage plateau around 2.3V and a second plateau near 1.8V versus sodium metal between a sodiation fraction of 0-0.3 and 0.3-1.2, respectively. After that, the voltage decreases and seems to fall back in another voltage plateau. The second voltage plateau shows a remarkable similarity to the computationally produced voltage profile. To compare, the voltage profiles of NDMe are repeated in appendix G.

However, based on the computationally produced voltage profile, one would expect the the second voltage plateau to end at a sodiation fraction (as determined by Buise in this case) of 2, and not at 1.2 as experimentally observed. Buise describes the observation of capacity loss due to the dissolution of active material into the electrolyte and an unwanted side-reaction. This could be a valid explanation for the voltage plateau to prematurely collapse. The second voltage plateau found in the computational results is located at roughly 0.4 V versus sodium. The shape of the experimental voltage profiles do hint for another voltage plateau at this voltage, but even in the first cycle the curve shows a steeps slope and a premature collapse. Considering the reported capacity loss and expected presence of side reactions, the computational results seem to match to a great extent with the experimental results for NDMe.

Having performed computational calculations to gain insights in the sodiation behavior of two variants of naphthalene diimides, it is useful to compare the results with other research outcomes on variant of naphthalene diimides.

Naphthalene diimides have been used as backbone molecule to be tuned with different chemical side-groups in order to unveil the difference in redox capabilities. Vadehra et al.[47] reported seven different variants of naphthalene diimides using H, HMe2, F, CN and hexyl as side-groups. The study reports first reduction potentials in a range of 2.9-2.3 V versus Li/Li^+. As the study researched the lithiation, the outcomes should be converted to potentials versus sodium metal-redox, which is not always a straightforward conversion in practice, as the intercalation process could be different for sodium atoms. When assuming a practical voltage difference to convert the to sodium potentials of 0.5 V, the variant with the best performance (N-hexylnitrile-substituted NDI) showed to potential of 2.3 V versus Na/Na^+. This makes the compound extremely interesting for the application as anode material in an aqeous sodium-ion battery, as the hydrogen evolution line is at 2.3 V vs Na/Na^+ at neutral pH.

Others have compared the electrochemical performance of the several organic backbone structures like 1,4,5,8-naphthalenetetracarboxylic dianhydride (NTCDA, NDI in this thesis), pyromellitic dianhydride (PMDA) and pyrilene 3,4,9,10-tetracarboxylic dianhydride (PTCDA) comined with an alkyl chain to construct polyimdes. [6, 9, 10, 43, 52, 61] The variants with the larger backbone structure of PTCDA yielded better results than variants with NDI, showing a lower solubility, higher working potentials and higher cycling stability. [61] A polyimde with interchanging NDI and ethane groups was found to have a discharge sloping voltage plateau between 2.25-1.8 V versus Na/Na^+ and a sodiation capacity of 4 ions per NDI molecule. [6] Another study reports the same compound have a discharging potential range between 1.89 - 2.29 V versus Na/Na^+, suggesting excellent applicability as anode in aqueous sodium-ion batteries. [9] A polyimide with only NDI and no intermediate was tested by Qin et al. [43], reporting redox peaks at 2.22/2.07V and 2.47/2.27V versus Na/Na^+, exactly above the hydrogen evolution potential.

One of the most valuable studies in this theme was done by Song et al. [52] and involved five different polyimide samples of which three were with the NDI backbone. Here, the difference in theoretical and experimental data is explained by the molecular structure of the polymers, only two-electron transfer is involved, resulting in only half of the theoretical capacity to be obtained. Four-electron transfer could be obtained by deep discharging below 1.5V versus Na/Na^+, but will inevitably cause serious structural damage like the collapse of the polymer framework.[52] Because a polyimide with NDI and a tolyl side-group is analyzes in this study, it is valuable to compare the results. The tolyl-variant polyimde shows redox peaks at 1.9-2.2 and 2.15-2.3 V versus Na/Na^+ (converted from Li/Li^+ with conversion of 0.35V). The reported average discharge voltage was 2.00 V versus Na/Na^+. Lastly, discharge/charge potentials for NDI crystal without additional side-groups were reported to be 2.7/2.4V versus Na/Na^+, in an aqueous environment. [22]

The mentioned references to previously reported experimental research are useful to a certain extent. As many researches have been focused on polyimide, most probably motivated by the relatively easy sythesis routes, the outcomes can not be compared with the computational results presented in this thesis. They set the stage and suggest a range of outcomes to be expected. The general trend to be seen is that NDI variants with larger side groups tend to result in lower discharge/charge voltages. These general trends do not match well with the trends described from the computational work, as NDTo shows a higher voltage (for low fraction of sodiation) than NDMe.

5.4.2. Suitability of DFT for organic crystals

The unit cell dimensions of NDMe and NDTo are compared to most previously reported DFT results rather large. Most metal oxides require smaller and less complex unit cells, which results in faster DFT calculations and allows for different kinds of calculations besides DFT, such as Molecular dynamics. It has occurred more than once to await a single DFT calculation for one configuration for one sodiation step for more than 2 weeks. Having over a hundred of atoms per one unit cell in the case of NDMe and NDTo, it is relevant to re-valuate the (time) investment necessary for completing a set of DFT calculations.

Besides that, as it is harder to synthesize crystals compared to polyimdes for example, it would be interesting to make computational calculations for those structures. However, as polyimdes contain out of long repetitive strings whose configuration can influence the sodiation behavior and can thus not be simply repeated as if it is bulk material, the validity of such a research setup is under scrutiny.

One recent study focused on the historic development of functionals in DFT calculations which have been designed to minimize the exact density of electron distribution, concluded the DFT functionals to have become less accurate after the year 2000. The theorems at the core of DFT state that energy of a many-electron system in its ground state is fully defined by the electron density distribution. The calculation methods for the energy-minimizing electron density for atomic species have since 2000 become less accurate, sacrificing physical rigor for the flexibility of empirical fitting.[34] This means that comparison with experimental data remains a crucial step for the validity of the DFT outcomes. Although DFT is extremely effective in screening a large number of substances without the need of (expensive) synthesis, it might not be best to use it for accurate predictions.

II

Second Part: Experimental work

6

Background theory on increasing the stability window

6.1. Aqueous electrolyte

Water-based electrolytes offer several substantial differences compared to electrolytes based on organic solvents. First of all, aqueous electrolytes are not flammable and thus provide much better safety. Next, aqueous electrolytes and the separators are less costly than organic electrolytes.[63] Also, aqueous salt solutions generally have a very high ionic conductivity which is unsurpassed by organic electrolytes, and are therefore promising for very high power operation. In some cases, the electrochemical performances of sodium-ion batteries have been improved with aqueous electrolytes compared to non-aqueous electrolytes.[35] This is mainly attributed to difference in the physical properties between water and organic electrolytes, as water has as a higher relative dielectric constant and lower viscosity.

However, aqueous electrolytes also bring several challenges. According to Kumar et al [45], the majority of aqueous rechargeable alkali-metal ion batteries are plagued with side reactions that limit their cycle stability. The four major side reactions are (1) hydrogen and oxygen gas evolution by electrolyte decomposition, (2) reaction between electrode materials and water or residual oxygen, (3) electrode dissolution and (4) proton co-insertion into the host electrode materials. Pure water will decompose into gaseous hydrogen and oxygen at potentials above 1.229V in a process called electrolysis. The distance between the potentials of the half-cell reactions for hydrogen and oxygen formation is called the stability window of water. The decomposition of water has to be prevented in aqueous batteries to enable safe operation and to prevent electrode and thus capacity degradation. This is the main reason why batteries with aqueous electrolytes in general do not have high voltages compared to batteries with organic electrolytes.

The selection of the suitable electrode materials is primarily dictated by the stability window of water. The stability window is dependent on the pH value of the electrolyte. For increasing pH values the relative location of the stability window descents. In accordance to the Nernst equation, as discussed in section 2.1.3, the stability window descents with 0.059 V per pH. However, the width of the stability window remains the same, namely 1.229V. This relation is illustrated in a Pourbaix diagram, as shown in figure 6.1.

There are kinetic considerations that could enlarge the actual potential at which water decomposes. Namely, in some electrolyte-electrode combinations the breakdown of electrolyte can result in the formation of an Solid-Electrolyte-Interphase (SEI), that effectively widens the stability window of the electrolyte.[51] This happens in lead-acid batteries, where a $PbSO_4$ film is formed at the electrode surface allowing the battery to operate at 2.0V, which is well beyond the thermodynamic stability window of pure water. Next to the electrode materials, the salt concentration of the aqueous electrolyte can be chosen in such a way, that water decomposition will be prevented to a certain extent. This leads to the 'practical' stability window which is dependent on the involved materials. In previous research from our group a practical stability window was

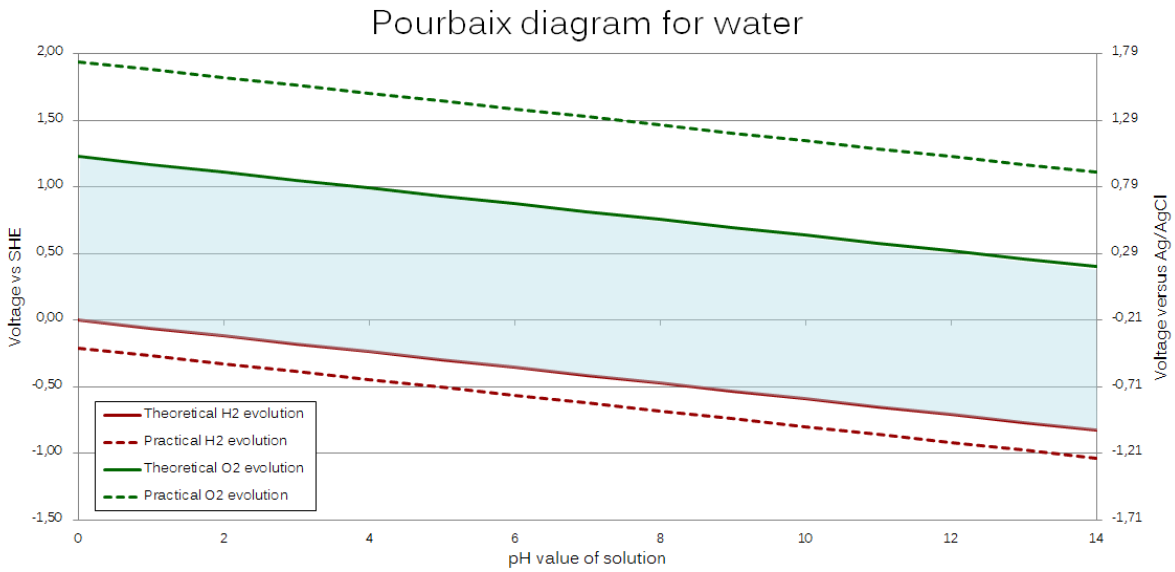

Figure 6.1: Pourbaix diagram of pure water including the theoretical and practical hydrogen and oxygen evolution lines and in blue the theoretical stability window.

determined based on an average of many electrode materials. [20] The practical evolution lines for hydrogen and oxygen are included in figure 6.1. The blue box is indicates the stability window of water.

6.2. Widening the stability window

Electrolyte concentration is an important factor that influences the electrochemical properties of the battery system. [13, 30, 36, 53, 71] It can improve the Coulombic efficiency, cycling stability of the electrode materials and bring down the activity of electrolyte solvents. Next to the electrolyte salt concentration, additives can protect the electrodes from reacting with dissolved oxygen gas by forming a protective layer on the electrode's surface. Among these additives are carboxymethyl cellulose (CMC) and agarose (Ag) and vinylene carbonate (VC).[45] In addition, Sodium Dodecyl Sultafate (SDS) as additive can behave as surfactant and has been reported to increase the stability window to 2.5V. [17]

Both lithium and sodium salts have been researched for their applicability in opening the window for aqueous electrolytes. Highly concentrated aqueous electrolytes of lithium bis(trifluoromethane sulfonyl)imide (LiTFSI)[53], lithium trifluoromethane sulfonate (LiOTf)[54], saturated $LiNO_3$[63] have previously been reported and show that water molecules do not engage in electrochemical decomposition when outnumbered by lithium ions. This is explained by the formation of a thick SEI and the reduction of water activity and electrode solubility.[36] The positive results in aqueous lithium-ion batteries have encouraged researchers to study the sodium equivalents of these salts. Very recent reports on high concentrations of sodium salts in aqueous electrolytes show similar feasibility. For example, Kühnel et al tested ultrahigh concentrations (up to 37m) of Sodium bis(fluorosulfonyl)imide (NaFSI), showing a stability window of 2.6V.[27] Suo et al tested 9.26m sodium trifluoromethane sulfonate (NaOTF) showing an overall electrochemcial stability window of 2.5V.[55] These high salt concentrations effectively mean the water molecules are outnumbered against the salt molecules. This insight has led to the term 'water-in-salt (WIS)' instead of 'salt-in-water' electrolytes.

Fluoride and sulfur containing salts impose high costs and safety concerns, making them unsuitable for low cost and safe batteries. Fluoride free sodium salts have also been reported for the application in electrolyte, among them Na_2SO_4, $NaNO_3$ and $NaClO_4$.[30, 35, 36, 40, 45**?**] Na_2SO_4 has a rather low saturation concentration of roughly 2M and is thus not able to outnumber the water molecules. $NaNO_3$ is known to have significant corrosive side reactions[35] with electrode materials, causing capacity fading. Li et al [30] point out that high concentration $NaClO_4$ electrolytes is an effective strategy to improve electrochemical performance of ferricyanide cathode for aqueous sodium-ion batteries. High concentrations of $NaClO_4$ are proven

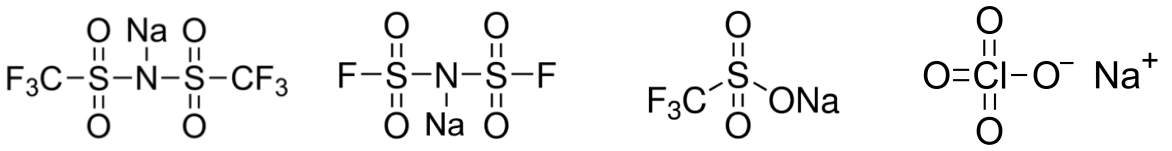

(a) NaTFSI [46] (b) NaFSI, 35m, 2.6V [27] (c) NaOTF, 9.26M, 2.5V [55] (d) $NaClO_4$, 17m, 2.8V [36]

Figure 6.2: Molecular structure of various sodium salts used previously to improve electrolyte stability.

to raise the working potential and improve the Coulombic efficiency. Having tested a range of concentrations between 1M and 9M, the 6M $NaClO_4$ aqueous electrolyte was considered to be optimal, as the Coulombic efficiency almost keeps invariable with further increase of concentration.[30] Another study experimented up to 4 M $NaClO_4$ and found the highest concentration to be feasible. [35]

An overview of the molecular structures of the previously reported sodium salts with concentrations and increased stability window is given in figure 6.2. Note that 'm' stands for molality, which is mol of solute per kg of pure solvent, and 'M' stands for molarity, which is mol of solute per liter of dissolved solution. From this overview, it can be concluded that an electrolyte with high concentrations of $NaClO_4$ is most promising, since it has the highest reported stability window and also does not contain fluoride atoms.

6.3. Electrode selection

In order to test NDMe as anode material in an enhanced electrolyte, other electrode materials that have been tested previously have to be tested in the test-cell first. This is because even though the reference electrode materials are well documented, they could show different behaviour in a different test-cell. In this way, the 'degrees of freedom' in the strategy are minimized leading to a robust scientifically justifiable research pathway.

Among the selection criteria for the reference electrode materials is: evidence of high synthesis yield, capacity retention upon cycling, redox potentials within the stability window of either water or 'enhanced' water, affordability and complexity of the synthesis route. The combination $NaTi_2(PO_4)_3/Na_{0.44}MnO_2$ in an aqueous system was found to match with these criteria, and was previously researched by Li et al [32] and Wu et al [66]. A remarkable observation is the use of $Na_{0.44}MnO_2$ in the aqueous sodium-ion battery system by the commercial company Aquion Energy Ltd., indicating the commercially viability of the material. [56, 65]

An additional advantage of choosing $Na_{0.44}MnO_2$ as reference cathode material is collaboration with other members from our research group, who currently research $Na_{0.44}MnO_2$ for different research objectives. Experiences and best practices are therefore very relevant to share.

Xu et al [69] and Li et al [31] reported insights in the sodiation process of $Na_{0.44}MnO_2$ and $NaTi_2(PO_4)_3$, respectively. The $Na_{0.44}MnO_2$ reveals two separate phases, and the $NaTi_2(PO_4)_3$ has a NASICON structure, as showed in figure 6.3.

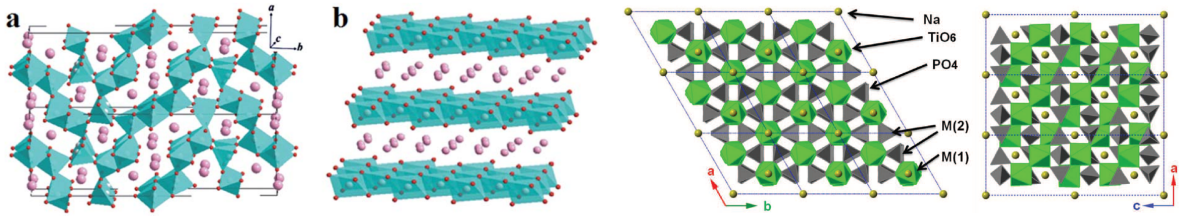

(a) Na_xMnO_2 configurations.[69] (b) NTP NASICON at different orientations.[31]

Figure 6.3: Schematic illustrations of $NaTi_2(PO_4)_3$ and $Na_{0.44}MnO_2$.

7

Research Methods

7.1. Test cell and materials

Because sodium metal can not be used as anode material in combination with an aqueous electrolyte, a reference electrode is required in order to measure the relative potentials of the reactions. This complicates the testing procedure, because most reference electrodes are too large to fit in the usual test-cell for half-cell or full-cell tests. Therefore, a different test-cell casing has to be used. During previous experimental work within our research group, appropriate test-cell casings have been constructed. At the moment, the available test-cell casings can not be sealed, which disables the possibility for removal of dissolved oxygen from the water. Sealed test-cell casings are constructed during the writing of this thesis and offer more flexibility for future research.

7.1.1. Test cell design

The open test-cell configuration is custom made and has reservoirs suitable for reference electrode insertion, and spaces in between for the placement of electrode materials and separator. In vertical positioning, electrolyte can be inserted after assembly of the test-cell. The design of the open test-cell can be seen in figure 7.1. With the inserted reference electrode and placed separators and electrodes, the volume to be filled by the electrolyte is approximately 6 mL.

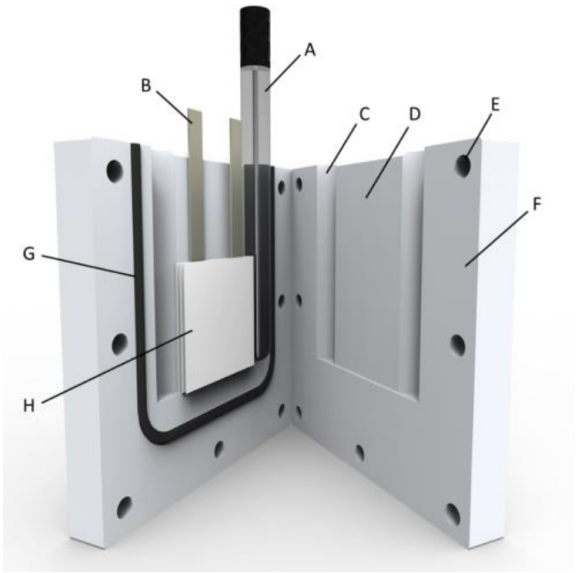

Figure 7.1: Test-cell design with the AgCl-reference electrode (A), the electrodes (B), 12 mm reservoirs for reference electrodes (C), spacing for separators and electrodes (D), bolts holes (E), the cell casing (F), the rubber water-tight band (G) and separators (H).[20]

7.1.2. Non-active electrode material

Non-reactive and non-active electrode materials are required for a reliable measurement of the stability window of water. The material should have an intrinsic high electronic conductivity and should not decompose within the potential range used during the CV measurements. In previous studies, a number of different materials have been used for this purpose.

Stainless steel (316) is one of those materials, that can be produced in very thin layers in a woven mesh configuration. These layers can be made relatively cheaply, and can be cut easily in all different shapes. The material is generally very non-reactive in aqueous environments and has a high conductivity. Several scholars have used stainless steel in experiments related to increasing the stability window of water. [27, 33, 42, 53–55]

Another option is to use carbon cloth, which is also produced in a woven layer. As it is a convention to mix active electrode material with carbon black or activate carbon powder, is is an intuitive choice to test the stability window with non-reactive carbon cloth. An extra advantage is the possibility to coat the carbon cloth with active material in the half cell and full cell tests. In this way, the current collector material for the electrolyte measurements and the half-cell measurements is kept constant, increasing the reliability of the measurements. Previous scholars that tested for increase stability windows have indicated this as a significant benefit. [44, 45, 67]

A third option is to use titanium mesh. Titanium is known for its higher oxygen evolution over-potential, which is normally essential for avoiding the interference of oxygen evolution with the cathodic Na-insertion reaction. Titanium has been used in a number or studies as well. [17, 30, 36, 67, 68] Especially the work of Nakamoto et al [36] is of great value, since the combination with sodium percholorate and titanium mesh was proven to be without unexpected side reactions. Other options for non-reactive electrode materials are pure Zinc [35, 40], Nickel foam [2, 72], Aluminum foil [29] and platinum [16, 63, 66].

The strategy applied in this research will be to try the cheapest materials first, which are stainless steel (316) and carbon cloth. At the moment side reactions are observed and there are reasons to belief a different material is needed, the third electrode material of choice is titanium. This cost minimizing strategy is based on the belief that the several non-reactive electrode materials all enable highly detailed measurements.

7.1.3. Reference electrode

A reference electrode is needed in order to measure the relative potential of electrode materials in aqueous electrolytes, in contrast to testing in non-aqueous cells where sodium metal can be used. A number of reference electrodes are available for aqueous systems. In the line of previous research within our group [5, 20], a double junction silver chloride electrode (AgCl) from Sigma Aldich©. will be used in this research. The redox potential of this reference electrode (in standard 3.0M KCl) is 0.210V versus SHE The reference electrode can be tested for accuracy by measuring the potential of Copper foil in a 1.0M $CuSO_4$ aqueous solution. The measured potential should be 0.127V vs Ag/AgCl, under standard conditions.

The strategy to achieve accurate measurements is simple. Before every measurement series, the reference electrode needs to be checked for accuracy using the Copper-test. Before insertion in the test-cell, it should be cleaned and dried using distilled water. Furthermore, the tip should always be kept wet and the refilling hole on top should be open during testing. After testing, a wet protection sealing is put over the tip and the refilling hole is closed and stored in a shock-proof casing.

7.2. Synthesis of active electrode materials

Several scholars have reported synthesis routes for the selected electrode materials. This enables sensible comparison and verification of the test results with previously reported results. In this way it can be ascertained that (1) our synthesis outcomes are of comparable quality, (2) the test procedure including the three-electrode open air aqueous test-cell yields comparable results and (3) scientific justified conclusions can be drawn on the prospect of NDMe as anode material.

For the synthesis of $Na_{0.44}MnO_2$, the work of Wu et al [66] and Whitacre et al [64] is used. For $NaTi_2(PO_4)_3$, two different synthesis routes were found and both showed interesting features. Nakamoto et al [36] used a mixture of Na_2CO_3 (99.7%, Kishida Chemical Co., Ltd.), TiO_2 (99%, Sigma-Aldrich), and $NH_4H_2PO_4$ as precursors. Wu et al [67] used $CH_3COONa{\cdot}3H_2O$, $NH_4H_2PO_4$ and $C_4H_{10}OTi$ (titanium(IV) butoxide) as precursors. Although both routes have been reported successful synthesis with high yields, differences in precursors, the need for inert environments and prolonged exposure to high temperature can lead to differences in obtained

product. Therefore, both routes are were tried simultaneously. N,N' –bis(methyl)- 1,4,5,8-naphthalene diimide (NDMe) was previously been synthesized by members of our research group, following the synthesis routes as proposed by Deng et al [8]. The synthesis of the electrode materials has been done in collaboration with several members of our research group.[1]

In the scope of this work, the determination of the electrode capacity and capacity retention upon cycling is not of primary interest. To achieve the research objectives, it is of essential importance to redox potentials of used electrode materials. This means that accurate methods for determining mass loading, surface area and thickness are not needed. This eases the experimental process significantly. Based on this insight, the synthesized active electrode material will be mixed with activated carbon and binder Polyvinyldifluoride (PVDF) in a 80:10:10 composition to obtain a slurry. Without further measurements, this slurry coated on a stainless-steel strip, that is precisely cut beforehand for it to fit in the aqueous three electrode test-cell used in this study.

7.3. Cyclic Voltammetry measurement

To evaluate the electrochemical behavior of both the electrolyte and the electrodes, cyclic voltammetry (CV) measurements are widely used. There are different types of CV scans; the most common are the potentiostatic and galvanostatic test. In the potentiostatic test, the potential is accurately modified while measuring the current through the test sample. In the galvanostatic test the current is controlled while the potential is being measured. The potentiostatic test is most commonly used, as it provides insight in the specific electrochemical reactions that take place in an electrode material. CV scanners from Methrohm Autolab©with related software Autolab NOVA©are used. There is a high flexibility in the settings for a CV-scan, as the speed, accuracy, minimal and maximum voltages and cutoff currents can all be determined separately. The measured potentials at which reactions take place can vary with the scan rate.[63] Also, an appropriate voltage window needs to be set to prevent detrimental decomposition or side-reactions.

Standard test procedures are available, but are not applicable for testing in an open three-electrode system. The surface area, mass loading, type and purity of the test sample are all factors that can influence the suitability of a specific CV test procedure. Therefore, based on the dimensions of the test-cell and the materials involved, a suitable procedure for CV tests needs to be found. This is done by firstly exploring best practices in similar studies, followed by a systematical modification of test-parameters. Documenting the exact settings is of vital importance. A strategy for numbering based on the NATO phonetic alphabet will be applied, including naming experiment series 'Alpha', 'Bravo', 'Charlie', and so on.

During the search for a suitable CV test procedure, it is useful to set a number of boundary conditions. First of all, all tests will be performed with pH neutral electrolyte. For fixed pH values, the theoretical window of water is known, and any observed reactions within this stability windows are considered to be side-reactions. Furthermore, only a prolonged (more than 5 seconds) increase in measured current is considered as the indication of a reaction. Also, repeating a test must yield the same result for it to be reliable.

7.4. X-Ray Diffraction

X-ray Diffraction (XRD) is one of the most common measures to determine the diversity, purity and structures of molecules in crystals. The spacing of the layers of atoms in solid crystals is usually between 2-20 Å. [3] The wavelengths of X-rays are also in this range. Therefore, the crystalline sample can serve as an effective diffraction grating for a beam of X-rays. The pattern of diffracted X-rays can reveal the composition very accurately and quickly. By comparing the outcomes with the available data in an online materials database, the outcomes can be analyzed effectively. Also in battery research XRD is a powerful tool to verify a successful synthesis of electrode material. In figure 7.2 a representation of the X-ray diffraction setup is given. A monochromatic X-ray beam is passed through a crystalline sample. The diffracted X rays result in a interference pattern. By rotating the either the sample or the X-ray beam, and by changing the incident angles, give a range of patterns.

[1] Remco van der Jagt, PhD student & Alexander Selz, Master student

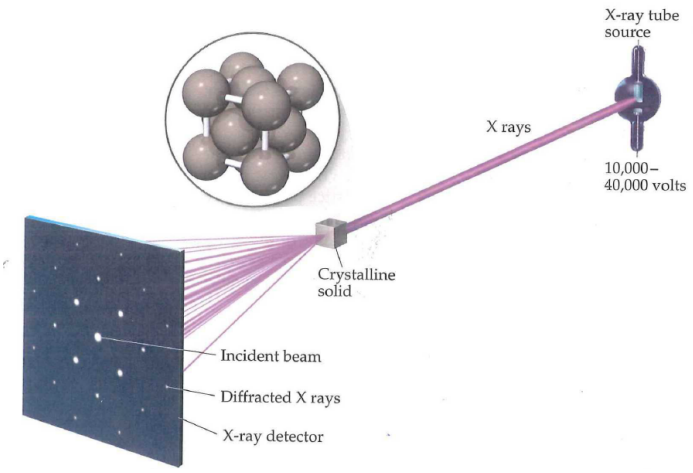

Figure 7.2: Representation of the X-Ray Diffraction (XRD) setup. Illustration copied from reference book [3].

The X-ray diffraction pattern of a pure substance is comparable to an unique fingerprint. The combination and intensity of diffraction angle peaks are easily distinguished. The fundamental principle is best explained by Bragg's law, that describes the destructive and constructive interference of diffracted waves.

$$n\lambda = 2d\sin\theta \tag{7.1}$$

In this equation, n is any integer, d is the spacing between the diffraction planes, θ is the incident angle and λ is the wavelengths of the X-ray beam. Due to the constructive interference, the detector will observe several high intensity spots. By varying the incident angle, the sample can be tested for wide range of diffraction angles.

8

Experimental Results

The experimental results are presented in three sections. First, the CV-measurement results from the increased electrolyte stability are presented. Then, the results from the XRD and CV measurements of the electrode materials NTP, $Na_{0.44}MnO_2$ and NDMe are given. In the last section the observed side-reactions during the CV measurements is described.

8.1. Increased electrolyte stability

8.1.1. Non-active electrodes

Stainless steel and carbon cloth were tested thoroughly and showed significant and unpredictable side-reactions. These are discussed in section 8.3. Following the research strategy discussed in section 7.1.2, the more expensive and less reactive titanium was therefore acquired. The titanium mesh showed a more reliable behaviour as repetitive testing with the same procedure yielded comparable results. A proper CV procedure was established, aiming for the optimal ratio between a high scan rate and high details.

8.1.2. CV procedure

The resulting CV procedure for measuring the stability window of the aqueous electrolytes consists out of specific settings that are specified for the used of the open test-cell, the dimensions of the used separators, non-active electrodes and electrode material. The most important parameters are summed up in the following list.

Start/Stop voltage	0.0 V vs V_{ref}
Upper/lower Vertex	2.0 V / -1.5V vs V_{ref}
Scan rate	5 mVs
Step	1 mV
Cycles	3
Cut off current	$1 \times 10^{-3} > A < -1 \times 10^{-3}$
Reverse when	dPdt > 0 AND $A > 2 \times 10^{-6} A$ for 6 detections
Reverse when	dPdt < 0 AND $A < 2 \times 10^{-6} A$ for 6 detections

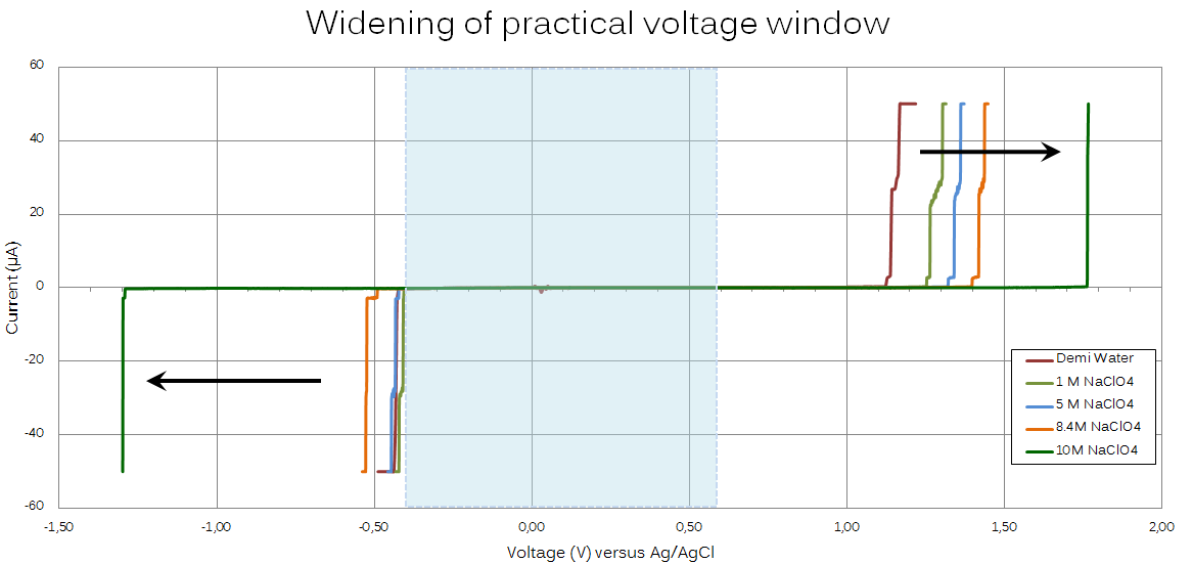

Figure 8.1: The widening effect of increasing $NaClO_4$ concentrations on the practical stability window of water.

8.1.3. Effect of $NaClO_4$ concentration

Using the same CV procedure for the measurements of the different electrolyte salt concentrations, results were obtained for distilled water and solutions of 1M, 5M, 8.4M and 10M of $NaClO_4$. The resulting curves indicate the stability window of the electrolytes by the sudden increase of the measured current. When a current is measured, an electrochemical reaction takes place, hinting for the decomposition of water. The curves of all electrolytes are combined in figure 8.1. The blue box indicates the theoretical thermodynamic stability window of water with a pH of 7.

A number of observations can be made from this figure. Firstly, it is clearly visible that for increasing salt concentrations the stability window is structurally enlarged on the cathodic side. On the anodic side there is only a little widening up to 8.4M concentrated electrolyte, making the observed offset for the 10M concentrated electrolyte unexpected. When neglecting measured currents up to 1 µA, the stability windows for all the electrolytes can be obtained by calculating the absolute difference between the potentials last applied before developing a current. These values are provided in table 8.1.

The total offset on the anodic side is 0.868 V, and on the cathodic side 0.639 V. Put together, the total stability window has increased with 1.508 V. This implies that the addition of $NaClO_4$ can lead to a increase in the practical stability window with a factor of roughly 2.

Upon close inspection in figure 8.1, small current peaks can be observed at voltages near 0.0 V versus Ag/AgCl. This has been neglected and assumed to be insignificant side reactions only at the start of the CV measurements. Another observation is the characteristic shape of the current profile on the boundaries of the stability window. At the cathodic side (right), the current profile seems to describe three steep increases, the first one being the smallest. On the anodic side a similar trend can be observed. This pattern could potentially indicate different types of reactions to occur outside of the stability window.

Table 8.1: Overview of the voltage windows for different electrolyte salt concentrations, measured in V versus Ag/AgCl

	Demi water	1M $NaClO_4$	5M $NaClO_4$	8.4M $NaClO_4$	10M $NaClO_4$
Lowest stable potential (V)	-0,423	-0,406	-0,422	-0,490	-1,291
Highest stable potential (V)	1,123	1,253	1,321	1,397	1,762
Stability window (V)	1,546	1,659	1,743	1,887	3,054

8.2. Half-cell testing

8.2.1. XRD of electrode materials

For each obtained electrode material a XRD-scan was made. The synthesis route for $NaTi_2(PO_4)_3$ of Nakamoto et al [36] could not be finished, as an essential device was not operational during the timeframe of this research, and is therefore omitted from the analysis.

In figure 8.2, the XRD scan results for $NaTi_2(PO_4)_3$, made via the synthesis route of Wu et al [66] are shown in green. The best candidate from the database was indeed NTP and matched with a score of 77, scale factor 1.012. The location and intensity of the peaks of the candidate are indicated in black, directly above the XRD profile of the sample. Although the match score is substantially high and most peaks overlap with the NTP candidate profile, it can be noted that especially for high diffraction angles, many peaks from the NTP candidate XRD profile are barely observed in the XRD profile of the sample. However, this could imply possible deviations in purity, or the presence of additional compounds. But, the missing small peaks are no reason to doubt the successful synthesis of NTP.

In figure 8.3 the XRD profile of the obtained $Na_{0.44}MnO_2$ is shown in red. In a similar fashion, the best matching candidate is selected from the database. Again, the best matching compound is in fact the $Na_{0.44}MnO_2$ as previously determined by others. The match score is 68 with a scaling factor of 0.657. The highest intensity peaks are all explained by the candidate profile. This contributes to the claim that $Na_{0.44}MnO_2$ has been successfully synthesized using the previously selected synthesis route. [64, 66]

In the third XRD profile the results for NDMe can be seen. No recorded XRD profiles were available in the database, so it is not a coincident not to find any highly matching candidates. The profiles shows only a few peaks, of which the peak at 65°is dis-proportionally large, with the second and third largest peak having diffraction angles at 78°and 14.8°. The absence of noise in the profile and the narrow and high peaks indicate that the material has been successfully synthesized.

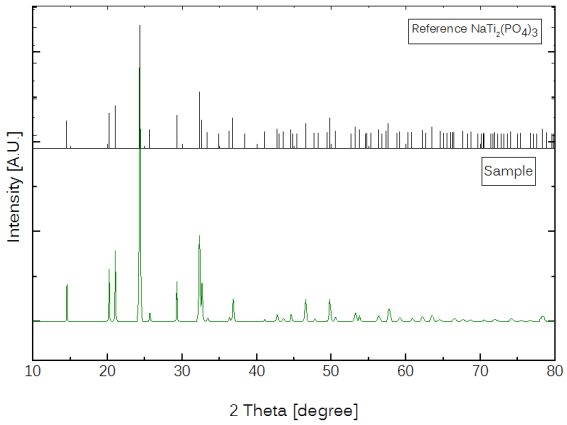

Figure 8.2: XRD scan of NTP including candidate

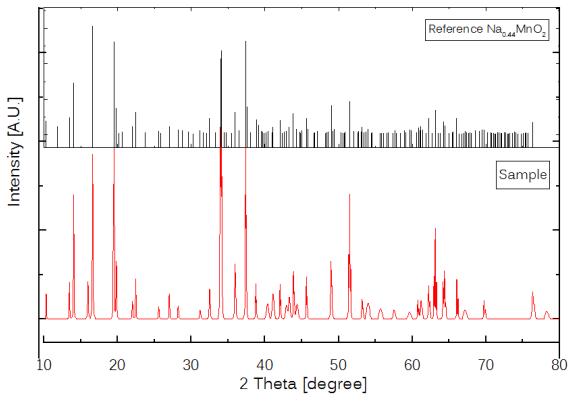

Figure 8.3: XRD scan of NaMnO2 including candidate

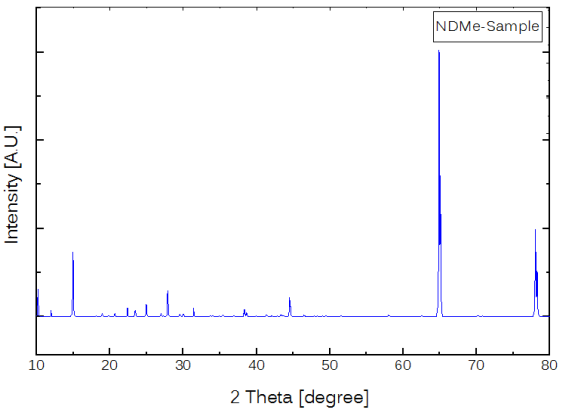

Figure 8.4: XRD scan of NDMe, no candidate available

8.2.2. Cyclic voltammetry half-cell

After confirming the successful synthesis of the electrode materials, the activated carbon mixed slurries of $Na_{0.44}MnO_2$, $NaTi_2(PO_4)_3$ and NDMe were coated on stainless steel (316) and dried in an oven at 70°Celsius. Subsequently, the coated strips were inserted in the three-electrode half-cell setup as described in section 7.1.1, with a titanium mesh strip as counter electrode. Copper foil was wrapped around the tips of the electrodes, for corrosive metal clips to be left out from the setup, reducing side reactions.

For all three electrode materials the same procedure has been used in order to enable comparison. In accordance to previous studies using CV measurements for the electrode materials $Na_{0.44}MnO_2$, $NaTi_2(PO_4)_3$, the scan rate was set at 0.5 mV/s and the potential range was adjusted in such a way to show the hydrogen and oxygen evolution lines, for anodic and cathodic half-cell testing, respectively.

The results of the CV measurements of $Na_{0.44}MnO_2$ are presented in figure 8.5. A number of observations can be made from this figure. Firstly, there are 3 clear peaks at roughly 0.7 V, 0.5 V and 0.3 V versus the Ag/AgCl reference electrode. The peaks seem to be mirrored to a large extent by the valleys, that have offset of roughly 0.2 V. The steep increase on the right hand side is the oxygen evolution which matches the previously discussed stability window of 10 M $NaClO_4$. The four cycles seem to greatly overlap and do not show a structural deviation at specific potentials, indicating stable insertion/extraction of sodium.

The results of the CV measurements of $NaTi_2(PO_4)_3$ are presented in figure 8.6. It should be mentioned that during the measurements many unexpected and extreme side-reaction currents were observed. In order to provide insights in the redox behavior of $NaTi_2(PO_4)_3$, these presumed side-reaction effects are removed from the data set. In addition, a damping factor (0.98) has been applied in the data analysis tool[1] in order to arrive at a smooth curve. The omitting of the side reactions and the application of the damping effect are discussed more elaborately in section 9.2.1.

The $NaTi_2(PO_4)_3$ CV curve in figure 8.6 shows a clear and almost perfectly mirrored redox couple, at - 0.65 V/ -0.75 V versus Ag/AgCl. On the left, the hydrogen evolution is visible, which indicates the NTP redox to be fully in the stability window of 10M $NaClO_4$.

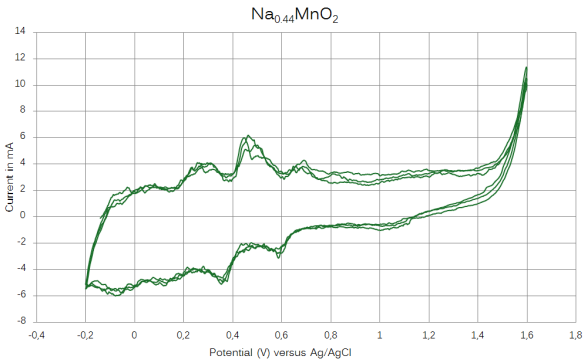

Figure 8.5: Cyclic voltammetry results of $Na_{0.44}MnO_2$ at 0.5mV/s in 10M $NaClO_4$.

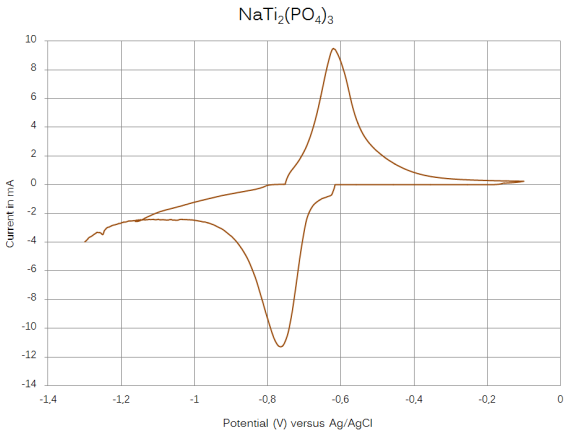

Figure 8.6: Cyclic voltammetry results of $NaTi_2(PO_4)_3$ at 0.5mV/s in 10M $NaClO_4$.

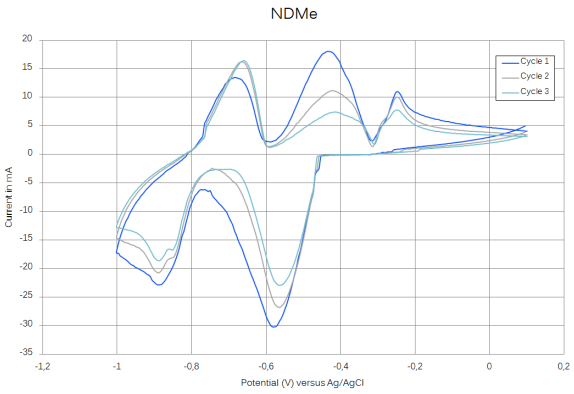

Figure 8.7: Cyclic voltammetry results of NDMe 5mV/s in 10M $NaClO_4$.

[1] Damping factor applied with Analysis Toolpak in Microsoft Excel©.

The CV measurements of NDMe showed inconsistencies for testing at low scan rates. After three CV scans, each showing significant differences in peak widths, heights and potentials, a new cell was made and a different CV scan with a scan rate of 5 mV/s was tried. The results are shown in figure 8.7. After two cycles with large offsets, three almost identical cycles where measured. As this is the material of interest, the relative shapes of these cycles is important to analyze. It can be observed that cycling has an adverse effect on the size of both the peaks and the valleys, with the upper left peak as the only exception, as it slightly increases upon cycling. Overall, the peaks are very well to distinguish. Surprisingly, there are three oxidation peaks (pointing upwards), but only two apparent reduction peak (pointing downwards). Potentially, the third peak is positioned at more negative potentials.

8.3. Side reactions

In the process of determining appropriate non-active electrode materials, over 350 CV tests were done. It was found to be extremely difficult to find one specific procedure setting that would (1) yield reliable results for all electrolyte concentrations (2) would find virtually equal results when repeated on the same cell in the same environment and (3) would stay in within the boundary conditions of invested time per measurement. All sorts of non-ideal behaviour have been observed, including hardware and software issues such as a recurring offset of exactly 1.0 V, sudden ohmic behaviour of cell-components, unexpected current increases at low potentials, unexpected low currents at high potentials, rust and crystalline precipitation and degradation and dissolution reactions of the non-active electrode materials. A number of recurring problems are described in detail here, and will be furthermore discussed in section 9.2. Photographs show a selection of the observed side reaction processes, presented in appendix I.

8.3.1. Stainless steel corrosion

More than once, brownish precipitation has been observed on the stainless steel electrode even after testing in low $NaClO_4$ concentrations. This could indicate that the iron in stainless steel somehow oxidizes, resulting in iron oxide, also known as rust. The electrode materials from 'Mike'-series showed particular remarkable forms of brownish rusty reaction products after a series of long tests. Driven by the curiosity to know the composition of the reaction products, a XRD measurement was done for the rusty crystalline precipitation. The outcomes for this XRD scan are presented in figure 8.8.

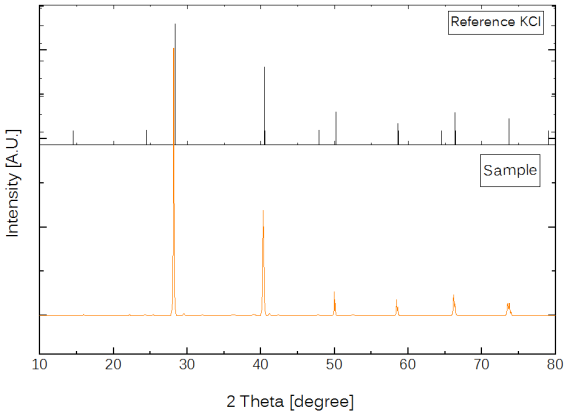

Figure 8.8: XRD profile of the precipitation on the stainless steel electrode.

The XRD peaks are remarkably sharp and clear, which suggests few different chemical compounds in the sample. Often this is a sign of a highly pure crystalline compound. Two chemical compounds were selected as best matching candidates. Potassium Chloride (KCl) had a high matching score of 78, and Potassium Sodium Chloride ($ClK_{0.6}Na_{0.4}$) had a lower matching score.

Because there is no source of Chloride anywhere near the test-cell setup besides the reference electrode which is internally filled with 3M KCl, it can be stated with a high certainty that the reference electrode somehow leaked its inner fluid. Another possibility for the contamination is the crumbling of the precipitation that 'grows' near the filling hole of the Ag/AgCl reference electrode upon prolonged testing. This precipitation is not an indication for failure, but can naturally occur during testing.

But the discovery of the reactive salt from the Ag/AgCl reference electrode did not describe the observed rust formations observed in previous test series. Evidence of the unexplained steel corrosion can ben found in appendix I.

8.3.2. Side reactions with test setup

Two other phenomena led to severe side reactions. The metal clips that are usually used for half-cell testing, are not stable when in contact with electrolyte and the voltage. Normally, the clips serve usually for the firm connection between the CV Autolab machine and the (dry) sealed test sample. But the metal clips are now used in a open cell, in proximity of an aqueous electrolyte, so the clips could get wet and start reacting when high voltages are applied. This leads to severe disruption of the CV measurements. Furthermore, it was discovered that the capillary effect was the main reason for the metal clips to get wet, causing them to react. The capillary effect can be understood by the the counter-gravitational force of a material on a liquid. It is therefore possible for ions to move upwards through a material. Painting the metal clips with a carbon coating did not prevent the metal clips from reacting.

For a moment a practical solution seemed to be found. By enlarging the non-active electrode with roughly 5 centimeters, the vertical distance for the reactive ions to reach the metal clips by the the capillary effect would become too large. A remarkable observation was made with long carbon strips in the 'Lima' test series. After stable measurements for destilled water and 1M $NaClO_4$, a very big reaction was observed in the test for 5M $NaClO_4$ at low applied voltages, suggesting a parasitic reaction with the carbon cloth and highly concentrated $NaClO_4$.

Testing the stainless steel with long strips were not found reliable for another reason, namely an unlikely narrow stability window of the electrolyte. The measured electrochemical window for destilled water and 1M $NaClO_4$ solutions was roughly 1.1V, which lies under the thermodynamic stability window. A theory of 'short-cutting' the Pourbaix diagram by temporarily and locally changes of pH values in micro-cavities in the separator could not be backed up by repetitive testing for pH changes, as no changes were observed at all.

Testing with titanium mesh yielded reliable results from the start. Repetitive testing of the same protocol for the same test cell yielded structurally in the same or very similar results. Because risking side reactions from the metal clips could have potentially ruined the expensive titanium mesh, a solution was found by wrapping coper foil around the tips of the titanium mesh and the metal connectors, effectively manually forming a copper 'dread'.

9

Interpretation and discussion

9.1. Interpretation of results

The results of the experimental part can be logically divided into two sections: (1) the CV measurements for the electrolytes with different concentrations of sodium perchlorate and (2) the CV and XRD measurements of the active electrode materials.

9.1.1. Improved stability window

The improved stability window for 10M $NaClO_4$ is a very promising result. On both the anodic and cathodic side, the hydrogen or oxygen evolution is suppressed. This translates into an anodic over-potential of 0.868 V and a cathodic over-potential of 0.639 V, comparing it with the practical stability window of distilled water, under the same circumstances. When assuming this stability window to be independent of the scan rate, which is debatable (see section 9.4.2), this opens up the possibility to use a wide range of previously unconsidered electrode materials for aqueous sodium-ion batteries. To quantify this and to gain insight into the available types of electrode materials with their potential range, an illustration by Larcher et al [28] is reproduced in figure 9.1. In this figure, the thermodynamical stability window of water is indicated in blue, the practical window in violet and the here presented improved 10M $NaClO_4$ stability window in light green.

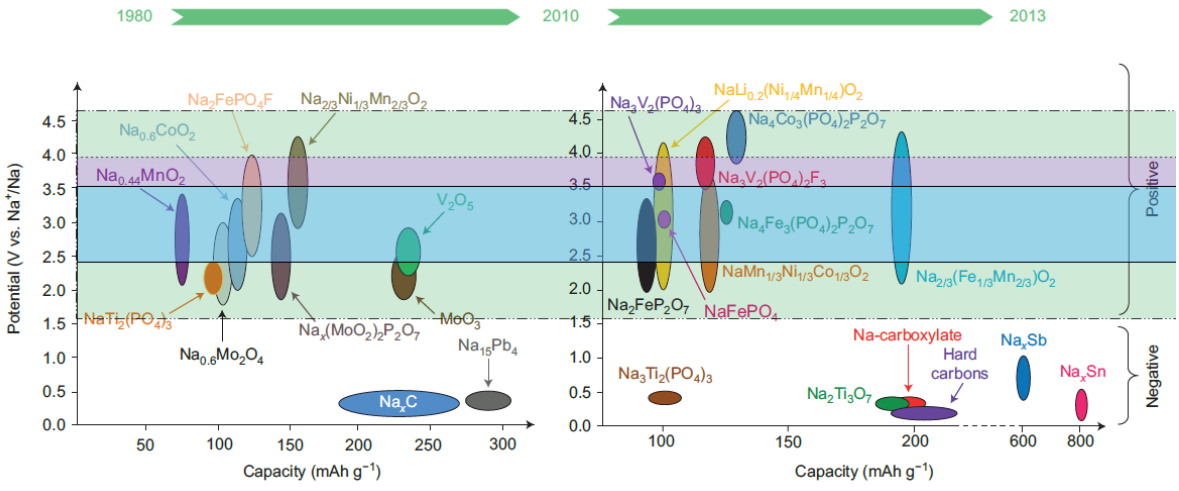

Figure 9.1: Sodium ion electrode materials including different electrolyte stability windows.

Looking at figure 9.1, two cathode materials can be identified that are theoretically not stable in water, but are stable in high $NaClO_4$ concentrated electrolyte, namely $Na_3V_2(PO_4)_2F_3$ and $Na_4Co_3(PO_4)_2P_2O_7$. It should be noted that this overview is not an inclusive lists, as many new electrode materials are reported regularly. However, it can be seen that the carboxylates, hard carbons and sodium carbon combinations are well below the hydrogen evolution line. This is a pity, because many promising findings in sustainable, biologically derived carbon anodes have been reported lately.[38, 70, 73]Besides from the too low potentials to be used in aqueous sodium-ion batteries, such organic carbons are in the same line as the overall objective of our research group to combine the most affordable and safe materials to enable cheap bulk storage.

9.1.2. Half-cell CV tests

Both the half-cell CV test results for $NaTi_2(PO_4)_3$ and $Na_{0.44}MnO_2$ were executed at 0.5 mV/s, and both showed significant hyperfast fluctuations in the measured current, which complicates the analysis of the CV curves. Usually, more details are obtained when scanning at low scan rates, when using an inert, protected and sealed test cell. Is is frustrating to witness a different relation when testing with the open test-cell, as comparing the obtained results with previously reported findings is most useful when the same test conditions are used. The main reason why the tendency could be different for in the open test-cell used in this research project is the constant possibility for oxygen exchange between the air and the water. Is has been previously reported that especially fully charged cathodes urgently need protection from the in water dissolved oxygen.

Besides the suspected adverse characteristics of the open test-cell to have a oxygen dissolved in it, there is another concern. Several measurements for the NDMe show significant differences in cyclic voltammetric curves for different salt . This is an important discussion point, because the eventual selection can be made with a biased towards which curve 'looks' the nicest or which shows the lowest or highest peaks. In this way, the researcher is tempted to 'shop' for the settings that get the desired outcomes, while it is scientifically more valuable to look for the most accurate measurements or to mimic processes from the natural world. A standardization of test procedures, also for deviating test-cell designs, could be a fruitful idea to align findings and enable fair comparisons.

Independent from the exact settings of the CV measurements of NDMe, All redox peaks lie within the stability window of 10M $NaClO_4$. This invites for the assembly of a full cell based on NDMe/$Na_{0.44}MnO_2$ as anode/cathode couple, which is the most logical step from the results presented here.

An important factor to keep in mind before preparing such an experiment is the effect of dissolve oxygen on the charged cathode material, reported by Luo et al. [33] It is therefore advised to either test in an oxygen free electrolyte, or in a sealed test-cell (or both), as the total oxygen dissolved in the electrolyte could only lead to a few percent of capacity fading, if it is not replenished by the free interaction with the air. [66]

9.2. Description of side-reactions

9.2.1. $NaTi_2(PO_4)_3$ CV side reactions

The results of the $NaTi_2(PO_4)_3$ half cell CV measurements were adjusted and damped in order to provide a smooth curve. This was done because of the disruptive effect of the large currents measured due to the presumed side reactions. Upon inspection of the data, a pattern was found in the occurrence of the side-reactions. The uncorrected results are presented in figure H.1 in appendix H. In between -1.26 V and -1.22 V v and near -0.62 V versus Ag/AgCl, sudden increases and decreases in the measured current occurs. Strangely enough, these sudden increases develop within half a second and are a multitude higher than the maximum currents involved in the $NaTi_2(PO_4)_3$ redox reaction. When comparing the data of the consecutive cycles, the observation was made that for a number of exactly similar potentials, the high sudden peak currents were recorded. These values are -0.62027 V, -0.62277 V, -1,23550 V, -1,24039 V, -1,24283 V, - 1,24526 V, -1,24542 V and -1,24771 V versus Ag/AgCl. It is hard to believe an actual chemical reaction takes place as an increasing slope towards high currents is generally the indicator of a chemical reaction. For all observed spikes, no increasing slope was preceded. Both the recurrence of exactly the same peak potentials and the absence of a sloping

current make it unlikely a chemical side-reaction takes place. It can therefore be argued that there might be a software or hardware related problem with the Metrohm Autolab CV measurement device, leading to measurement errors in the form of high currents.

Whether these expected measurement errors have had a significant impact on the reliability of the results as presented in figure 8.6 is questionable. Structurally after a current spike was observed, it took a few seconds to return to normal currents. This shows the interaction between the current spike and the current measured from the sample. As large currents tend to be malicious to electrode materials and usually inflict a high rate of capacity decay, it is expected that the CV measurement with the possible errors in software or hardware have caused for unintended damage.

9.3. Comparison with other studies

9.3.1. Electrolyte stability window

The studies of Nakamoto et al [36] and Li et al [30] formed the basis of the theoretical framework of using a range of increasing $NaClO_4$ salt to discover the influence on the stability window of aqueous electrolytes. It is therefore most logical to compare the results with those two studies. The reported stability window of 17m (equal to 10M) $NaClO_4$ by Nakamoto is almost identical to the one found in this research. This suggests that the open test-cell does not derogate the stabilizing effect of $NaClO_4$ on pure water.

A high ionic conductivity is a benign property for electrolytes. The conductivity of $NaClO_4$ increases with increasing concentrations up to roughly 5M, where maximum conductivity of 170mS/cm^2 has been determined. For even more increasing concentrations, the conductivity declines, due to the effect of increased static electrical force between the ions at decreased inter-molecular distance. Thus, the static force starts to impede the movement of ions. [66] Although conductivity for aqueous electrolytes is generally orders of magnitude larger than organic electrolytes, it is important to assess critically what other implications the super concentrated $NaClO_4$ electrolyte has.

9.3.2. Electrode performance

The XRD data clearly shows sufficient evidence that the materials $NaTi_2(PO_4)_3$ and $Na_{0.44}MnO_2$ were obtained in acceptable purity. Therefore the CV measurements can be assumed to represent the behaviour of the two materials. Comparing the CV results with the characteristic found by others, the resemblance is striking. The results of the NTP CV results to Part et al [40] en Wu et al. [66] are shown in figure **??**. By the similarities, is can be safely concluded that NTP shows proper redox behavior in the open test-cell used in this research. The MSE reference electrode works with a standard potential of is 0.64 V versus SHE, while the Ag/AgCl reference electrode used here 0.197 V versus SHE.

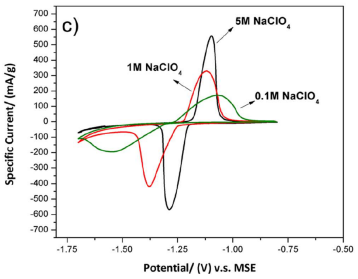

Figure 9.2: Wu et al. [66]

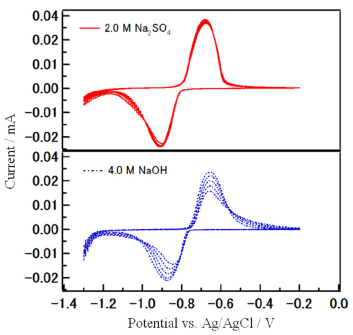

Figure 9.3: Park et al. [40]

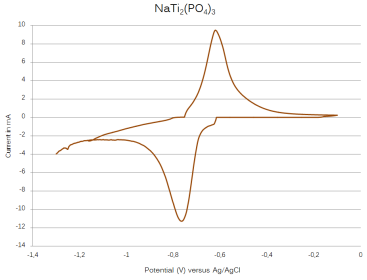

Figure 9.4: Own findings

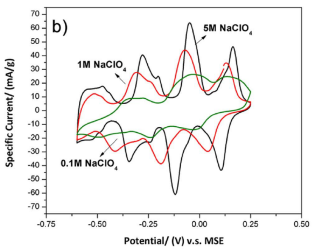

Figure 9.5: Wu et al. [66]

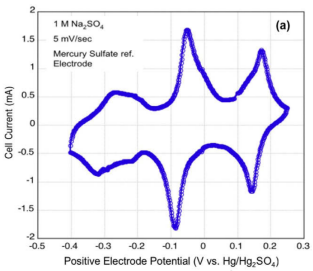

Figure 9.6: Whitacre et al. [64]

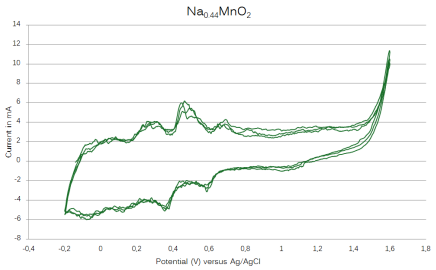

Figure 9.7: Own findings

Similarly, the results for $Na_{0.44}MnO_2$ are compared to the results of Wu et al [66] and Whitacre et al. [64]. At first sight the curves do not look similar. However, focusing only at the left side of the $Na_{0.44}MnO_2$ CV curve in figure 9.7, the two-and-half characteristic peaks and valleys can be distinguished. Combined with proper match from the XRD scan, there is not much doubt whether these redox peaks are caused by $Na_{0.44}MnO_2$. However, more interesting to see is the relative location to the oxygen evolution line, which is indicated by the upward curl on the right side of the graph in figure 9.7. All redox peaks are well within the stability window.

A point of uncertainty arises from the fluctuating course of the data set of the CV scan of $Na_{0.44}MnO_2$. The graph in figure 9.7 is smoothed using a damping factor (0.98) but still shows fluctuating behaviour. This might be caused by a possible low mass loading, or by side reactions with the oxygen. Dissolved oxygen is known to react with charged cathode materials, and because the open test-cell is exposed to atmospheric oxygen this could explain the continuous fluctuations. It would be interesting to see if sealing the open test-cell would change the outcomes, in order to provide evidence for this assumption.

9.4. Reflection and revaluation

Scientific work requires critical attitude towards own research results, methods and objectives. Over the course of the research there have been several valuable discussion topics that challenge the feasibility of improving the stability window of the aqueous electrolyte or in a wider scope the feasibility of aqueous sodium-ion batteries in general. These topics will be summarized in a number of arguments and will be discussed sequentially.

9.4.1. Salty concerns

Firstly, the addition of high amounts of salt inflicts extra costs for the fabrication of the electrolyte. This is in conflict with the one of the most important motivations for research to aqueous sodium-ion batteries, which is the selection of the most abundant and safe materials to achieve maximum affordability. Secondly, because 10M $NaClO_4$ is close to the saturation boundary (at 25° Celsius), crystallization of the salt upon electrode material is not unlikely in colder environments or in case of evaporation of water. This effect is known in some battery chemistries, but has not been research for the combination of $NaClO_4$ in aqueous sodium-ion batteries, as far as the writer is concerned. This places an inconvenient uncertainty for the impact of high salt concentrations on the capacity fading and thus lifetime of the battery. This has an indirect impact on the affordability as well.

Furthermore, concerns about the safety of the battery assembly must also be taken seriously. Sodium perchlorate is a very strong oxidizer and is known to interact with organic liquids in an explosive way.[35] Therefore, the undissolved salt requires proper storage, shipment and handling. Because aqueous sodium-ion batteries are often portrait as the better option for future large scale stationary energy storage, large battery systems and assembly facilities will be needed. Using sodium perchlorate as sodium salt of choice will thus require bulk shipments and storage. Solutions might be easy to practically implement (dissolve before shipping and storing), but before the actual dangers are known, a critical attitude will not be unwise.

Another argument that contributes to a critical attitude towards high concentrations of sodium salts is the corrosive effect on active materials. Some scholars have expressed their concerns about the corrosive effect, not per-se directly but also indirectly because of the higher electrochemcial potentials.[66] In the findings of this work, there has also been several indications that not only the active material, but also the supposed non-active material undergoes side-reactions that were not expected. This puts more constraint on the materials used in a the battery system.

9.4.2. Important factors

During the search for an appropriate procedure for the CV measurements, the effect of the scan rate on the outcomes were observed. Apparently, the scan rate does not just dictate the speed, but also the outcomes of the test in several different ways. Different scan rate settings, while all other parameters are kept equal, can shift redox peaks, show different currents for the same potentials and hide parasitic reactions. [55]. It is known that fast scan rates tend to overestimate the stability window of electrolytes. In this work, a scan rate for the electrolyte CV tests was eventually set at 5 mV/s, in accordance to many scholars. However, Suo et al. suggest a much lower scan rate (0.1 mV/s) which would simulate an actual battery better and thus result in more reliable results.

A shortcoming in this work is thus a quantification on the influence of the scan rate on the outcomes of the stability window. To enhance the relevance of this influence, a realistic charge/discharge profile for stationary large-scale batteries could be tried. This could also settle the debate about whether galvanostatic, potentiostatic or constant current measurements [63] provide the most accurate outcomes by testing for realistic scenarios. Another suggestion is to quantitatively determine the effect of dissolved O_2 in aqueous solutions. Although it is a known fact that many charged cathodes will react with the dissolved oxygen in water. An effective measure to counterbalance this is by purging the electrolyte for a prolonged time with pure nitrogen gas. an react with charged cathodes and can thus result in capacity fading during cycling. [33]

III

Third part: Conclusions and Recommendations

10

Conclusions and recommendations

10.1. Conclusions computational work

The aim of the computational part of this research was to gain fundamental insights in electrochemical properties of two organic crystals, NDMe and NDTo, upon sodium insertion. This is done, by first identifying the most stable binding spots in the crystal lattices, and consequently monitoring the sodiation pathway. From the relaxation energies from the most stable configurations, the enthalpy of formation could be calculated unveiling the thermodynamically stable states. By this, the voltage profiles could be established.

Upon sodium insertion, N,N' –bis(methyl)- 1,4,5,8-naphthalene diimide (NDMe) appears to share sodium atoms with three surrounding molecules in the crystal lattice in so called Triple Binding Spots (TBS). Until a sodiation fraction of 0.5, it shows a voltage plateau at 1.78 V versus Na/Na^+. Further sodiation is calculated to happen at roughly 0.4 V versus Na/Na^+. The second organic molecule N,N' –bis(p-tolyl)- 1,4,5,8-naphthalene diimide (NDTo) appears to share sodium atoms between in two or four molecules, forming Dual Binding Spots (DBS) or Quartet Binding Spots (QBS). The voltage profile of NDTo suggests a sloping voltage between 2.05 V and 1.2 V until a sodiation fraction of 0.5, followed by a rather low voltage plateau at 0.24V versus Na/Na^+ until full sodiation.

Another aim of this research was to assess the significance of the Van der Waals corrections in the accuracy of the computational calculations compared to the available experimental data. For both the DFT calculations of NDMe and NDTo, the zero damping DFT-D3 method of Grimme [12] is found to be best correction for the Van der Waals interactions. It is found to be of crucial importance to include a Van der Waals correction method in the DFT calculations, as the Van der Waals force tends to increase for molecules with many atoms and with large surfaces. Without Van der Waals corrections, the outcomes of the DFT calculations show without exceptions large deviations from experimental data in all cell parameters. For NDTo, the Van der Waals corrections show more significance for an increasing fraction of sodiation.

Even with corrections, both organic crystals show extreme lattice distortions upon sodiation. NDMe shows a volumetric change of 14,73% upon full sodiation with changes in vector lengths up to 50,13%. NDTo shows a volumetric change of 8,24% upon full sodiation with changes in vector lengths up to 10,41%. These large lattice distortions demand the crystal structure to have an exceptionally high flexibility to prevent material degradation when applied in a working battery. This inflicted high requirement calls for the revaluation of NDMe and NDTo as robust anode materials based on computational findings as presented here.

Combining the insights that the computational calculations have provided, i.e. a sloping and rather low voltage plateaus and the high volume expansion and lattice distortion for both NDMe and NDTo, there is sufficient evidence to conclude that both crystalline NDMe and NDTo show undesired electrochemical characteristics which disqualify them as promising anode materials.

10.2. Conclusions experimental work

The overall aim of the experimental work was to assess the feasibility of $NaClO_4$ to be used in improving the aqueous electrolyte for affordable aqueous sodium-ion. Solutions with different concentrations of sodium perchlorate ($NaClO_4$) have been tested in a three-electrode open test cell to find evidence for an enlarged electrochemical stability window compared to that of distilled water. At a concentration of 10M, close to the saturation limit, the solution shows a stability window between -1.29 V and 1,762 V versus Ag/AgCl, effectively offering a stability window of 3.05 V. In order to test its applicability with an organic anode material, NDMe has been obtained and tested in 10M $NaClO_4$ versus a titanium counter electrode. For comparison and to proof the open test-cell design not reported elsewhere, two easy to synthesize inorganic electrodes that are elaborately described in previous studies have been selected.

NDMe shows redox potentials that are well within the improved stability window. However, strong capacity fading was observed upon the first cycles. Due to the open test-cell, dissolved oxygen has all the chance to react, as it is replenished. However, capacity fading can only be assesses when correspondent measurements and cycle-tests are performed. The suggestions made in this research invite for future research starting from there.

The last experimental research aim was to assess the impact of highly concentrated $NaClO_4$ solutions on the safety, environmental and cost of an future aqueous sodium-ion battery. A general scientific consensus is reached on the benefits of highly concentrated electrolytes (amongst them $NaClO_4$) on the electrode performance and indirectly the cycle life, improving the affordability in its turn. However, as $NaClO_4$ is a strong oxidizer so it inflicts serious safety issues during shipment, storage and assembly the battery. A positive characteristic of $NaClO_4$ is the abundance of the consisting elements. Taking all these insights into consideration I would like to conclude with expressing both the great potential indicated by previous studies to enhance battery performance, and the need for both fundamental and experimental research in order to make a more nuanced and elaborate decision whether or not and under what conditions it benign to use such high concentrations of an explosive oxidizer.

10.3. Recommendations

10.3.1. Other promising organic anodes

Organic crystals show great promise as sustainable and cheap anode materials for aqueous sodium-ion batteries. Capacity fading caused by side reactions or big volume changes is one of the main reason this field needs more research attention. Many reported organic crystals or polymers show a remarkable flexibility. Krishna et al. [26] report a wide range of hyper-flexible organic compounds. In this thesis, the computational analysis of two compounds failed prematurely due to unclear reasons. However, there is enough reason to believe that those organic crystals (the 'brothers' of NDMe and NDTo) show good electrochemical behaviour and mechanical strength. These compounds are called N,N'-bis(n-propyl)-1,4,5,8-naphthalene diimide and N,N'-bis(p-tertiarybutylphenyl)-1,4,5,8-naphthalene diimide.

One of the main arguments to consider organic crystals for aqueous sodium ion batteries is the great abundance of the elements used in organic molecules and with that an assumed great affordability. Approaching the situation from the other perspective could be to research the cheapest materials (instead of the elements) on earth. Waste materials for example, can have negative prices and explorations to find possibilities to make batteries from those materials could thus be very appealing.

10.3.2. Different battery chemistry

Aqueous sodium-ion batteries are paralleled by other battery chemistries offering more sustainable, more affordable, less toxic and less flammable alternatives to lithium ion batteries. Although I believe in the feasibility of simultaneous research in various battery technologies, it is also important to avoid a tunnel vision for a specific chemistry, when it is widely proven to be inferior to other chemistries in important factors. One

of the most interesting alternatives is the innovative setup involving both an organic and an aqueous electrolyte, as proposed by Senthilkumar [49]. Interchangable cathode materials and the use of seawater are both interesting concepts for affordable large scale sodium-ion battery systems.

10.3.3. Suitable electrolyte research methods

I strongly recommend to timely acquire appropriate testing materials to prevent waste of time, energy and money on inaccurate measurements. In retrospect it would have helped me greatly if I would have had access to a prefabricated, accurate and user friendly electrolyte tester, as developed by numerous suppliers, amongst them Metrohm Autolab. In the same line to this argument is the importance of the uniformity of the test-cell dimensions and parameters, to enable comparison with the experimental results by others. As far as I know, the open test-cell that has been used extensively during this research project has not been used by other scholars, making it difficult to establish the same testing environment (electrode surface, area between electrodes, etc.) in order to compare it with results by others. Besides that, a new type of test-cell that is air tight is strongly recommended.

As discussed previously, a shortcoming in this thesis is the uncertainty in the influence of the scan rate on the outcomes of the stability window. Battery testing could be taken to a new level if a realistic load profile is used for the charge and discharge rates, depths and intermediate waiting times. This could also settle the debate about whether galvanostatic, potentiostatic or constant current measurements [63] provide the most accurate outcomes by testing for realistic scenarios. Another suggestion is to quantitatively determine the effect of dissolved O_2 in aqueous solutions. There is some evidence that charged cathodes will react with the dissolved oxygen in water. An effective measure to counterbalance this is by purging the electrolyte for a prolonged time with pure nitrogen gas. [33]

Epilogue

This research project has been an exceptional experience to me in many different ways. Being driven by intrinsic motivation and operating in a positive and professional social environment, I was able to discover both computational and experimental battery research. Serving as the completion of my tentative scientific education, this research project has been the most challenging and versatile all efforts I have done previously. In retrospect I see how my attitude towards scientific research has changed from finding it sluggish and dull into contagiously interesting. The appreciation for scientific battery research has increased to the point I genuinely like to read, which is a very peculiar thing for the people that know me well.

Large scale and affordable energy storage is the missing link for the spectacular energy transition that awaits us in the coming years. I believe it is useful to simultaneously research multiple innovative technologies that are fundamentally based on different principles and materials, as I do not believe that the aqueous sodium-ion battery is the only suitable solution. The continuous awareness of the importance and relevance of energy storage research for the sustainable energy transition resulted in an inexhaustible source of intrinsic motivation in the research project which made it fairly easy to progress. This insight is a valuable lesson that I kindly take with me in my future career.

Certainly it was not just the developed intrinsic motivation that made me so satisfied with the overall project. In fact, I found the social environment remarkably nice to work in. The social interaction between battery-team members and the management from the supervisors are both things I would like to highlight here. The unforced and laid-back management style of Marnix Wagemaker, head of the department for Storage of Electrochemical Energy (SEE), makes students feel fully in charge of their research project. This shapes the environment in which students propose their own deadlines, keep track of their progress and explore interesting new research directions without external pressure. Although this might not work best for everyone, I have prospered on this. Therefore I would like to thank Marnix for his leadership and supervision during my research project.

For an inexperienced student an involved and accessible daily supervisor is essential for a steep learning curve. Always being witty and approachable, I have been lucky Alexandros Vasileiadis. Ευχαριστώ πολύ for your daily supervision and many short talks, enthusiastic updates about new convex hull diagrams and tutoring me computational analysis based on Density Functional Theory.

Furthermore I have made extensive use of the knowledge and expertise of my colleagues, and would like to thank them all for a nice time together. Remco, your practical supervision in the laboratory has been fantastic, thank you very much. Also Frans, 'opperhoofd' of the laboratory, thanks for your sincere attention and infectious humor. All other members of the battery team with whom I have collaborated; without you there would not be any potential, thanks for all the positive energy!

Kajan Nando Kort
Delft, December 2017

Bibliography

[1] M. Andrzejak, G. Mazur, and P. Petelenz. Quantum chemical results as input for solid state calculations: charge transfer states in molecular crystals. *Journal of Molecular Structure: THEOCHEM*, 527(1):91 – 102, 2000. ISSN 0166-1280.

[2] F. Barzegar, D. Y. Momodu, O. O. Fashedemi, A. Bello, J. K. Dangbegnon, and N. Manyala. Investigation of different aqueous electrolytes on the electrochemical performance of activated carbon-based supercapacitors. *RSC Adv.*, 5:107482–107487, 2015. doi: 10.1039/C5RA21962K. URL `http://dx.doi.org/10.1039/C5RA21962K`.

[3] Theodore L. Brown, H.Eugene Jr LeMay, Bruce E. Bursten, Catherine J. Murphey, Patrick M. Woodward, and Matthew W. Stoltzfus. *Chemistry, The central science*. Pearson, 2015.

[4] Tomas Bucko, Jurgen Hafner, Sebastien Lebegue, and Janos G. Angyan. Improved description of the structure of molecular and layered crystals: Ab initio dft calculations with van der waals corrections. *The Journal of Physical Chemistry A*, 0(proofing):null, 0. doi: 10.1021/jp106469x@proofing.

[5] Bas Buise. N,n'-dimethyl-1,4,5,8-naphthalene-carboxylicdimide as electrode material for cheap large scale sodium ion batteries. Master's thesis, Delft University of Technology, 2017.

[6] Long Chen, Wangyu Li, Yonggang Wang, Congxiao Wang, and Yongyao Xia. Polyimide as anode electrode material for rechargeable sodium batteries. *RSC Adv.*, 4:25369–25373, 2014. doi: 10.1039/C4RA03473B. URL `http://dx.doi.org/10.1039/C4RA03473B`.

[7] Juan Carlos Cuevas. Introduction to density functional theory. URL `http://tfp1.physik.uni-freiburg.de/eu_www/Miraflores/lecturenotes/JuanCarlosCuevas_Talk.pdf`.

[8] Wenwen Deng, Yifei Shen, Jiangfeng Qian, and Hanxi Yang. A polyimide anode with high capacity and superior cyclability for aqueous na-ion batteries. *Chem. Commun.*, 51:5097–5099, 2015. doi: 10.1039/C5CC00073D. URL `http://dx.doi.org/10.1039/C5CC00073D`.

[9] Xiaoli Dong, Long Chen, Jingyuan Liu, Servane Haller, Yonggang Wang, and Yongyao Xia. Environmentally-friendly aqueous li (or na)-ion battery with fast electrode kinetics and super-long life. *Science Advances*, 2:e1501038–e1501038, 01 2016.

[10] Hossein Ghassemi and Allan S. Hay. Polyimides from n,n'diamino1,4,5,8-naphthalenetetracarboxylic bisimide. *Macromolecules*, 27:3116–3118, 05 1994.

[11] Stefan Grimme. Semiempirical gga-type density functional constructed with a long-range dispersion correction. *Journal of Computational Chemistry*, 27(15):1787–1799, 2006.

[12] Stefan Grimme, Jens Antony, Stephan Ehrlich, and Helge Krieg. A consistent and accurate ab initio parametrization of density functional dispersion correction (dft-d) for the 94 elements h-pu. *The Journal of Chemical Physics*, 132(15):154104, 2010.

[13] Chunyang Guo, Kai Zhang, Qing Zhao, Longkai Pei, and Jun Chen. High-performance sodium batteries with the 9,10-anthraquinone/cmk-3 cathode and an ether-based electrolyte. *Chem. Commun.*, 51: 10244–10247, 2015.

[14] Xugang Guo and Mark D. Watson. Conjugated polymers from naphthalene bisimide. *Organic Letters*, 10 (23):5333–5336, 2008.

[15] Jürgen Hafner, Christopher Wolverton, and Gerbrand Ceder. Toward computational materials design: The impact of density functional theory on materials research. *MRS Bulletin*, 31(9):659–668, 2006. doi: 10.1557/mrs2006.174.

[16] Elham Hosseini-Bab-Anari, Andrea Boschin, Toshihiko Mandai, Hyuma Masu, Kasper Moth-Poulsen, and Patrik Johansson. Fluorine-free salts for aqueous lithium-ion and sodium-ion battery electrolytes. *RSC Adv.*, 6:85194–85201, 2016.

[17] Zhiguo Hou, Xueqian Zhang, Xiaona Li, Yongchun Zhu, Jianwen Liang, and Yitai Qian. Surfactant widens the electrochemical window of an aqueous electrolyte for better rechargeable aqueous sodium/zinc battery. *J. Mater. Chem. A*, 5:730–738, 2017.

[18] R.A. Huggins. *Advanced Batteries, Materials Science Aspects*. Springer Science + Business Media, LLC, 2009.

[19] M. Saiful Islam and Craig A. J. Fisher. Lithium and sodium battery cathode materials: computational insights into voltage, diffusion and nanostructural properties. *Chem. Soc. Rev.*, 43:185–204, 2014.

[20] Remco van der Jagt. Aqueous sodium-ion batteries: acquiring new anode materials. Master's thesis, Delft University of Technology, 2016.

[21] Gerald Kettlgruber, Martin Kaltenbrunner, Christian M. Siket, Richard Moser, Ingrid M. Graz, Reinhard Schwodiauer, and Siegfried Bauer. Intrinsically stretchable and rechargeable batteries for self-powered stretchable electronics. *J. Mater. Chem. A*, 1:5505–5508, 2013. doi: 10.1039/C3TA00019B. URL `http://dx.doi.org/10.1039/C3TA00019B`.

[22] Dong Jun Kim, Young Hwa Jung, K. Kamala Bharathi, Sang Hyun Je, Do Kyung Kim, Ali Coskun, and Jang Wook Choi. An aqueous sodium ion hybrid battery incorporating an organic compound and a prussian blue derivative. *Advanced Energy Materials*, 4(12):1400133–n/a, 2014. ISSN 1614-6840. doi: 10.1002/aenm.201400133. URL `http://dx.doi.org/10.1002/aenm.201400133`. 1400133.

[23] Young Jo Kim, Wei Wu, Sang-Eun Chun, Jay F. Whitacre, and Christopher J. Bettinger. Biologically derived melanin electrodes in aqueous sodium-ion energy storage devices. *Proceedings of the National Academy of Sciences*, 110(52):20912–20917, 2013. doi: 10.1073/pnas.1314345110. URL `http://www.pnas.org/content/110/52/20912.abstract`.

[24] Youngjin Kim, Kwang-Ho Ha, Seung M. Oh, and Kyu Tae Lee. High-capacity anode materials for sodium-ion batteries. *Chemistry – A European Journal*, 20(38):11980–11992, 2014. ISSN 1521-3765. doi: 10.1002/chem.201402511. URL `http://dx.doi.org/10.1002/chem.201402511`.

[25] B. Kooger. Sodium insertion in ramsdellite tio2. Master's thesis, Delft University of Technology, 2014.

[26] Gamidi Rama Krishna, Ramesh Devarapalli, Garima Lal, and C. Malla Reddy. Mechanically flexible organic crystals achieved by introducing weak interactions in structure: Supramolecular shape synthons. *Journal of the American Chemical Society*, 138(41):13561–13567, 2016. doi: 10.1021/jacs.6b05118. PMID: 27454016.

[27] Ruben-Simon Kühnel, David Reber, and Corsin Battaglia. A high-voltage aqueous electrolyte for sodium-ion batteries. *ACS Energy Letters*, 2(9):2005–2006, 2017.

[28] D. Larcher and J.-M. Tarascon. Towards greener and more sustainable batteries for electrical energy storage. *Nature Chemistry*, 7:19 EP–, Nov 2014. URL `http://dx.doi.org/10.1038/nchem.2085`. Review Article.

[29] Jaegi Lee, Yongwon Lee, Jeongmin Lee, Sang-Min Lee, Jeong-Hee Choi, Hyungsub Kim, Mi-Sook Kwon, Kisuk Kang, Kyu Tae Lee, and Nam-Soon Choi. Ultraconcentrated sodium bis(fluorosulfonyl)imide-based electrolytes for high-performance sodium metal batteries. *ACS Applied Materials & Interfaces*, 9 (4):3723–3732, 2017.

[30] Wanfeng Li, Fang Zhang, Xingde Xiang, and Xiucheng Zhang. High-efficiency na-storage performance of a nickel-based ferricyanide cathode in high-concentration electrolytes for aqueous sodium-ion batteries. *ChemElectroChem*, 4(11):2870–2876, 2017. ISSN 2196-0216. doi: 10.1002/celc.201700776. URL `http://dx.doi.org/10.1002/celc.201700776`.

[31] Xiaona Li, Xiaobo Zhu, Jianwen Liang, Zhiguo Hou, Yan Wang, Ning Lin, Yongchun Zhu, and Yitai Qian. Graphene-supported nati2(po4)3 as a high rate anode material for aqueous sodium ion batteries. *Journal of The Electrochemical Society*, 161(6):A1181–A1187, 2014. doi: 10.1149/2.0081409jes. URL http://jes.ecsdl.org/content/161/6/A1181.abstract.

[32] Zheng Li, David Young, Kai Xiang, W Carter, and Yet-Ming Chiang. Towards high power high energy aqueous sodium-ion batteries: The nati 2(po4)3/na0.44mno2system. *Advanced Energy Materials*, 3, 03 2013.

[33] Jia-Yan Luo, Wang-Jun Cui, Ping He, and Yong-Yao Xia. Raising the cycling stability of aqueous lithium-ion batteries by eliminating oxygen in the electrolyte. *Nature Chemistry*, 2:760–765, Aug 2010. URL http://dx.doi.org/10.1038/nchem.763. Article.

[34] Michael G. Medvedev, Ivan S. Bushmarinov, Jianwei Sun, John P. Perdew, and Konstantin A. Lyssenko. Density functional theory is straying from the path toward the exact functional. *Science*, 355(6320): 49–52, 2017. doi: 10.1126/science.aah5975. URL http://science.sciencemag.org/content/355/6320/49.

[35] Kosuke Nakamoto, Yusuke Kano, Ayuko Kitajou, and Shigeto Okada. Electrolyte dependence of the performance of a na2fep2o7//nati2(po4)3 rechargeable aqueous sodium-ion battery. *Journal of Power Sources*, 327:327–332, 09 2016.

[36] Kosuke NAKAMOTO, Ryo SAKAMOTO, Masato ITO, Ayuko KITAJOU, and Shigeto OKADA. Effect of concentrated electrolyte on aqueous sodium-ion battery with sodium manganese hexacyanoferrate cathode. *Electrochemistry*, 85(4):179–185, 2017. doi: 10.5796/electrochemistry.85.179.

[37] Prasant Kumar Nayak, Liangtao Yang, Wolfgang Brehm, and Philipp Adelhelm. From lithium-ion to sodium-ion batteries: Advantages, challenges, and surprises. *Angewandte Chemie International Edition*, 2017. ISSN 1521-3773. doi: 10.1002/anie.201703772. URL http://dx.doi.org/10.1002/anie.201703772.

[38] Viorica-Alina Oltean, Stéven Renault, Mario Valvo, and Daniel Brandell. Sustainable materials for sustainable energy storage: Organic na electrodes. *Materials*, 9(3), 2016. ISSN 1996-1944. doi: 10.3390/ma9030142. URL http://www.mdpi.com/1996-1944/9/3/142.

[39] Huilin Pan, Yong-Sheng Hu, and Liquan Chen. Room-temperature stationary sodium-ion batteries for large-scale electric energy storage. *Energy Environ. Sci.*, 6:2338–2360, 2013. doi: 10.1039/C3EE40847G. URL http://dx.doi.org/10.1039/C3EE40847G.

[40] Sun Il Park, Irina Gocheva, Shigeto Okada, and Jun-ichi Yamaki. Electrochemical properties of nati2(po4)3 anode for rechargeable aqueous sodium-ion batteries. *Journal of The Electrochemical Society*, 158(10):A1067–A1070, 2011. doi: 10.1149/1.3611434. URL http://jes.ecsdl.org/content/158/10/A1067.abstract.

[41] Richard Perez and Marc Perez. A fundamental look at energy reserves for the planet. *IEA-SHCP-Newsletter*, 62, 11 2015.

[42] Justyna Piwek, Anetta Platek, Krzysztof Fic, and Elzbieta Frackowiak. Carbon-based electrochemical capacitors with acetate aqueous electrolytes. *Electrochimica Acta*, 215(Supplement C):179 – 186, 2016. ISSN 0013-4686. doi: https://doi.org/10.1016/j.electacta.2016.08.061. URL http://www.sciencedirect.com/science/article/pii/S0013468616317716.

[43] H. Qin, Z.P. Song, H. Zhan, and Y.H. Zhou. Aqueous rechargeable alkali-ion batteries with polyimide anode. *Journal of Power Sources*, 249(Supplement C):367 – 372, 2014. ISSN 0378-7753. doi: https://doi.org/10.1016/j.jpowsour.2013.10.091. URL http://www.sciencedirect.com/science/article/pii/S0378775313017576.

[44] Q.T. Qu, Y. Shi, S. Tian, Y.H. Chen, Y.P. Wu, and R. Holze. A new cheap asymmetric aqueous supercapacitor: Activated carbon//namno2. *Journal of Power Sources*, 194(2):1222 – 1225, 2009. ISSN 0378-7753. doi: https://doi.org/10.1016/j.jpowsour.2009.06.068. URL http://www.sciencedirect.com/science/article/pii/S0378775309010842.

[45] P Ramesh Kumar, Young Hwa Jung, Brindha Moorthy, and Do Kyung Kim. ffect of electrolyte additives on nati2(po4)3-c//na3v2o2x(po4)2f3-2x-mwcnt aqueous rechargeable sodium ion battery performance. *Journal of the Electrochemical Society*, 163:A1484–A1492, 05 2016.

[46] David Reber, Ruben-Simon Kuhnel, and Corsin Battaglia. High-voltage aqueous supercapacitors based on natfsi. *Sustainable Energy Fuels*, 1:2155–2161, 2017. doi: 10.1039/C7SE00423K. URL http://dx.doi.org/10.1039/C7SE00423K.

[47] Geeta S. Vadehra, Ryan P. Maloney, Miguel Garcia-Garibay, and Bruce Dunn. Naphthalene diimide based materials with adjustable redox potentials: Evaluation for organic lithium-ion batteries. *Chemistry of Materials*, 26:7151–7157, 12 2014.

[48] Ken Sakaushi, Eiji Hosono, Georg Nickerl, Thomas Gemming, Haoshen Zhou, Stefan Kaskel, and Jürgen Eckert. Aromatic porous-honeycomb electrodes for a sodium-organic energy storage device. *Nature Communications*, 4:1485 EP –, Feb 2013. URL http://dx.doi.org/10.1038/ncomms2481. Article.

[49] S.T. Senthilkumar, Mari Abirami, Junsoo Kim, Wooseok Go, Soo Min Hwang, and Youngsik Kim. Sodium-ion hybrid electrolyte battery for sustainable energy storage applications. *Journal of Power Sources*, 341 (Supplement C):404 – 410, 2017. ISSN 0378-7753. doi: https://doi.org/10.1016/j.jpowsour.2016.12.015. URL http://www.sciencedirect.com/science/article/pii/S0378775316316974.

[50] Michael D. Slater, Donghan Kim, Eungje Lee, and Christopher S. Johnson. Sodium-ion batteries. *Advanced Functional Materials*, 23(8):947–958, 2013. ISSN 1616-3028. doi: 10.1002/adfm.201200691. URL http://dx.doi.org/10.1002/adfm.201200691.

[51] Leland Smith and Bruce Dunn. Opening the window for aqueous electrolytes. *Science*, 350(6263):918–918, 2015. ISSN 0036-8075. doi: 10.1126/science.aad5575. URL http://science.sciencemag.org/content/350/6263/918.

[52] Zhiping Song, Hui Zhan, and Yunhong Zhou. Polyimides: Promising energy-storage materials. *Angewandte Chemie International Edition*, 49(45):8444–8448, 2010. ISSN 1521-3773. doi: 10.1002/anie.201002439. URL http://dx.doi.org/10.1002/anie.201002439.

[53] Liumin Suo, Oleg Borodin, Tao Gao, Marco Olguin, Janet Ho, Xiulin Fan, Chao Luo, Chunsheng Wang, and Kang Xu. "water-in-salt" electrolyte enables high-voltage aqueous lithium-ion chemistries. *Science*, 350(6263):938–943, 2015. ISSN 0036-8075. doi: 10.1126/science.aab1595.

[54] Liumin Suo, Oleg Borodin, Wei Sun, Xiulin Fan, Chongyin Yang, Fei Wang, Tao Gao, Zhaohui Ma, Marshall Schroeder, Arthur vonCresce, Selena M. Russell, Michel Armand, Austen Angell, Kang Xu, and Chunsheng Wang. Advanced high-voltage aqueous lithium-ion battery enabled by "water-in-bisalt" electrolyte. *Angewandte Chemie International Edition*, 55(25):7136–7141, 2016. ISSN 1521-3773. doi: 10.1002/anie.201602397. URL http://dx.doi.org/10.1002/anie.201602397.

[55] Liumin Suo, Oleg Borodin, Yuesheng Wang, Rong Xiaohui, Wei Sun, Xiulin Fan, Xu Shuyin, Marshall Schroeder, Arthur V. Cresce, Fei Wang, Chongyin Yang, Yong-Sheng Hu, Kang Xu, and Chunsheng Wang. "water-in-salt" electrolyte makes aqueous sodium-ion battery safe, green, and long-lasting. *Advanced Energy Materials*, 07 2017.

[56] A. D. Tevar and J. F. Whitacre. Relating synthesis conditions and electrochemical performance for the sodium intercalation compound na4mn9o18 in aqueous electrolyte. *Journal of The Electrochemical Society*, 157(7):A870–A875, 2010. doi: 10.1149/1.3428667. URL http://jes.ecsdl.org/content/157/7/A870.abstract.

[57] Alexandre Tkatchenko and Matthias Scheffler. Accurate molecular van der waals interactions from ground-state electron density and free-atom reference data. *Phys. Rev. Lett.*, 102:073005, Feb 2009.

[58] Alexandros Vasileiadis. Sodium storage in titanium oxides for na-ion batteries. Master's thesis, Delft University of Technology, 2014.

[59] M. Wagemaker. Towards static storage of renewable energy: New organic electrodes for cheap na-aqueous batteries, 2016. Unpusblished document, Grant application, Open Technologieprogramma.

[60] Caiyun Wang, Wen Zheng, Zhilian Yue, Chee O. Too, and Gordon G. Wallace. Buckled, stretchable polypyrrole electrodes for battery applications. *Advanced Materials*, 23(31):3580–3584, 2011. ISSN 1521-4095. doi: 10.1002/adma.201101067. URL http://dx.doi.org/10.1002/adma.201101067.

[61] Heng-guo Wang, Shuang Yuan, De-long Ma, Xiao-lei Huang, Fan-lu Meng, and Xin-bo Zhang. Tailored aromatic carbonyl derivative polyimides for high-power and long-cycle sodium-organic batteries. *Advanced Energy Materials*, 4(7):1301651–n/a, 2014. ISSN 1614-6840. doi: 10.1002/aenm.201301651. URL http://dx.doi.org/10.1002/aenm.201301651. 1301651.

[62] Song Weixing and Cao Guozhong. Universal organic anodes enable safe low-cost aqueous rechargeable batteries with long cycle life, high capacity, and fast kinetics. *SCIENCE CHINA Materials*, 60(8):789, 2017. doi: https://doi.org/10.1007/s40843-017-9075-7. URL http://engine.scichina.com/publisher/ScienceChinaPress/journal/SCIENCECHINAMaterials/60/8/10.1007/s40843-017-9075-7.

[63] Colin Wessells, Riccardo Ruff, Robert A. Huggins, and Yi Cui. Investigations of the electrochemical stability of aqueous electrolytes for lithium battery applications. *Electrochemical and Solid-State Letters*, 13(5):A59–A61, 2010. doi: 10.1149/1.3329652. URL http://esl.ecsdl.org/content/13/5/A59.abstract.

[64] J.F. Whitacre, A. Tevar, and S. Sharma. Na4mn9o18 as a positive electrode material for an aqueous electrolyte sodium-ion energy storage device. *Electrochemistry Communications*, 12(3):463 – 466, 2010. ISSN 1388-2481. doi: https://doi.org/10.1016/j.elecom.2010.01.020. URL http://www.sciencedirect.com/science/article/pii/S1388248110000330.

[65] J.F. Whitacre, T. Wiley, S. Shanbhag, Y. Wenzhuo, A. Mohamed, S.E. Chun, E. Weber, D. Blackwood, E. Lynch-Bell, J. Gulakowski, C. Smith, and D. Humphreys. An aqueous electrolyte, sodium ion functional, large format energy storage device for stationary applications. *Journal of Power Sources*, 213 (Supplement C):255 – 264, 2012. ISSN 0378-7753. doi: https://doi.org/10.1016/j.jpowsour.2012.04.018. URL http://www.sciencedirect.com/science/article/pii/S0378775312007495.

[66] Wei Wu, Sneha Shanbhag, Jiang Chang, Ann Rutt, and Jay F. Whitacre. Relating electrolyte concentration to performance and stability for nati2(po4)3/na0.44mno2 aqueous sodium-ion batteries. *Journal of the Electrochemical Society*, 162:A803–A808, 02 2015.

[67] Xian-yong Wu, Meng-ying Sun, Yi-fei Shen, Jiang-feng Qian, Yu-liang Cao, Xin-ping Ai, and Han-xi Yang. Energetic aqueous rechargeable sodium-ion battery based on na2cufe(cn)6–nati2(po4)3 intercalation chemistry. *ChemSusChem*, 7(2):407–411, 2014. ISSN 1864-564X. doi: 10.1002/cssc.201301036. URL http://dx.doi.org/10.1002/cssc.201301036.

[68] Xianyong Wu, Yuliang Cao, Xinping Ai, Jiangfeng Qian, and Hanxi Yang. A low-cost and environmentally benign aqueous rechargeable sodium-ion battery based on nati2(po4)3–na2nife(cn)6 intercalation chemistry. *Electrochemistry Communications*, 31(Supplement C):145 – 148, 2013. ISSN 1388-2481. doi: https://doi.org/10.1016/j.elecom.2013.03.013. URL http://www.sciencedirect.com/science/article/pii/S1388248113000957.

[69] Maowen Xu, Yubin Niu, Yutao Li, Shujuan Bao, and Chang Ming Li. Synthesis of sodium manganese oxides with tailored multi-morphologies and their application in lithium/sodium ion batteries. *RSC Adv.*, 4:30340–30345, 2014. doi: 10.1039/C4RA03735A. URL http://dx.doi.org/10.1039/C4RA03735A.

[70] Yang Xu, Min Zhou, and Yong Lei. Organic materials for rechargeable sodium-ion batteries. *Materials Today*, 2017. ISSN 1369-7021. doi: https://doi.org/10.1016/j.mattod.2017.07.005. URL http://www.sciencedirect.com/science/article/pii/S1369702117301414.

[71] Yuki Yamada, Keizo Furukawa, Keitaro Sodeyama, Keisuke Kikuchi, Makoto Yaegashi, Yoshitaka Tateyama, and Atsuo Yamada. Unusual stability of acetonitrile-based superconcentrated electrolytes for fast-charging lithium-ion batteries. *Journal of the American Chemical Society*, 136(13):5039–5046, 2014.

[72] Qing Zhang, Chaoyi Liao, Tianyou Zhai, and Huiqiao Li. A high rate 1.2v aqueous sodium-ion battery based on all nasicon structured nati2(po4)3 and na3v2(po4)3. *Electrochimica Acta*, 196(Supplement C):470 – 478, 2016. ISSN 0013-4686. doi: https://doi.org/10.1016/j.electacta.2016.03.007. URL http://www.sciencedirect.com/science/article/pii/S0013468616305217.

[73] Guoqiang Zou, Zhaodong Huang, Ganggang Zhao, Simin Li, Hongshuai Hou, Xiaoqing Qiu, and Xiaobo Ji. Evaluating the storage behavior of superior low-cost anode material from biomass for high-rate sodium-ion batteries. *Journal of The Electrochemical Society*, 164(7):A1431–A1437, 2017. doi: 10.1149/2.0521707jes. URL http://jes.ecsdl.org/content/164/7/A1431.abstract.

A

Appendix A: The molecular configuration and crystal structure of NDMe

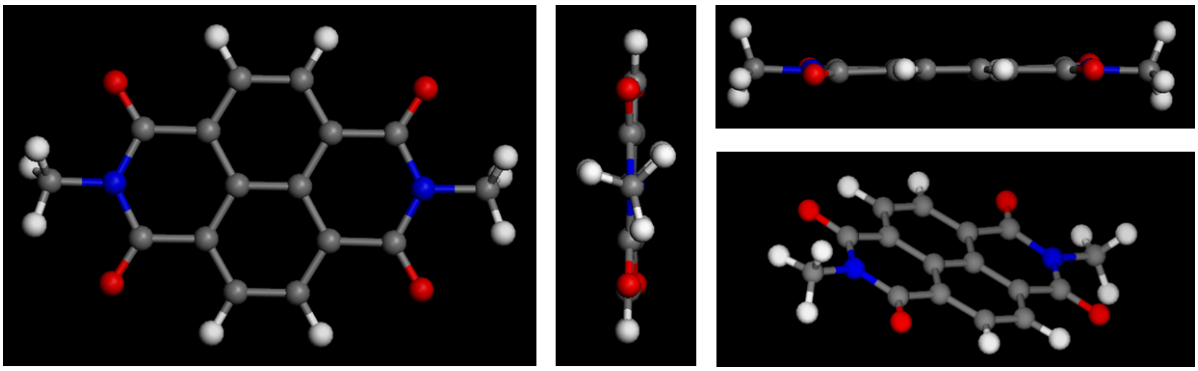

Figure A.1: The empty host structure of NDMe from frontal, side, top and diagonal perspective as derived from experimental data.[26]

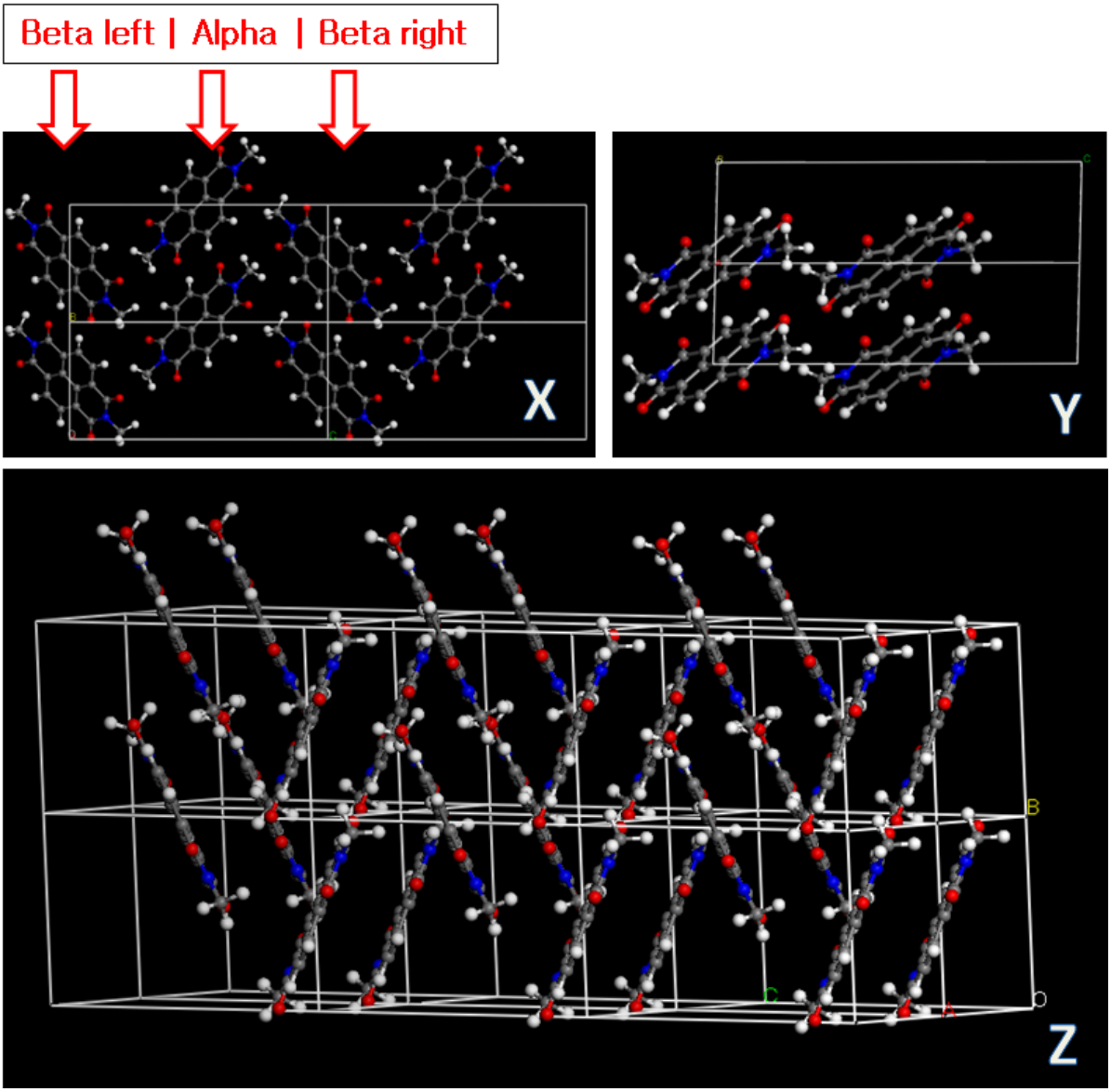

Figure A.2: Crystal orientation of NDMe, looking into X direction, Y direction, near Z direction as derived from experimental data.[26]

B

Appendix B: The molecular configuration and crystal structure of NDTo

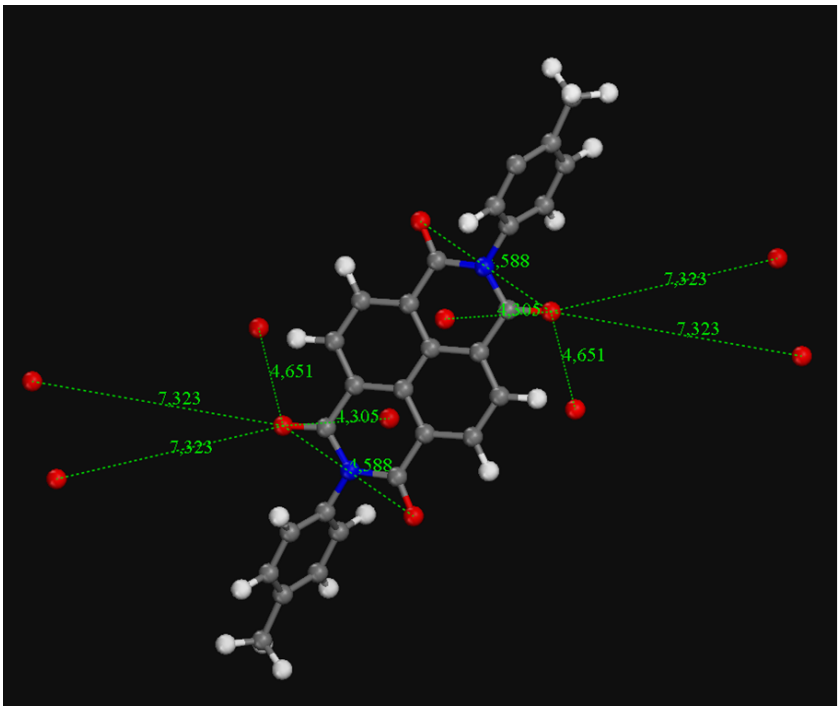

Figure B.1: Empty host molecule of NDTo with indicated distances between the O2 oxygen atom (right) and O3 oxygen atom (left) with surrounding oxygen atoms

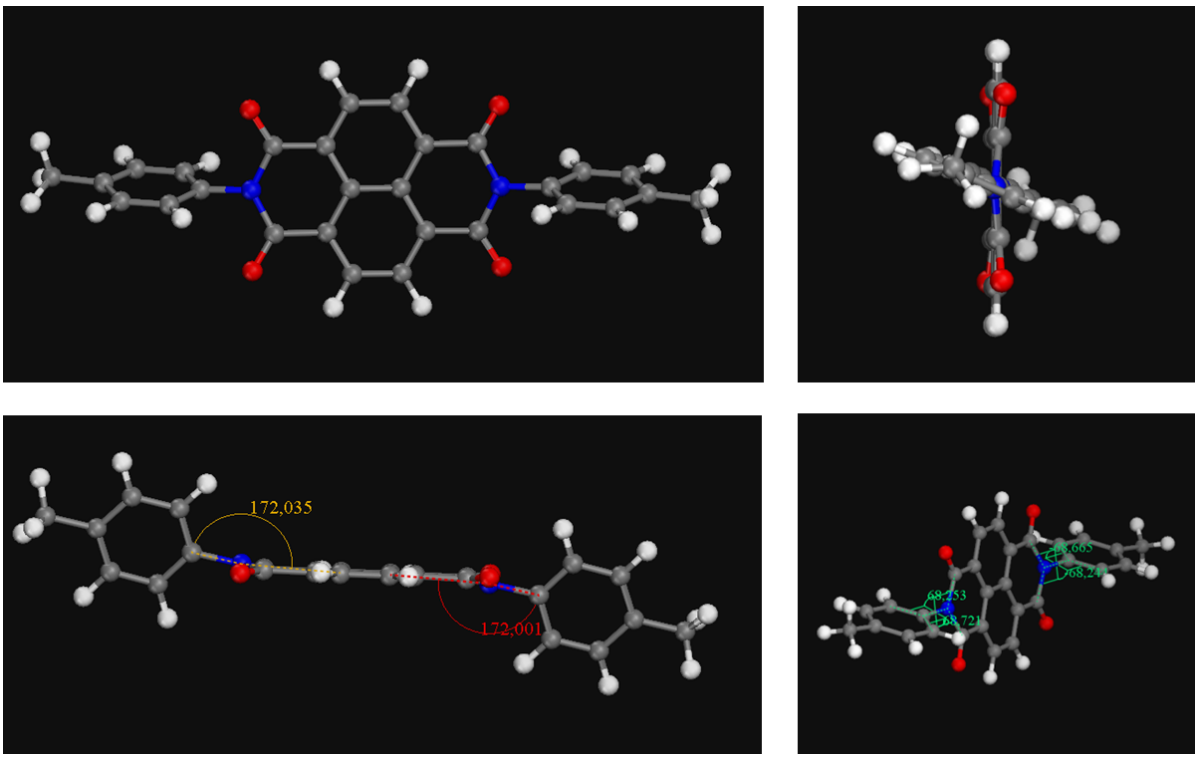

Figure B.2: The empty host structure of NDTo from frontal, side, top and diagonal perspective including angles of twists as derived from experimental data.[26]

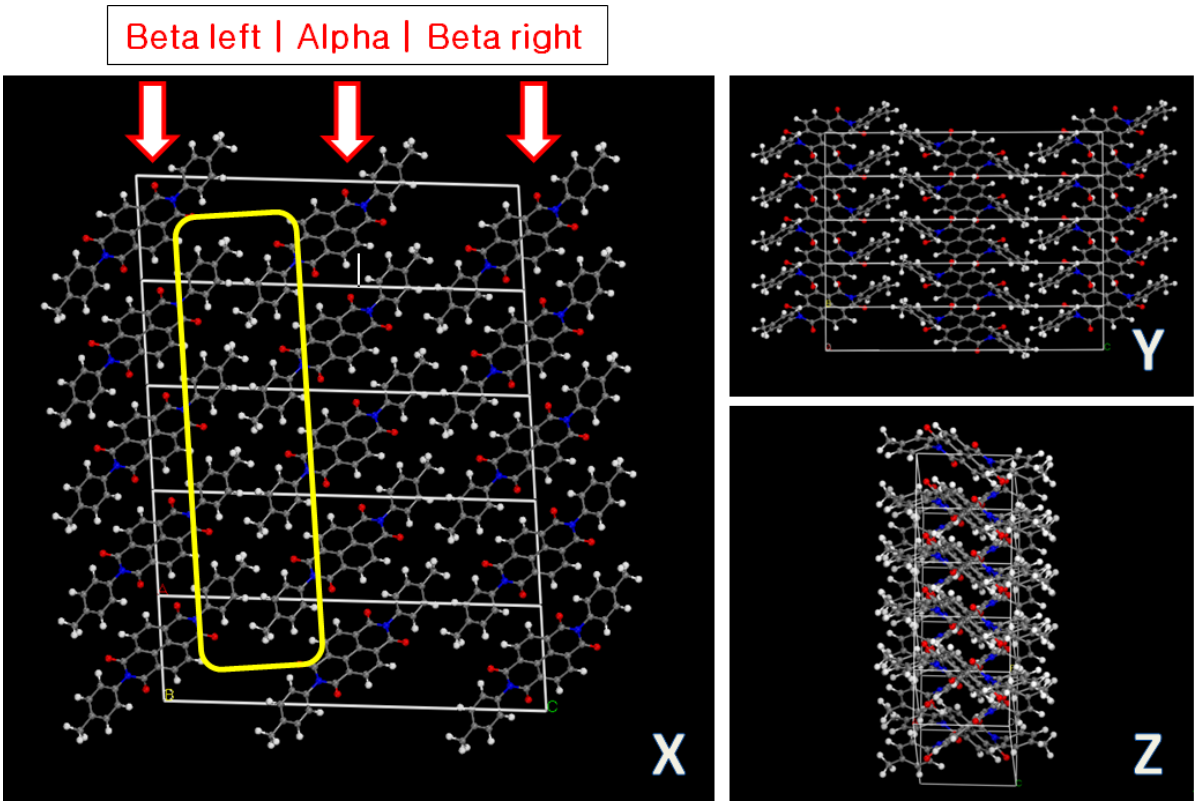

Figure B.3: Crystal orientation of NDTo, looking into X direction, Y direction and Z direction as derived from experimental data.[26]

C

Appendix C: Overview of the INCAR file settings

- ENCUT=520
- ISTART=0
- ICHARG=2
- PREC=Med
- NSW=1000
- ISIF=3
- IBRION=2
- LREAL=Auto
- ISMEAR=-5
- NPAR=4
- ISYM=0

D

Appendix D: Outcomes of different Van der Waals correction models

In order to gain insight in the significance of the Van der Waals corrections, a series of calculations were executed based on the insights of the uncorrected NDMe and NDTo sodiation pathways. A set of calculations for the empty host structure with different Van der Waals correction models were performed. The tables on the next page show the calculation outcomes. The outcomes show significant deviations in relaxation energy, unit cell volume and crystallinity between the Van der Waals correction models.

Table D.1: Calculation outcomes of empty NDMe unit cell with different Van der Waals correction models.

	Energy (eV)	Volume	ΔV%	a	Δa%	b	Δb%	c	Δc%	α (°)	$\Delta\alpha$%	β (°)	$\Delta\beta$%	γ (°)	$\Delta\gamma$%
Experimental	-	629,380		4,622		8,019		17,024		90,000		93,990		90,000	
IVDW = 0	-451,92410	690,620	9,73%	4,880	5,59%	8,018	-0,01%	17,656	3,71%	90,000	0,00%	91,350	-2,81%	90,010	0,01%
IVDW = 1	-456,14236	603,190	-4,16%	4,522	-2,15%	7,961	-0,72%	16,879	-0,85%	89,950	-0,06%	96,980	3,18%	89,970	-0,03%
IVDW = 10	-456,14236	603,190	-4,16%	4,522	-2,15%	7,961	-0,72%	16,879	-0,85%	89,950	-0,06%	96,980	3,18%	89,970	-0,03%
IVDW = 11	-455,70092	626,750	-0,42%	4,630	0,18%	7,929	-1,12%	17,131	0,63%	89,930	-0,08%	94,790	0,85%	89,970	-0,03%
IVDW = 12	-457,07420	620,880	-1,35%	4,600	-0,47%	7,934	-1,06%	17,083	0,35%	90,010	0,01%	95,170	1,26%	90,010	0,01%
IVDW = 202	-451,92410	690,620	9,73%	4,880	5,59%	8,018	-0,01%	17,656	3,71%	90,000	0,00%	91,350	-2,81%	90,010	0,01%
IVDW = 4	-451,92410	690,620	9,73%	4,880	5,59%	8,018	-0,01%	17,656	3,71%	90,000	0,00%	91,350	-2,81%	90,010	0,01%

Table D.2: Calculation outcomes of empty NDTo unit cell with different Van der Waals correction models.

	Energy (eV)	Volume	ΔV%	a	Δa%	b	Δb%	c	Δc%	α (°)	$\Delta\alpha$%	β (°)	$\Delta\beta$%	γ (°)	$\Delta\gamma$%
experimental		1007,490		8,040		4,324		29,008		90,000		92,363		90,000	
IVDW = 0	-725,97334	1129,920	12,15%	8,179	1,73%	4,651	7,57%	29,798	2,72%	90,000	0,00%	94,580	2,40%	90,000	0,00%
IVDW = 1	-732,70565	969,830	-3,74%	8,064	0,30%	4,168	-3,60%	28,870	-0,48%	90,000	0,00%	91,930	-0,47%	90,000	0,00%
IVDW = 10	-732,70565	969,830	-3,74%	8,064	0,30%	4,168	-3,60%	28,870	-0,48%	90,000	0,00%	91,930	-0,47%	90,000	0,00%
IVDW = 11	-731,97248	1025,170	1,75%	8,105	0,81%	4,336	0,29%	29,210	0,70%	90,000	0,00%	92,880	0,56%	90,000	0,00%
IVDW = 12	-725,97339	1129,930	12,15%	8,179	1,73%	4,651	7,57%	29,799	2,73%	90,000	0,00%	94,570	2,39%	90,000	0,00%
IVDW = 202	-725,97316	1129,750	12,14%	8,179	1,73%	4,651	7,57%	29,795	2,71%	90,000	0,00%	94,590	2,41%	90,000	0,00%
IVDW = 4	-725,97316	1129,740	12,13%	8,179	1,73%	4,651	7,57%	29,795	2,71%	90,000	0,00%	94,590	2,41%	90,000	0,00%

E

Appendix E: Outcomes of the step-wise sodium insertion of NDMe and NDTo

The Van der Waals correction model of IVDW=11 was selected for further calculations. The overview of the calculation outcomes for different correction models is given in the elaborate tables on the following page.

Table E.1: Calculation outcomes of the uncorrected and corrected step-wise sodium insertion pathway of NDMe.

		Energy (eV)	Volume	Δ V %	Δ V % T	a (Å)	Δ a%	Δ a% T	b (Å)	Δ b%	Δ b% T	c (Å)	Δ c%	Δ c% T
Uncorrected	Empty	-451,9241	690,62			4,88			8,018			17,656		
	Step 1	-457,9168	769,17	11,37%	-	5,373	10,10%	-	7,948	-0,87%	-	18,056	2,27%	-
	Step 2	-464,2264	752,38	-2,19%	8,94%	6,341	18,02%	29,94%	7,513	-5,47%	-6,30%	15,808	-12,45%	-10,47%
	Step 3	-466,9718	796,65	5,88%	-	6,727	6,09%	-	7,281	-3,09%	-	16,495	4,35%	-
	Step 4	-469,7591	767,71	-3,64%	2,04%	7,205	7,11%	13,63%	6,758	-7,18%	-10,05%	16,143	-2,13%	2,12%
Vd Waal corrected	Empty	-455,70092	626,75			4,63			7,929			17,131		
	Step 1	-461,75254	636,96	1,63%	-	5,172	11,71%	-	7,51	-5,28%	-	16,529	-3,51%	-
	Step 2	-468,02643	669,8	5,14%	6,87%	5,952	15,08%	28,55%	7,339	-2,28%	-7,44%	15,343	-7,18%	-10,44%
	Step 3	-471,53351	692,85	3,44%	3,44 %	6,616	11,16%	11,16%	6,896	-6,04%	-6,04%	15,299	-0,29%	-0,29%
	Step 4	-474,90945	719,04	3,79%	3,78%	6,951	5,06%	5,06%	6,717	-2,60%	-2,60%	15,868	3,72%	3,72%

Table E.2: Calculation outcomes of the uncorrected and corrected step-wise sodium insertion pathway of NDTo.

		Energy (eV)	Volume	Δ V %	Δ V % T	a (Å)	Δ a%	Δ a% T	b (Å)	Δ b%	Δ b% T	c (Å)	Δ c%	Δ c% T
Uncorrected	Empty	-725,97332	1129,9			8,179			4,651			29,798		
	Step 1	-731,93042	1096,19	-2,60%	-2,98%	8,514	4,10%	4,10%	4,295	-7,65%	-7,65%	30,191	1,32%	1,32%
	Step 2	-736,50636	1091,9	-0,19%	-0,39%	8,674	1,88%	1,88%	4,233	-1,44%	-1,44%	30,01	-0,60%	-0,60%
	Step 3	-739,66989	1191,86	9,81%	-	9,094	4,84%	-	4,423	4,49%	-	30,081	0,24%	-
	Step 4	-742,94261	1231,48	3,61%	12,78%	9,386	3,21%	8,21%	4,487	1,45%	6,00%	29,767	-1,04%	-0,81%
Vd Waal corrected	Empty	-731,97248	1025,17			8,105			4,336			29,21		
	Step 1	-738,68919	980,83	-4,33%	-4,33%	8,306	2,48%	2,48%	4,09	-5,67%	-5,67%	28,926	-0,97%	-0,97%
	Step 2	-743,70651	995,73	1,51%	-4,33%	8,539	2,81%	2,81%	4,058	-0,78%	-0,78%	28,861	-0,22%	-0,22%
	Step 3	-746,48745	1011,11	1,54%	-	8,671	1,55%	-	4,055	-0,07%	-	28,936	0,26%	-
	Step 4	-749,89015	1109,61	9,74%	11,44%	8,949	3,21%	4,80%	4,313	6,36%	6,28%	29,046	0,38%	0,64%

F

Appendix F: Relative difference in lattice distortion of NDMe and NDTo upon sodiation.

The following curves indicate the difference of the change in lattice parameters upon sodiation between the uncorrected and corrected calculations.

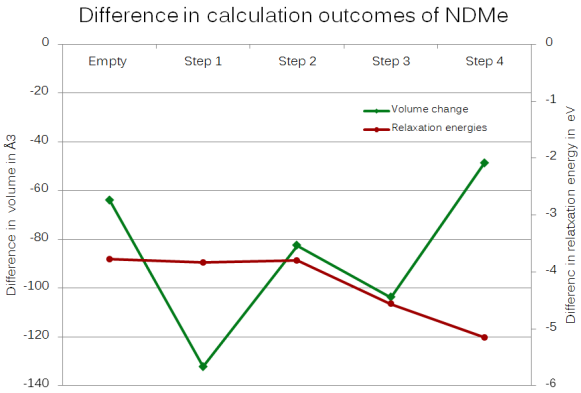

(a) Total volume and energies

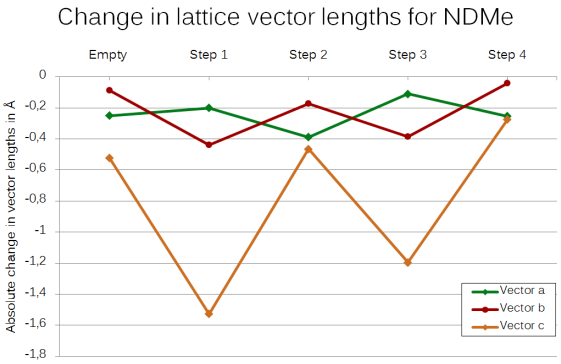

(b) Lattice vector lengths

Figure F.1: Difference between the change in total unit cell volume, relaxation energies and lattice vector lengths between the corrected and uncorrected NDMe calculations.

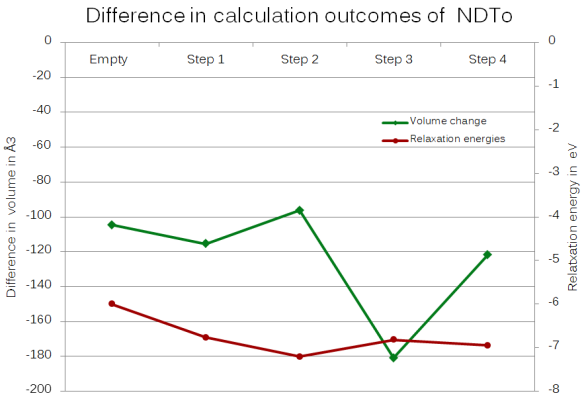

(a) Total volume and energies

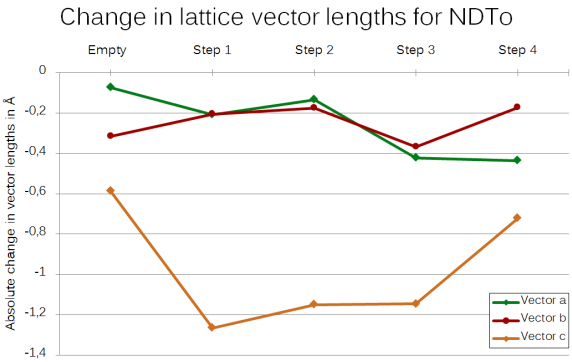

(b) Lattice vector lengths

Figure F.2: Difference between the change in total unit cell volume, relaxation energies and lattice vector lengths between the corrected and uncorrected NDTo calculations.

G

Appendix G: Experimental data of NDMe from previous studies

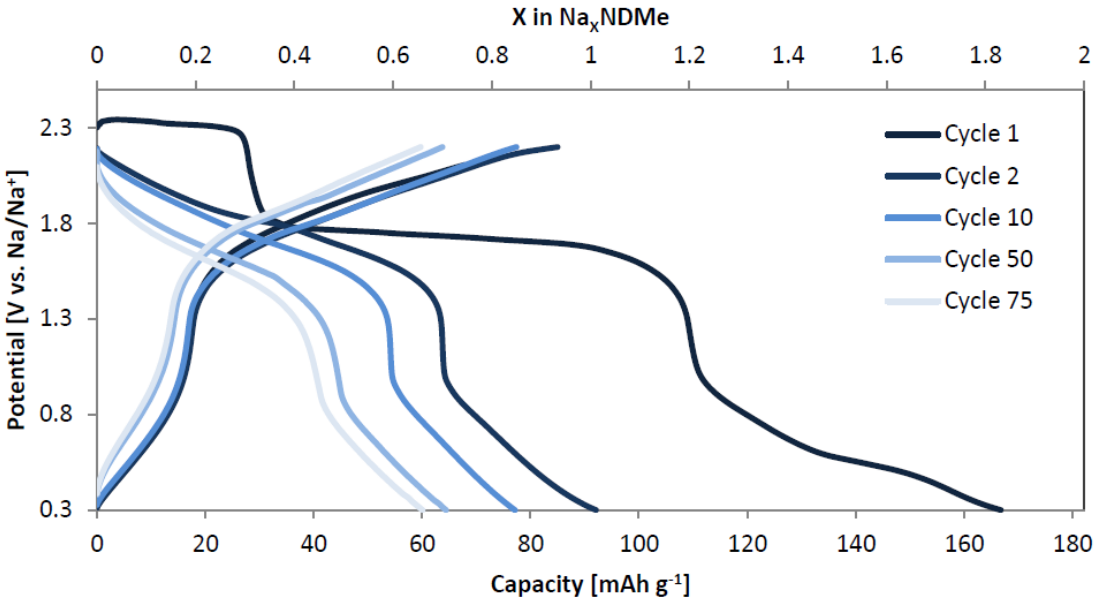

Figure G.1: Galvanostatic test of NDMe versus sodium at 0.1C, 1 M NaClO4 EC:PC electrolyte, as derived from Buise (2017) [5]

Appendix H: Cyclic Voltammetry results of $NaTi_2(PO_4)_3$ with side reactions

The spikes in graph H.1 indicate either side-reactions or measurement errors. When comparing the data of the consecutive cycles, the observation was made that for a number of exactly similar potentials, the high sudden peak currents were recorded. These values are -0.62027 V, -0.62277 V, -1,23550 V, -1,24039 V, -1,24283 V, - 1,24526 V, -1,24542 V and -1,24771 V versus Ag/AgCl.

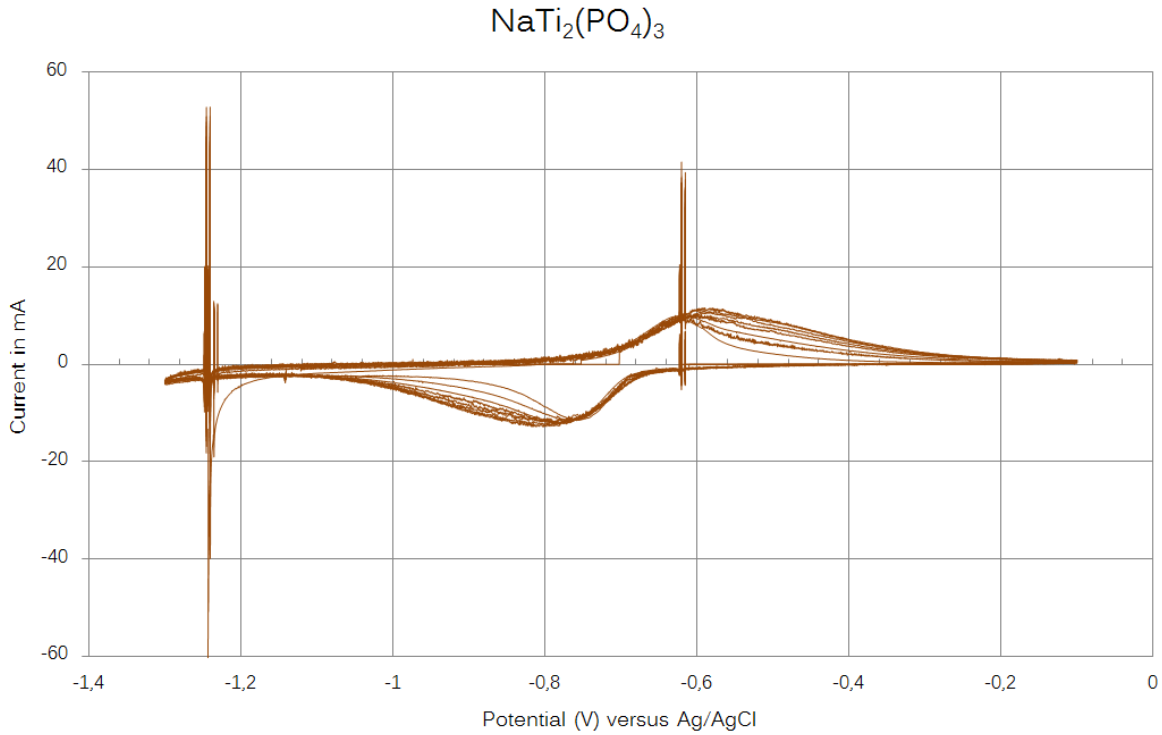

Figure H.1: Untreated cyclic voltammetry results of $NaTi_2(PO_4)_3$ at 0.5mV/s in 10M $NaClO_4$ indicating side reactions.

Appendix I: Photographs of corrosion non-active by metal clips

Figure I.1: Spot shaped corrosion on stainless steel.

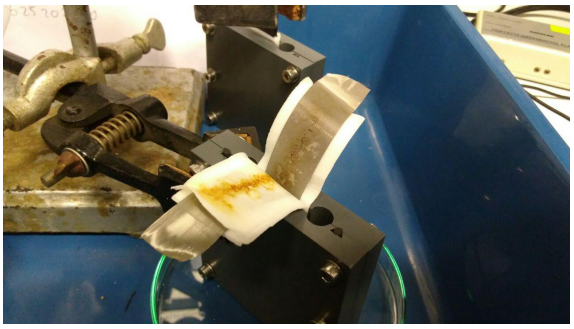

Figure I.2: Striped corrosion on stainless steel.

Figure I.3: Spot shaped 'burns' on carbon cloth.

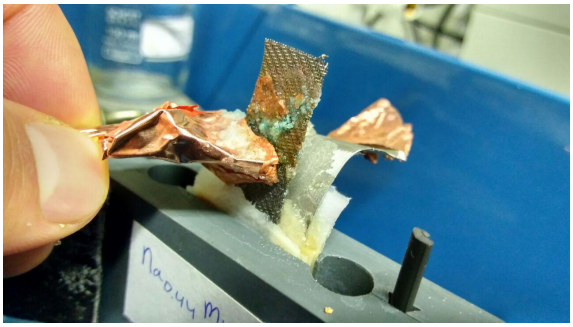

Figure I.4: Copper ions precipitation.

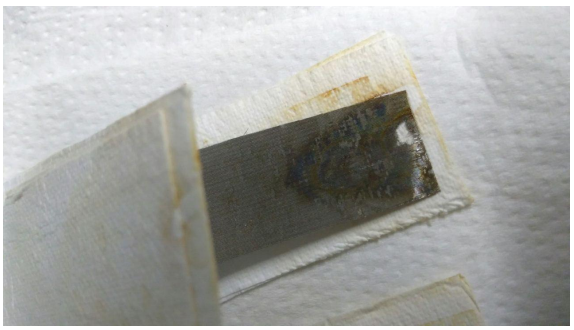

Figure I.5: Corrosion at the bottom side of steel.

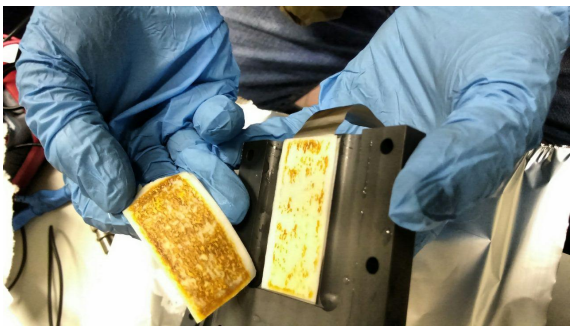

Figure I.6: Heavy corrosion over full steel surface.